CRACK DETECTION IN PLATED T-JOINTS THROUGH VIBRATION TECHNIQUES

YIN CHEN

Crack Detection in Plated T-joints Through Vibration Techniques

by

© Yin Chen, B. Eng., M. Eng.

A thesis submitted to the School of Graduate Studies

in partial fulfilment of the requirements for the degree of

Doctor of Philosophy

Faculty of Engineering and Applied Science

Memorial University of Newfoundland

June, 1996

St. John's Newfoundland Canada

To my parents

ACKNOWLEDGEMENTS

First of all, I would like to thank Dr. A.S.J. Swamidas, my thesis supervisor, for his constant guidance and assistance throughout the course of my graduate studies. His patience, supervision and giving of timely suggestions were indispensable to the successful completion of this dissertation. Thanks also go to the members of my supervisory committee, viz., Dr. M. Booton and Dr. J.Y. Guigne, for their helpful suggestions during my discussions of research problems.

The financial support from the Faculty of Engineering and Applied Science and the School of Graduate Studies of Memorial University of Newfoundland is also greatly appreciated.

I would also like to extend my gratitude to Mr. Austin Bursey and Mr. Ron O'Driscoll, for their great help in all the work associated with my experimental studies.

ABSTRACT

The study presents investigations on different aspects of vibration techniques for crack detection in welded T-joints; it incorporates experimental testing, finite element analysis, system identification and model updating procedures in developing a methodology for detecting and quantifying fatigue cracks in plated T-joints. The experimental study measured modal parameter changes that occur in a structure as a fatigue crack grows in the critical region of plated T-joints. The finite element model was generated and refined by comparing the frequency response functions (FRFs) obtained from the finite element (FE) model and the intact experimental model. Finally, combining the experimental and finite element results and utilizing a model updating procedure a methodology was developed to find out the location, length and depth of the crack at different intervals of fatigue crack growth; the methodology used the correlation between the finite element and experimental frequency response functions. Local strain frequency response functions, which are very sensitive to cracking, were used as the objective functions in the model updating procedure. Perturbation based updating procedure, which incrementally modifies the design parameters (i.e. crack location, length and depth) at every iteration, was used to minimize the error in FRFs between the experimental and finite element models. Changes in strain mode shapes were used to determine the approximate location of the crack initially; subsequent estimation of crack profile was carried out utilizing model updating procedure and using line spring (crack) elements to model the crack.

The crack location, length and depth measured from five experimental T-joint specimens have been correctly identified and quantified by this methodology. To the author's best knowledge, the application of this method to a plate-type structure and the accuracy that could be achieved have never been investigated in the published literature so far. At the conclusion of this study, a promising method for crack detection is provided. It is believed that this will help in the further development of new vibration-based NDE techniques for industrial applications.

CONTENTS

ABSTRACT		iv
List of Figures		viii
List of Tables		xiii
Nomenclature		xiv
CHAPTER 1	**INTRODUCTION**	1
1.1	Cracking and Crack Detection in Structures	1
1.2	Scope of the Present Study	2
1.3	Organization of the Thesis	4
CHAPTER 2	**LITERATURE REVIEW**	6
2.1	Nondestructive Evaluation and Damage Detection in Structures	6
2.2	Damage Detection Using Vibration Characteristics	7
	2.2.1 Monitoring of changes in modal parameters	10
	2.2.2 System identification/model updating procedures	16
2.3	Other Nondestructive Evaluation Techniques	21
2.4	Summary	23

CHAPTER 3 BASIC THEORIES 25

3.1 Modal Analysis and Testing 25

3.1.1 Multi-Degree-Of-Freedom (MDOF) system theory 25

3.1.2 Frequency response function 30

3.1.3 Modal parameter extraction 37

3.2 Finite Element Method 38

3.2.1 General equations of finite element analysis 38

3.2.2 Thin shell element 44

3.2.3 Line spring element for modelling crack 49

3.3 Model Updating for Damage Detection 53

3.4 Summary 57

CHAPTER 4 EXPERIMENTAL STUDY OF PLATED T-JOINTS UNDERGOING FATIGUE CRACKING 59

4.1 Methodology 59

4.2 Experimental Setup 61

4.2.1 Instrumentation for experiment 61

4.2.2 Modal testing 69

4.3 Results and Discussion 78

4.3.1 Natural frequencies and damping ratios 78

4.3.2 Frequency response functions for accelerations 83

4.3.3 Frequency response functions for surface strains 83

4.3.4 Mode shapes 94

4.4 Summary 98

CHAPTER 5 FINITE ELEMENT ANALYSIS OF PLATED T-JOINTS AND MODEL UPDATING FOR CRACK DETECTION 100

5.1 FE model 100

5.2 Refining of FE model to be Compatible with Experimental Results 104

5.3 Model Updating with Experimental Data for Crack Detection 111

5.3.1 Initial step using changes in strain mode shapes 111

5.3.2 Perturbation based approach of model updating procedure for crack detection 116

5.4 Discussions and Summary 126

CHAPTER 6 CONCLUSIONS 133

REFERENCES AND BIBLIOGRAPHY 138

Appendix I MODAL PARAMETER EXTRACTION METHODS 145

Appendix II WELDING PROCEDURE AND SPECIFICATIONS 153

Appendix III NATURAL FREQUENCIES AND DAMPING RATIOS OBTAINED FROM THE EXPERIMENTS ON SEVEN PLATED T-JOINTS 157

List of Figures

3.1	General three-dimensional body	39
3.2	Deformations considered for a for plate element	45
3.3	ABAQUS's S8R5 8-noded shell element	48
3.4	Single edge notched specimen	49
3.5	Line spring element	52
3.6	Line spring element in a shell mesh	52
4.1	Dimensions of a plated T-joint	62
4.2	Supporting mechanism for the T-joint	63
4.3	Photo of the whole experimental setup	65
4.4	The connection between the plate and the actuator	64
4.5	The actuator connected to the T-joint	67
4.6	The actuator disconnected from the T-joint	67
4.7	Cyclic sinusoidal fatigue load	68
4.8(a)	Samples of random signals	71
4.8(b)	Samples of sine sweep signals	72
4.9	Distribution of strain gauges and accelerometers	74
4.10	Normalized modal strains from a strip gauge	76

4.11	Procedure for data acquisition and signal processing	77
4.12	Overlap in signal processing	78
4.13(a)	Changes in frequency and damping ratio for first resonant frequency	80
4.13(b)	Changes in frequency and damping ratio for second resonant frequency	80
4.13(c)	Changes in frequency and damping ratio for third resonant frequency	81
4.13(d)	Changes in frequency and damping ratio for fifth resonant frequency	81
4.13(e)	Changes in frequency and damping ratio for sixth resonant frequency	82
4.13(f)	Changes in frequency and damping ratio for seventh resonant frequency	82
4.14(a)	Acceleration FRFs at a1 for various crack growth levels, close to the supporting edge (specimen #7)	85
4.14(b)	Acceleration FRFs at a11 for various crack growth levels; close to the weld toe (specimen #7)	86
4.15	Strain FRFs at s48 (single gauge) for various crack growth interval; s48 was located away from the crack (42 mm) (specimen #7)	88
4.16	Strain FRFs at s31 (strip gauge) for various crack growth intervals; s31 was located very close to the crack at the centre of the bottom plate (1-3 mm) (specimen #7)	89
4.17	Strain FRFs at s25 (single gauge) for various crack growth intervals; s25 was located away from the crack at the centre of the bottom plate (42 mm) (specimen #7)	90
4.18(a)	Strain FRFs at s41 (rosette gauge) for various crack growth intervals; s41 was located close to the crack at 45° to the crack (5-8 mm) (specimen #7)	91

4.18(b)	Strain FRFs at s42 (rosette gauge) for various crack growth intervals; s42 was located close to the crack at 90° to the crack (5-8 mm) (specimen #7)	92
4.18(c)	Strain FRFs at s43 (rosette gauge) for various crack growth intervals; s43 was located close to the crack at 135° to the crack (5-8 mm) (specimen #7)	93
4.19	Displacement mode shapes	95
4.20	Strain mode shapes for the intact T-joint	96
4.21	Strain mode shapes for the cracked T-joint	97
4.22	Crack profile for specimen #3	98
5.1	FE model of the plated T-joint	101
5.2	Fine mesh around the anticipated crack region	102
5.3	Mode shapes of the plated T-joint	105
5.4	Procedure used for refining the FE model; {X} represents parameters that are varied	107
5.5(a)	Acceleration FRFs obtained from refined FE model and intact experimental model at location a1 for specimen #7. Solid line is for experimental model and dashed line is for FE model	112
5.5(b)	Acceleration FRFs obtained from refined FE model and intact experimental model at location a11 for specimen #7. Solid line is for experimental model and dashed line is for FE model	112
5.5(c)	Strain FRFs obtained from refined FE model and intact experimental model at location s25 for specimen #7. Solid line is for experimental model and dashed line is for FE model	113

5.5(d) Strain FRFs obtained from refined FE model and intact experimental model at location s31 for specimen #7. Solid line is for experimental model and dashed line is for FE model 113

5.6 Strain FRFs obtained from refined FE model and intact experimental model at location s31 for specimen #3. Solid line is for experimental model and dashed line is for FE model 114

5.7 Strain FRFs obtained from refined FE model and intact experimental model at location s31 for specimen #4. Solid line is for experimental model and dashed line is for FE model 114

5.8 Strain FRFs obtained from refined FE model and intact experimental model at location s31 for specimen #5. Solid line is for experimental model and dashed line is for FE model 115

5.9 Strain FRFs obtained from refined FE model and intact experimental model at location s31 for specimen #6. Solid line is for experimental model and dashed line is for FE model 115

5.10 Strain mode shapes, before and after cracking (specimen #3) 117

5.11 Procedure of model updating for crack detection 118

5.12 FRFs at crack growth interval 4 for T-joint #7 at location s31. Solid line: cracked specimen; dashed line: FE model; dotted line: intact specimen 123

5.13 FRFs at crack growth interval 5 for T-joint #7 at location s31. Solid line: cracked specimen; dashed line: FE model; dotted line: intact specimen 123

5.14 FRFs at crack growth interval 6 for T-joint #7 at location s31. Solid line:

	cracked specimen: dashed line: FE model; dotted line: intact specimen	124
5.15	FRFs at crack growth interval 7 for T-joint #7 at location s31. Solid line: cracked specimen; dashed line: FE model; dotted line: intact specimen	124
5.16	Measured and predicted crack profile for specimen #7, at different crack growth intervals	125
5.17	Strain FRFs of specimen #3 at location s31. Solid line: cracked specimen; dashed line: FE model; dotted line: intact specimen	127
5.18	Measured (ink staining) and predicted crack profile for specimen #3	127
5.19	Strain FRFs of specimen #4 at location s31. Solid line: cracked specimen; dashed line: FE model; dotted line: intact specimen	128
5.20	Measured (ink staining) and predicted crack profile for the specimen #4	128
5.21	Strain FRFs of specimen #5 at location s31. Solid line: cracked specimen; dashed line: intact specimen	129
5.22	Measured (ink staining) and predicted crack profile for specimen #5	129
5.23	Strain FRFs of specimen #6 at location s31. Solid line: cracked specimen; dashed line: FE model; dotted line: intact specimen	130
5.24	Measured (ink staining) and predicted crack profile for specimen #6	130
AI.1	Modal circle for receptance	149
AII.1	Typical welded joint geometry	154
AII.2	Dime test for the T-joint welding	156

List of Tables

4.1	Young's modulus of steel used for plated T-joint	62
4.2	Fatigue loads and stress ranges used for different plated T-joint specimens	68
4.3	Specifications of STRUCTCEL accelerometer	75
4.4	Fatigue cycles for each crack growth interval of the seven plated T-joint specimens	84
5.1	Natural frequencies obtained from the FE model [experimental frequencies (from specimen #3) within bracket]	103
5.2	Natural frequencies obtained from each experimental specimen and the corresponding refined FE model	109
5.3	Predicted and measured crack length and depth at various crack growth intervals for specimen #7	122
5.4	Predicted and measured crack location, length and depth for the remainder of the test specimens	126

Nomenclature

$[A]$	strain-displacement matrix
A^r_{ij}	residue of rth mode
a	crack depth
$[B(s)]$	system matrix
C	crack centre
$[C]$	damping matrix
$[\bar{C}]_{modal}$	diagonal modal damping matrix
D	crack depth
E	Young's modulus
$\{F(t)\}$	force vector
$[H(s)]$	transfer function matrix
$H(\omega)$	frequency response function (FRF)
h	thickness of plate
$[K]$	stiffness matrix
$[\bar{K}]_{modal}$	diagonal modal stiffness matrix
K_I	stress intensity factor

L	crack length
$[M]$	mass matrix
$[\bar{M}]_{modal}$	diagonal modal mass matrix
$[N]$	displacement interpolation matrix
Q	sensitivity matrix
S	error function
s	Laplace variable
t	time
$\{U\}$	displacement vector
u, v, w	x, y, z direction displacement
X, Y, Z	global axes directions
x, y, z	local axes directions
β	rotation
Δ	difference between analytical and experimental FRFs
δ	difference of FRFs between cracked and uncracked experimental FRFs
ϵ, γ	strain
ζ_i	ith damping ratio
λ_r	system pole
ν	Poisson's ratio
Π	total potential
τ	stress
$[\phi]$	modal matrix

Ψ_r	rth modal strain
ω_i, Ω_i	ith natural frequency

CHAPTER 1

INTRODUCTION

1.1 Cracking and Crack Detection in Structures

Many structures are subjected to repeated regular/irregular cyclic loadings; parts of these structures will develop cracks after certain service life. For instance, offshore structures are subjected to repeated loadings due to ocean waves which impose a large number of cyclic stresses; under these varying cyclic stresses fatigue cracks develop at critical welded junctions of offshore structures. The cracks should be detected at an early stage so as to prevent them from developing into large cracks that would produce a catastrophic failure of the structure.

Therefore the prediction, detection and monitoring of cracks in structures have been the subject of intensive investigations during recent years. Its importance is shown in the strict guidelines enforced in the design of structures and structural components, as well as on the maintenance and in-situ repair carried out on structures for maximum effectiveness at minimum cost. Many theoretical and experimental studies of the behaviour of structures with cracks have been carried out to develop a feasible methodology. Thousands of theoretical and experimental studies have been carried out in the allied area of fatigue and fracture mechanics. Meanwhile,

many techniques have already been developed to quantify cracking and damage in structures, such as acoustic emission, magnetic particle inspection, alternating/direct current field measurement, eddy current measurement, ultrasonics, radiographic examination, etc.

The Non-Destructive Evaluation (NDE) techniques, listed above, have attracted the attention of many investigators for utilizing them in monitoring and detection of cracks developed in operating structures. Each of these methods has its own advantages and disadvantages. New techniques are being developed to meet the requirements of modern structures operating in more severe environments. Among these newly emerging techniques, the procedure for modal analysis and testing is being explored by many researchers to determine whether it can be used as an efficient technique for crack monitoring and detection.

1.2 Scope of the Present Study

The physical properties of any structure can be expressed in term of its mass, stiffness and damping. Any crack/damage that occurs in the structure will cause changes in these physical properties; and these changes will be reflected in the change of dynamic characteristics of the structure such as natural frequencies, mode shapes, displacements, strains/stresses and damping. A number of studies have already been carried out to investigate the sensitivities of these parameters to cracking in a structure. Early studies on vibration crack detection have focused on the changes in natural frequencies due to damage in the structure. Certain limitations have been observed in this approach, viz., (i) Changes in natural frequencies due to damage are too

small; (ii) Crack sizing becomes quite difficult; and (iii) It is not easy to locate the damage in the structure. Recently other parameters, which are more sensitive to cracking in the structure, have been investigated. Also, the fast growth of computer technology has made the finite element analysis method more accurate in terms of modelling the structure; consequently, matching the experimental results with the finite element analysis results in modal space is easier to achieve. This study investigates the sensitivities of the dynamic characteristics of a structure to crack development so as to develop a new technique to monitor, detect and locate cracks or damages in structures, especially in offshore structures. Model updating procedures which combine the experimental and analytical results (based on finite element analysis) will be used to quantify cracking in structures. Not only the location, but also the length and depth of crack would be determined for plate-type structures (in this particular study, plated T-joints were examined).

More specifically the following goals have been planned for this study:

i) Develop a methodology, based on frequency response function approach, to detect, quantify and locate fatigue or any other type of damage in a plate-type structure.

ii) Carry out modal testing of fatiguing plated T-joints, acquire experimental data on crack growth and its development, and identify the characteristic features of their dynamic responses.

iii) Carry out a finite element modal analysis and structural dynamic modification so that the experimental and analytical results of the study could be correlated to minimize the mean square error between experimental and analytical results; thereafter, a refined finite element model would be obtained.

iv) Use the perturbation based approach in model updating procedure to determine the extent and location of the crack. An updating algorithm based on minimizing the least square error between experimental frequency response functions and analytical frequency response functions of a structure with a crack, will be developed, and predicted values compared with measured experimental ones to determine the effectiveness of the methodology developed in this thesis.

1.3 Organization of the thesis

The research study reported in this thesis contains three parts, viz., (i) Experimental study; (ii) Analytical study (finite element analysis); and (iii) Model updating procedure, which combines both the experimental and analytical results, and gives the final predicted values. The thesis is written in the following format: Chapter 2 gives a review of the relevant studies carried out by other researchers in the area. Chapter 3 is devoted to basic theories needed to carry out the thesis research. They include the basic theories of finite element analysis, basic theories of modal analysis and testing, and basic theories required for model updating procedure. Chapter 4 discusses the experimental studies on plated T-joints, which include the experimental set up

for fatigue and modal testing, and the results of modal testing of seven T-joints. Chapter 5 includes the results of finite element analysis, and the model updating procedure. In this chapter, experimental and analytical results are combined, and the final predictions of the location and extent of the crack are presented and compared with the measured crack profiles. Finally, in Chapter 6, conclusions obtained from this study and recommendations for further studies are given.

CHAPTER 2

LITERATURE REVIEW

2.1 Nondestructive Evaluation and Damage Detection in Structures

The detection of cracks in components of structures in service is important to ensure integrity since these cracks can propagate and cause sudden failures. Such failures can be very costly in terms of human life and property damage. Therefore nondestructive evaluation (NDE) techniques are widely used for damage detection. Some of the commonly used techniques are acoustic emission, magnetic particle inspection, alternating/direct current field measurement, eddy current method, ultrasonics and radiographic measurements. Each of these techniques has its own advantages and disadvantages. The use of most of the well known NDE techniques may become inconvenient under certain situations due to the need for the investigator to have access to the component under operating conditions. Therefore a newly emerging technique using the vibrational characteristics of structures via modal analysis has been recently considered by many researchers for damage detection.

2.2 Damage Detection Using Vibrational Characteristics

The physical properties of any structure can be expressed in term of its mass, stiffness and damping. Any crack or damage that occurs in the structure will cause changes in these physical properties; and these changes will be reflected in changes of the dynamic characteristics of the structure, such as natural frequencies, mode shapes, damping ratios, modal amplitudes, etc. The numerous methods developed for damage/crack detection in a structure using vibration techniques during the past 25 years differ only in the techniques used to detect and quantify changes in the modal response, and the method for relating such changes to physical damage in the structure. Doebling et al. (1996) have summarized the research studies published during the past 25 years, dividing the investigations into two parts (309 references). The first part discusses various methods that have been developed and the philosophy and methodology behind each of them. They include:

(1) **Frequency change method**, which consists of calculating the damage parameters, e.g., crack length and/or location, from the frequency shifts;

(2) **Mode shape change method**, consisting of examining the changes of mode shapes due to the crack/damage of the structure;

(3) **Mode shape curvature or strain mode shape change method**, consisting of examining changes in these modal parameters due to the presence of crack/damage in a structure;

(4) **Methods based on measured flexibility**, which use the measured flexibility matrix to estimate changes in the static behaviour of the structure. Typically, damage is detected using flexibility matrices by comparing the flexibility matrices of the damaged structure to those of the undamaged structure, via a finite element or analytical model;

(5) **Matrix updating methods**. This class of methods is based on the modification of structural model matrices such as mass, stiffness, and damping, to reproduce results as closely as possible to the measured static or dynamic response of the structure. These methods solve for the updated matrices (or perturbation to the nominal model which produces the updated matrices) by forming a constrained optimization problem based on the structural equations of motion, the nominal model, and the measured data. The methods use a common basic set of equations, and the differences in the various algorithms result from the objective function to be minimized, constraints placed on the problem, and the numerical scheme used to implement the optimization;

(6) **Nonlinear methods** which examine the nonlinearity associated with the crack opening and closing;

(7) **Sensitivity methods**. Several sensitivity matrices were derived in these class of methods. The damage (normally represented in the reduction of an element or the magnitude of one of the stiffness matrices) was related to the changes of certain parameters, such as natural frequency or damping. By examining these changes (e.g. changes in natural

frequency) through the sensitivity matrix, the location of damage can be identified.

Of these seven methods, only the first three methods have been applied to complex structures such as plates, shells, bridges, offshore platforms, etc. The remainder of the methods have been developed and verified using simple structures such as trusses, beams and frames.

The second part of their review paper has listed various field/laboratory studies carried out for developing a damage detection methodology using vibration techniques. The kind of structures which have been tested include: (1) Metal and concrete beams; (2) Trusses; (3) Plates; (4) Shells; (5) Bridges; (6) Offshore platforms; (7) Other large civil engineering structures; (8)Aerospace structures; (9) Machinery; and (10) Composites. Most of the methods in this part of their review have used monitoring changes in natural frequencies, damping ratios, and mode shapes.

Another study which carried out a similar detailed investigation of the various vibration-based procedures for crack detection and monitoring (178 references) was reported by Rytter (1993). He also carried out experimental studies on beams besides carrying out detailed numerical investigation of a few of the listed procedures. He has classified the various available methodologies into level one (detection), level two (localization), level three (assessment) and level four (details of available safety limits) methods. More detailed examination of some of these methods are presented below.

2.2.1. Monitoring of changes in modal parameters

Adams, et al. (1978) examined a method by which damage in a structure can be identified from changes in the resonant frequencies. Shahrivar and Bouwkamp (1986) determined the natural frequency shifts in an offshore structure due to the presence of damages in structural elements. Modal testing of an offshore framed platform model, with grossly cracked structural members (severed members), was performed and a reduction in natural frequencies and increase in structural responses were reported.

Springer et al. (1991) reported that a boxbeam structure was built and tested at the Marshall Space Flight Centre (MSFC) for the purpose of evaluating the ability of the modal test to detect the presence of structural faults in space flight hardware. A finite element model of this structure was also developed and used to simulate the modal test results. The results of the finite element analysis compared favourably with the test data. No further results were presented in the paper.

Gomes and Silva (1990 and 1991) and Silva and Gomes (1992) conducted a series of studies using modal analysis for crack identification in simple structures. Modal tests of cantilever beams with increasing fatigue crack depths at different locations were performed. The influence of a lumped mass, which was attached to the structure (to simulate the end loads on the structure), was also studied. The main modal parameters that were monitored were the natural frequencies of the vibrating beams. A series of nondimensional curves and tables

depicting the changes in natural frequencies for various depths of the crack, location of the crack, and lumped masses were presented. Use of these tables and figures would give the probable depth and location of the crack in an cantilever beam. The method has only been tested under laboratory conditions and needs more detailed studies for application to more complex structures.

Richardson and Mannen (1991) developed modal sensitivity functions for the location of structural faults due to a change of mass, stiffness and/or damping in structural components. For small stiffness changes, where the fault was small enough so that the mode shapes did not change substantially, the authors gave the stiffness sensitivity equation as:

$$\{U_k\}^T[dK]\{U_k\} = \omega_{1k}^2 - \omega_{0k}^2 \qquad (2.1)$$

where $\{U_k\}$ is the modal displacement vector for the kth mode, [dK] is the change in the stiffness matrix for the structure, ω_{1k} is the frequency of the damaged structure, and ω_{0k} is the frequency of undamaged structure. Using this equation, when the change in natural frequency of kth mode and the corresponding model vectors are also known (where $k=1, \ldots, n$, n being the number of modes considered), the corresponding change in stiffness can be obtained, and vice-versa. Normally cracks in the structure tend to reduce the stiffness of the structure. Consequently when a structure is cracked, a natural frequency reduction is predicted. For mass and damping changes, similar sensitivity equations were derived in their paper. The method uses changes in natural frequencies alone for crack detection. These changes would be too small in a complex structure to correctly identify the stiffness changes dK.

Stubbs and Osegueda (1990) also derived expressions for changes in modal stiffness in terms of modal masses, modal dampings, eigenfrequencies and eigenvectors. From matrix structural analysis, sensitivity matrices which relate variations in stiffnesses of structural elements to the variations in modal stiffnesses were generated. Thus by examining the changes in modal parameters such as natural frequency and damping through the sensitivity matrix, the location and the magnitude of the damage can be detected. A case study of a simply supported beam was presented in their paper, and good results were achieved. This method requires the calculation of the variation in stiffness, which limits its application to more complex structures.

Most researchers have stated that damages in structures reduce the natural frequencies (Boebling et al., 1996); consequently by knowing the changes in natural frequencies, it is possible to determine the extent of cracks or damages in a structure. However it is difficult to determine the location of the crack by this procedure since cracks at two different locations, associated with certain crack lengths or depths, may cause the same amount of frequency shift at certain modes. Hearn and Testa (1991) have pointed out that the magnitudes of changes for different natural frequencies is a function of the severity and location of defects in the structure. Therefore ratios of changes in natural frequencies, normalized with respect to the largest frequency change, are independent of severity for small flaws and can be utilized to indicate the defect locations directly. The theory was based on the concept that a single crack will affect each vibration mode differently, having a strong effect on certain modes and a weaker effect on others. This dissimilarity of effect on various modes (since it can be predicted) is the basis for the identification of damaged members. The procedure was stated as follows: Natural vibration

frequencies are to be measured periodically; when changes in natural frequencies are measured, the set of ratios of changes are computed and compared with the various member characteristic ratio ensembles obtained from the equation:

$$\frac{\Delta\omega_i^2}{\Delta\omega_j^2} = \frac{\dfrac{\epsilon_N^T(\phi_i)\,k_N\,\epsilon_N(\phi_i)}{\Phi_i^T M \Phi_i}}{\dfrac{\epsilon_N^T(\phi_j)\,k_N\,\epsilon_N(\phi_j)}{\Phi_j^T M \Phi_j}} \tag{2.2}$$

where $\Delta\omega_i$ and $\Delta\omega_j$ are the changes of the natural frequency of ith and jth modes, respectively, due to cracking; ϵ_N are the Nth member deformations and have the following relationships with displacement mode shapes and stiffness/mass matrices of the whole structure:

$$\phi_i^T K \phi_i = \sum \epsilon_N^T(\phi_i)\,k_N\,\epsilon_N(\phi_i) \tag{2.3a}$$

$$\phi_i^T M \phi_i = \sum \epsilon_N^T(\phi_i)\,M_N\,\epsilon_N(\phi_i) \tag{2.3b}$$

where ϕ_i is the ith displacement mode shape, M the mass of the structure, K the stiffness matrix of the whole structure and k_N the stiffness of Nth member. The location of crack is determined by selecting the member characteristic ensemble that most closely matches the observed ratios of frequency changes. This method can identify the location of cracked members of the structure. This method is more suitable for a truss-type structure where k_N is easy to define.

Pandey et al. (1991) used changes in curvature mode shapes to determine the location of the damage. They examined a cantilever beam and a simply supported beam. Instead of displacement mode shapes, curvature mode shapes were calculated. Absolute differences between the curvature mode shapes for the intact and the damaged beam were calculated. The largest differences occurred at the damaged point. Therefore they stated that absolute differences of the curvature mode shapes between the intact and the damaged structures could be used to indicate the location of damage in the structure. Obtaining the curvature mode shapes in a complex structure is difficult, if not impossible. Also, the extent of damage in a structure cannot be found by this method.

Recently a study concerning both the severity and location of cracks in offshore structures was carried out by Swamidas and Chen (1992). They used strain gauges in modal testing, monitoring both the global and local changes in frequency and amplitude of strain frequency response functions. Also they carried out a finite element analysis for the modal response of the structure and determined the frequency response functions for displacements and accelerations. The results showed that local surface strain frequency response functions were very sensitive to the presence of cracking in the structure and was strongly recommended for the detection of cracking in structures. This method can give an approximate indication of cracking in the structure. Further investigation is needed to find out more accurate location and extent of cracking in a structure.

As pointed out in the previous paragraph, modal strains are very sensitive to local

damage. Chen and Swamidas (1993) conducted an experiment which showed that the amplitude of the strain frequency response function near the crack zone decreased considerably when the crack size increased. They reported that in the main column of a tripod tower platform model, with a diameter of 300 mm and a thickness of 3 mm, the amplitude of the local strain FRF at the first resonant frequency decreased by more than 60% when the crack became a through crack, with a crack length to circumference ratio of 1/10 (actual length 90 mm).They used accelerometers, linear variable displacement transducers (LVDT), and strain gauges in their experiment. They proposed a procedure to detect cracks in offshore structures from global sensors, such as accelerometers, to determine the natural frequency changes that occur in the structure. When there is a change in the natural frequencies of the structure, there is a possibility that a crack has started to grow. Local sensors (strain gauges applied in critical areas of the structure) are then monitored to find the location and magnitude of the crack. Later, Chen (1993) carried out a systematic theoretical study of the behaviour of a plate with a small growing surface crack using the finite element method, including static, steady state, resonant and transient response analyses. By comparing the sensitivity of different parameters to cracking, it was found that besides natural frequencies of the structure and amplitude of the response, some of the most sensitive parameters to cracking were the difference of the strain mode shapes and local strain FRFs. Again, the method can only give an indication and not the extent of cracking in a structure.

In addition to the literature reviewed above, many other researchers have also carried out studies on the behaviour of structures with cracks. Collins et al. (1992) studied the free and

forced longitudinal vibrations of a cantilever bar with a crack, and the effect of the crack location and compliance on the fundamental natural frequencies was determined. Chondros and Dimarogonas (1989) studied the change in natural frequencies and modes of vibration of the structure with a given geometry for a crack. Earlier (1980), they had investigated the relationships between the change in natural frequency of vibration of a cantilever beam and the crack depth that occurred at welded junctions.

From the literature reviewed above, it can be observed that by monitoring the changes in modal parameters, which include natural frequencies, mode shapes, strain mode shapes, curvature mode shapes, residues or amplitude of FRFs, etc., damages occurring in structures can be found, and the approximate location and severity of the crack can also be obtained. But in all the reviewed literature, no method is available to locate cracking in complex structures very accurately, that gives the location along with length and depth of a crack.

2.2.2 System identification/model updating procedures

Doebling et al. (1993) carried out an experimental investigation on damage detection of a truss structure by a model updating procedure. They presented a damage detection algorithm based on a particular finite element updating scheme. First they expanded the experimental data so that the experimental model can be described in all finite element model degrees-of-freedom (DOFs). Then they used a Sensitivity Based Element By Element (SB-EBE) updating algorithm which relies on an unconstrained minimization of modal dynamic residual

$$R_m = KU_m - MU_m\Omega_m^2 \tag{2.4a}$$

for m experimental eigen-modes, and of static residuals

$$R_n = KU_n - F_n \tag{2.4b}$$

for n experimental static modes, where K and M are the stiffness and mass matrices, respectively; U_m, U_n are measured mode shape matrix (expanded to have DOFs of the finite element model); Ω_m is mth eigenvalue; and F_n is the loading for static deflection curves. Young's modulus and density of various truss members were reduced to simulate the damage in the structure.

From their paper it was shown that the algorithm worked very well for a cantilevered truss structure, but had trouble locating the damage in a suspended truss with several concentrated masses. They believed that the reason for this was the modal complexity of the structure. They concluded that the choice of modes in the modally complex structure is critical to the success of the algorithm, and to detect damage in the structure with highly localized modal mechanics, it was necessary to consider high frequency modes as well.

Kim et al. (1995) developed a two-step approach to identify the location and extent of structural damages. First, a general area of structure damage was located by minimizing the following function

$$\text{minimize } \theta = 1/2 \left\| M_{au}^{1/2} (K_{td} - K_{au}) M_{au}^{-1/2} \right\| \tag{2.5a}$$

subject to

$$K_{td}^{T} \phi_{td} = M_{au} \phi_{td} \Omega_{td}^{2} \tag{2.5b}$$

and

$$K_{td} = K_{td}^{T} \tag{2.5c}$$

where K, M are the stiffness and mass matrix, respectively; ϕ is the modal matrix; and subscripts au and td represent analytical/undamaged and test/damaged, respectively. The location and extent of the damage can be identified by examining $K_{td} - K_{au}$.

This approach can only identify a general area of structural damage when instrumentation is limited. So the second method, using a perturbation based approach, was developed to carry out a more detailed investigation on damage detection. The basic theory can be expressed as follows:

The design vector, which includes physical properties such as cross-sectional area and moment of inertia, is defined as:

$$\mathbf{u} = [u_1 u_2 \cdots u_d]^T \tag{2.6a}$$

The state vector, which includes frequencies and mode shapes, is defined as

$$\mathbf{v} = [v_1 v_2 \cdots v_s]^T \tag{2.6b}$$

Using linear perturbation theory, the modified state vector, $\mathbf{v}^m$, with respect to the change in design vector $\Delta\mathbf{u}$ can be approximated without solving the eigenvalue problem as,

$$\mathbf{v}^m = \mathbf{v}^0 + \Delta\mathbf{v} \doteq \mathbf{v}^0 + Q\Delta\mathbf{u} \tag{2.6c}$$

where $\mathbf{v}^0$ is the original state vector calculated from the undamaged analytical model, $\Delta\mathbf{v}$ is the change of state vector, and Q is a sensitivity matrix. The optimal design vector, which contains the damage information of the structure, can be found by iteratively minimizing the difference between the test results and the modified analytical results with least changes to the analytical model:

$$\text{minimize } \theta = \text{function of } \left[\frac{\mathbf{v}^t - \mathbf{v}^m}{\mathbf{v}^t}\right] + \text{function of } \left[\frac{\Delta\mathbf{u}}{\mathbf{u}^0}\right] \tag{2.6d}$$

where $\mathbf{u}^0$ is the original design vector used in the undamaged analytical model; and $\mathbf{v}^t$ includes frequencies and mode shapes obtained from modal testing of the damaged structure. The method was successfully applied to detect damaged members in a long hexagonal truss with total of 224 members.

Kaouk and Zimmerman (1993) conducted an experiment on cantilevered truss structures. They developed a theory which approached the damage location and extent in a decoupled manner. The original finite element model and a subset of measured eigenvalues and eigenvectors were used in this technique. First, a theory was developed to determine the location of structural damage. With the location determined, the extent of damage was then estimated. The damage extent algorithm was a minimum rank perturbation procedure, which was consistent with the effects of many classes of structural damage in a finite element model. They tested fifteen damage cases. The damage was clearly located in eleven cases. In two cases, the damage location was determined with further analysis. In one case, the location of damage was narrowed down to within two struts. The location algorithm failed in one case. On the other hand, the extent algorithm performed well for all cases where the damage was located.

Salawu and Williams (1993) compared four different methods of structural damage detection using modal analysis. A simulation analysis of a simply supported steel beam was performed using four methods. One method used changes in natural frequencies and mode shapes to locate the damage area, while the other three methods utilized system identification/model updating procedures. The authors concluded that the procedures they used in their paper were quite attractive, and the effectiveness of the three model updating procedures could have been affected by the choice of the system identification method.

The methods reviewed here were able to detect the cracks, relatively accurately, for truss-type structures. The severity of the damage for this kind of structure is mostly simulated

by cutting off one or more members, or by reducing the stiffness of one or more elements where the crack was located. It must also be pointed out that for the location of the crack, all the methods mentioned above had to check all the elements in the structure, which would be very time consuming for a complex structure. No publication is available in the open literature which gives the location and the accurate extent (length and depth) of crack(s) in plate-type structures.

2.3 Other Nondestructive Evaluation Techniques

Besides vibration techniques using modal analysis many other NDE techniques are available for crack detection. Harris and Heyman (1993) reviewed some of the NDE procedures that were considered in the research activities of the NASA airframe structural integrity program for the aging commercial transport fleet, which included thermal methods, ultrasonics, radiographic methods, magnetic particle methods and optical methods. Newton (1990) outlined some new development of techniques for underwater inspection of offshore structure, which included eddy current system and ultrasonic methods. Rogers (1987) published a paper that outlined the use of acoustic emission method for detection and monitoring of cracks in offshore structures. Guigne et al. (1992) used acoustic intensity and pressure measurements for fatigue crack detection applications.

Some of the methods mentioned above are well developed, widely used and are available in the market (such as ultrasonics, eddy current, magnetic particle imaging, etc.). Hundreds of papers have been published in these areas, while the others (such as acoustic intensity

measurements) are still undergoing development. Each of these methods has its own advantages and disadvantages for specific applications. For example, in offshore structures, most of the methods mentioned above require divers for underwater inspection each time an inspection becomes necessary. Another interesting feature that most of these methods have in common (except acoustic measurement) is that they measure the crack in a static mode. It will be interesting to see how the dynamic behaviour of the structure would change when cracks occur in the structure, and how the detection and sizing of cracks should be carried out under such context.

Another new NDE technique which is worth being mentioned here is the additive/subtractive decorrelated electronic speckle pattern interferometry (ESPI), which is undergoing development at California Institute of Technology and Northwestern University (Pouet, 1993). This method uses the speckle phase decorrelation between successively subtracted correlated speckle images, each of which contains information about the same two states of deformation of a test object undergoing vibration stressing. Based on the correlation fringes observed on the screen of the monitor, the displacement fields associated with changes in the state of the specimen can be determined, and the location of cracks can be monitored directly on the screen when discontinuity of the fringe patterns occur. This technique provides real time monitoring and can show crack opening and closing on the screen, which is attractive for the better understanding of fatigue cracking in structures.

2.4 Summary

During recent years, many investigations have been carried out for crack detection and assessment using various techniques. Vibration techniques using modal testing and analysis have also attracted a lot of attention because of their unique characteristics of investigating the structure in a dynamic mode and global sense. Earlier investigations using modal testing mainly focused on natural frequency shifts. Recently other modal parameters such as displacement/curvature/strain mode shapes, damping ratios and amplitudes of frequency response functions have also been investigated as sensitive indicators to cracking. With the availability of: (i) More accurate system identification procedures which utilize new modal techniques; (ii) Well developed finite element analysis procedures and degree-of-freedom condensation techniques, for matching the results of finite element and experimental models; and (iii) Various test analysis/identification algorithms and commercial softwares such as STAR STRUCT (Spectral Dynamics, Inc.), MODAL (Hewlett-Packard Co.), LMS CADA-X (LMS International), etc., the diagnostics of crack detection for preventive maintenance is gaining more attention.

As reviewed earlier, use of vibration techniques and model updating procedures for crack detection is still under development, and most of the available methods have been applied only to truss- and frame- type structures. The present study as given in the subsequent chapters extends this technique further, and applies it to a plate-type structure. A model updating procedure, which combines the results of experimental and finite element analyses, is used to

identify a fatigue crack in a plated T-joint. The study has carried out a detailed implementation of the procedure to a plate-type structure, combining it with the strain mode shape changes for approximate crack location and for accurate estimation of crack profiles (location, length, and depth). The procedure uses the currently available techniques of system identification, incorporating a perturbation based optimization procedure. Shallow shell elements have been used in the finite element model, so that the model updating procedure could be applied to any plate-type structure.

CHAPTER 3

BASIC THEORIES

3.1 Modal Analysis and Testing

3.1.1 Multi-Degree-Of-Freedom (MDOF) system theory

Modal analysis deals with the method of determining basic vibration properties of a general linear structure. It is based on the concept that the structure's behaviour can be described by a set of vibration modes: the modal model. This model is defined by a set of natural frequencies with corresponding vibration mode shapes and modal damping factors.

For the typical theoretical route to vibration analysis (by modal analysis), one begins with the description of the structure's physical characteristics, usually in terms of its mass, stiffness and damping properties. Then an analytical modal analysis is performed, and the modal model determined. Finally, the response of the structure to a given excitation is obtained.

The governing equations for vibration of the structure are expressed as:

$$[M]\{\ddot{U}\} + [C]\{\dot{U}\} + [K]\{U\} = \{F(t)\} \tag{3.1}$$

where [M], [C] and [K] are the mass, damping and stiffness matrices, respectively, {U} is the displacement vector and F(t) is the applied time-dependent force.

Applying Laplace transform to the equation:

$$\mathcal{L}\left([M]\{\ddot{U}\} + [C]\{\dot{U}\} + [K]\{U\}\right) = \mathcal{L}\left(\{F(t)\}\right) \tag{3.2}$$

one obtains:

$$[B(s)]\{U(s)\} = \{F(s)\} + ([M]s + [C])\{U(0)\} + [M]\{\dot{U}(0)\} \tag{3.3}$$

where

$$[B(s)] = [M]s^2 + [C]s + [K] \tag{3.4}$$

Rearrangement of the above equation leads to

$$\{U(s)\} = [H(s)]\left(\{F(s)\} + ([M]s + [C])\{U(0)\} + [M]\{\dot{U}(0)\}\right) \tag{3.5}$$

where $[H(s)] = [B(s)]^{-1}$ is called the transfer function matrix.

For the homogeneous solution:

$$[B(s)]\{U(s)\} = 0 \tag{3.6}$$

The characteristic polynomial equation is obtained from:

$$p(s) = \det[B(s)] = 0 \tag{3.7}$$

where the Laplace variable $s = \sigma + j\omega$

The roots s_i of the characteristic equation are called eigenvalues. Substituting the eigenvalues into the equation of motion and solving for $\{U\}$ yields the associated eigenvectors:

$$[B(s_i)]\{U_i\} = \{0\} \tag{3.8}$$

where s_i is the ith eigenvalue and U_i is the associated eigenvector. The eigenvalue s_i (or sometimes called complex natural frequency) has two parts: (i) the imaginary part which gives the damped natural frequency; (ii) the real part which gives the damping factor.

It can be shown that modal vectors are orthogonal with respect to one another if they are weighted with respect to the stiffness matrix [K] and mass matrix [M]. It can also be shown that modal vectors are orthogonal to one another if they are weighted with respect to the damping matrix [C], when the damping matrix is proportional to the mass matrix and stiffness matrix (the proportionally damped system).

Eqn. (3.1) can also be written in the modal space. The transformation from physical

space to modal space is given by

$$\{U\}_{nx1} = [\phi]_{nxm}\{p\}_{mx1} \tag{3.9}$$

where:

{U}: displacement of the physical degrees of freedom,

$[\phi]$: modal matrix. $[\phi] = [\phi_1, \phi_2, \ldots, \phi_m]$,

{p}: displacement in modal space,

n: number of physical degrees of freedom, and

m: number of modes considered in the study.

Using Eqn. (3.9), Eqn. (3.1) can be written as:

$$[M][\phi]\{\ddot{p}\} + [C][\phi]\{\dot{p}\} + [K][\phi]\{p\} = \{F(t)\} \tag{3.10}$$

Pre-multiplying by $[\phi]^T$, we get:

$$[\phi]^T[M][\phi]\{\ddot{p}\} + [\phi]^T[C][\phi]\{\dot{p}\} + [\phi]^T[K][\phi]\{p\} = [\phi]^T\{F(t)\} \tag{3.11}$$

For the proportionally damped system, using the orthogonality properties of the modal vectors weighted with respect to the mass, stiffness and damping matrices, one can define the diagonal modal mass matrix as:

$$[\bar{M}]_{modal} = [\phi]^T[M][\phi] \tag{3.12}$$

diagonal modal damping matrix as:

$$[\bar{C}]_{modal} = [\phi]^T[C][\phi] \tag{3.12a}$$

diagonal modal stiffness matrix as:

$$[\bar{K}]_{modal} = [\phi]^T[K][\phi] \tag{3.12b}$$

and modal force vector as:

$$\{\bar{F}\}_{modal} = [\phi]^T\{F\} \tag{3.12c}$$

Eqn. (3.1) can be written as:

$$[\bar{M}]_{mxm}\{\ddot{p}\}_{mx1} + [\bar{C}]_{mxm}\{\dot{p}\}_{mx1} + [\bar{K}]_{mxm}\{p\}_{mx1} = \{\bar{F}\}_{mx1} \tag{3.13}$$

It can be noticed that each equation is uncoupled from the other equation and represents an individual modal response of the system (Ewins, 1996).

As is often the case for real systems, the damping matrix is not proportional, and thus cannot be diagonalized as shown in the above derivation. The occurrence of non-proportional damping generally results in eigenvalues which are either negative real, or complex with

negative real parts. In the latter case both eigenvectors and eigenvalues exist as conjugate pairs. In handling cases like this a common procedure is to transform n coupled second order differential equations into 2n uncoupled first order equations. Fortunately, in most cases, especially in steel structures, the damping values are small, and can be treated as proportional. In this study, the damping matrix of the plated T-joint is treated as proportional matrix.

3.1.2 Frequency response function

Using Eqn. (3.5), the transfer function [H] can be expressed as follows:

$$[H] = [B]^{-1} = \frac{[D]}{\mathrm{Det}[B]} \tag{3.14}$$

where: [D]: adjoint matrix of [B]

Det [B]: Determinant of [B]

Since both the adjoint matrix of [B] and the determinant of [B] are polynomials of s, the elements of [H] are rational fractions of s. Therefore, it is possible to represent any element of the transfer function matrix [H] in a partial fraction form.

If it is assumed that the poles of the system are of unit multiplicity, and that the system is inherently underdamped (the poles occur in complex conjugate pairs) the transfer function can be expressed as:

$$H_{ij} = \sum_{r=1}^{n} \frac{A^{r}_{ij}}{s-\lambda_r} + \frac{A^{r*}_{ij}}{s-\lambda_r^*} \tag{3.15}$$

where

$$\lambda_r = -\zeta_r\omega_r \pm j\omega\sqrt{1 - \zeta_r^2} \tag{3.15a}$$

$$A_{ij}^{r} = U_{ir}U_{jr} \tag{3.15b}$$

λ_r is called the system pole, and λ^*_r is its complex conjugate; A_{ij}^r is called the residue of the rth mode (or sometime it's called modal constant), and A_{ij}^{r*} is its complex conjugate; ω_r is the rth natural frequency; ζ_r is the critical damping ratio of rth mode; and ϕ_{ir} is an element in modal matrix $[\phi]$.

From Eqn. (3.5), assuming zero initial conditions, one obtains:

$$[H(s)] = \frac{\{U(s)\}}{\{F(s)\}} \tag{3.16}$$

If the Fourier variable $s = j\omega$, then we have:

$$[H(j\omega)] = \frac{\{U(j\omega)\}}{\{F(j\omega)\}} \tag{3.17}$$

where $[H(j\omega)]$ is called the Frequency Response Function (FRF).

The frequency response function has many forms in terms of input (excitation) and output (response). The traditional forms include:

(a) receptance, in the form of (displacement)/(force), where displacement is the output.

(b) mobility, in the form of (velocity)/(force), where velocity is the output.

(c) inertance, in the form of (acceleration)/(force), where the acceleration is output.

Recently other forms such as slope, curvature, strain, bending moments etc., per unit applied force, have been discussed. It must be noted that in all these cases, the input is the excitation force.

Strain frequency response function

During the past decade, the consideration of surface strains has been introduced into modal analysis. The strain frequency response function is the transform function between output (surface strain level at a certain point) and input (the excitation force) in the frequency domain. The derivation of the strain frequency response function using finite element method is described as given below [Bernasconi and Ewins (1989), and Li et al. (1989)].

Eqn. (3.9) can also be written as

$$\underline{U} = \sum_{r=1}^{m} p_r(t)\phi_r(x,y,z) \qquad (3.18)$$

where

$$\underline{U} = \begin{Bmatrix} u \\ v \\ w \end{Bmatrix}$$

From the theory of elasticity, strain in x-direction can be written as

$$\epsilon_x = \frac{\partial u}{\partial x} = \sum_{r=1}^{m} p_r \psi_r(x,y,z) \tag{3.19}$$

and

$$\psi_r = \frac{\partial \phi_r}{\partial x} \tag{3.20}$$

where ψ_r is the strain mode shape of rth mode in x-direction (or some times called modal strain). Similar expressions could be written for ϵ_y, ϵ_z, γ_{xy}, γ_{yz}, and γ_{zx} and can be derived in the same way. Strain at a point should be a tensor. But usually only the normal strains are measured.

Using the finite element method, strain can be expressed as

$$\{\epsilon\} = [A]\{U\} \quad \text{or} \quad \{U\} = [A]^{-1}\{\epsilon\} \tag{3.21}$$

where [A] is the strain-displacement matrix. Substituting Eqn. (3.21) into Eqn. (3.1), one obtains

$$[M']\{\ddot{\epsilon}\} + [C']\{\dot{\epsilon}\} + [K']\{\epsilon\} = [A]^{-T}\{f(t)\} \tag{3.22}$$

where

$$[M'] = [A]^{-T}[M][A]^{-1} \tag{3.23}$$

$$[C'] = [A]^{-T}[C][A]^{-1} \tag{3.24}$$

$$[K'] = [A]^{-T}[K][A]^{-1} \tag{3.25}$$

Similar to displacement, the solution of Eqn. (3.22) has the form of

$$\{\epsilon\} = [\psi]\{p'\} = \sum_{r=1}^{m} p_r'\{\psi_r\} \tag{3.26}$$

where p_r' is the strain modal coordinate.

Substituting Eqn. (3.26) into Eqn. (3.22), and premultiplying with $[\psi]^T$, one obtains

$$[\psi]^T[M'][\psi]\{\ddot{p}'\} + [\psi]^T[C'][\psi]\{\dot{p}'\} + [\psi]^T[K'][\psi]\{p'\} = [\psi]^T[A]^{-T}\{f(t)\} \tag{3.27}$$

Since

$$\{\epsilon\} = [A]\{U\} \tag{3.28}$$

therefore

$$[\psi] = [A][\phi] \tag{3.29}$$

Then

$$\begin{aligned}[\psi]^T[M^c][\psi] &= ([A][\phi])^T([A]^{-T}[M][A]^{-1})([A][\phi]) \\ &= [\phi]^T[M][\phi] \\ &= [\bar{M}]_{modal}\end{aligned} \tag{3.30}$$

Similarly

$$[\psi]^T[C^c][\psi] = [\bar{C}]_{modal} \tag{3.31}$$

$$[\psi]^T[K^c][\psi] = [\bar{K}]_{modal} \tag{3.32}$$

$$[\psi]^T[A]^{-T} = [\phi]^T \tag{3.33}$$

Rewriting Eqn. (3.27), one obtains

$$[\bar{M}]_{modal}\{\ddot{p}'\} + [\bar{C}]_{modal}\{\dot{p}'\} + [\bar{K}]_{modal}\{p'\} = [\phi]^T\{f(t)\} \tag{3.34}$$

Eqn. (3.34) is the same as Eqn. (3.13); therefore $p_r' = p_r$, which means the strain modal coordinate $p_{r'}$ is the same as the displacement modal coordinate p_r defined in section 3.1.1.

Similar to displacements, if one assumes $f(t) = \{F\}e^{j\omega t}$, the solution of Eqn. (3.22) has the form of

$$\{\epsilon\} = [\psi][Y_r]_{diag}[\phi]^T = [H']\{F\} \tag{3.35}$$

where

$$Y_r = (K_r - \omega^2 M_r + j\omega C_r)^{-1} \tag{3.36}$$

Then the strain transfer function

$$[H'] = [\psi][Y_r][\phi]^T \tag{3.37}$$

As in displacement, the strain transfer function can also be expressed in the following form

$$H_{ij}' = \sum_{r=1}^{m} \frac{A_{ijr}'}{s-\lambda_r} + \frac{A_{ijr}'^*}{s-\lambda_r} \tag{3.38}$$

where $A_{ijr}' = \psi_i\phi_{jr}$ is the residue.

3.1.3. Modal parameter extraction

Frequency response function of a structure can be obtained experimentally by measuring the excitation input and the response output at various points of interest. The fundamental expression used in the derivation of FRFs was given in Eqn. (3.17). This states that an FRF is the complex ratio of response output to force input in the frequency domain. There are several formats which can be used in the derivation of the FRF. Each of these has a specific strength in terms of noise reduction. The three methods defined below are: the H_1 Estimator, the H_2 Estimator, the H_3 Estimator (SDRC, 1990).

The H_1 uses cross spectrum of response and force to the autospectrum of force,

$$H_1(\omega) = \frac{F^* \cdot U}{F^* \cdot F} = \frac{G_{FU}(\omega)}{G_{FF}(\omega)} \tag{3.39}$$

This method minimizes the effect of noise in response output.

The H_2 is defined as the ratio of the autospectrum of response to the cross spectrum of force and response,

$$H_2(\omega) = \frac{U^* \cdot U}{U^* \cdot F} = \frac{G_{UU}(\omega)}{G_{UF}(\omega)} \tag{3.40}$$

This estimator reduces the effect of noise present in input signals while computing the FRF.

The H_3 is the average of H_1 and H_2.

$$H_3(\omega) = \frac{H_1(\omega) + H_2(\omega)}{2} \tag{3.41}$$

There are some other estimators, which minimize the influence of noise in both input and output signals. One of them is called H_v (SDRC, 1990).

From these FRFs, modal parameters such as natural frequencies, damping ratios, and mode shapes can be extracted. The techniques that are widely used, most suitable for lightly damped and well separated modes, are peak searching, polynomial and circle fitting techniques. Some other methods such as complex exponential technique, Ibrahim time domain approach, polyreference technique, etc. are more suitable for closely coupled modes or heavily damped structures (Allemang, 1993). The theories for the three curve fitting techniques, namely, peak searching, polynomial and curve fitting techniques, are described in Appendix I.

3.2 Finite Element Method

3.2.1. General equations of finite element analysis

Consider the equilibrium of a general three-dimensional body such as that shown in Figure 3.1. The external statical forces acting on the body (shown in Figure 3.1) are surface tractions $\mathbf{f}^S$, body forces $\mathbf{f}^B$ and concentrated forces $\mathbf{F}^i$. These forces have three components corresponding to the three coordinate axes:

$$\mathbf{f}^S = \begin{bmatrix} f_X^S \\ f_Y^S \\ f_Z^S \end{bmatrix}; \quad \mathbf{f}^B = \begin{bmatrix} f_X^B \\ f_Y^B \\ f_Z^B \end{bmatrix}; \quad \mathbf{F}^I = \begin{bmatrix} F_X^I \\ F_Y^I \\ F_Z^I \end{bmatrix} \tag{3.42}$$

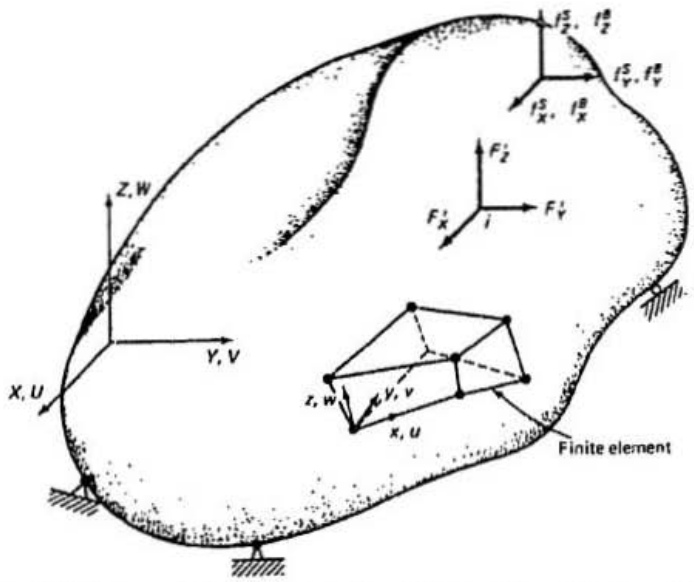

Figure 3.1 General three-dimensional body (from Bathe, 1982)

The displacements of the body, as shown in Figure 3.1, are **U** where

$$\mathbf{U}^T = [U \; V \; W] \tag{3.43}$$

The strains corresponding to **U** are,

$$\epsilon^T = [\epsilon_{XX} \; \epsilon_{YY} \; \epsilon_{ZZ} \; \gamma_{XY} \; \gamma_{YZ} \; \gamma_{ZX}] \tag{3.44}$$

and the stresses are

$$\tau^T = [\tau_{XX}\ \tau_{YY}\ \tau_{ZZ}\ \tau_{XY}\ \tau_{YZ}\ \tau_{ZX}] \tag{3.45}$$

Applying the principle of virtual displacements, the total internal virtual work done is equal to the total external virtual work; hence we have,

$$\int_V \bar{\epsilon}^T \tau dV = \int_V \bar{U}^T f^B dV + \int_S \bar{U}^{ST} f^S dS + \sum_i \bar{U}'^T F' \tag{3.46}$$

where $\bar{\epsilon}$ and $\bar{U}$ are the virtual strains and virtual displacements.

In finite element analysis the body shown in Figure 3.1 is treated as an assemblage of discrete finite elements with the elements being interconnected at the nodal points on the element boundaries. The displacements measured in a local coordinate system x,y,z within each element are assumed to be functions of displacements at the N nodal points. Therefore, for element m we have (Bathe, 1982)

$$\mathbf{U}^{(m)}(x,y,z) = \mathbf{N}^{(m)}(x,y,z)\hat{\mathbf{U}} \tag{3.47}$$

where $\mathbf{N}^{(m)}$ is the displacement interpolation matrix, and $\hat{\mathbf{U}}$ is a vector of the three global displacements U_i, V_i and W_i at all nodal points.

$$\hat{\mathbf{U}}^T = [U_1 V_1 W_1\ U_2 V_2 W_3\ \ldots\ U_N V_N\ W_N] \tag{3.48}$$

or we can write more generally

$$\hat{\mathbf{U}}^T = [U_1 U_2 \ldots U_n] \tag{3.49}$$

The strain distributions within the element now can be determined from

$$\epsilon^{(m)}(x, y, z) = \mathbf{A}^{(m)}(x, y, z)\hat{\mathbf{U}} \tag{3.50}$$

where $\mathbf{A}^{(m)}$ is the strain-displacement matrix.

The stresses in an element are related to the element strains and the element initial stresses, using the following equation.

$$\tau^{(m)} = \mathbf{C}^{(m)}\epsilon^{(m)} + \tau^{I(m)} \tag{3.51}$$

where $\mathbf{C}^{(m)}$ is the elasticity matrix of element m and $\tau^{I(m)}$ are the element initial stresses.

Rewriting the Eqn. (3.46), one obtains

$$\sum_m \int_{V^{(m)}} \bar{\epsilon}^{(m)T}\tau^{(m)}dV^{(m)} = \sum_m \int_{V^{(m)}} \bar{\mathbf{U}}^{(m)T}\mathbf{f}^{B(m)}dV^{(m)} + \sum_m \int_{S^{(m)}} \bar{\mathbf{U}}^{S(m)T}\mathbf{f}^{S(m)}dS^{(m)} + \sum_i \bar{\mathbf{U}}^{iT}\mathbf{F}^i \tag{3.52}$$

where m = 1, 2, ..., k and k is the number of elements. If we substitute Eqns. (3.47) - (3.51) into Eqn. (3.52), one obtains

$$\bar{\mathbf{U}}^T \left[\sum_m \int_{V^{(m)}} \mathbf{A}^{(m)T} \mathbf{C}^{(m)} \mathbf{A}^{(m)} dV^{(m)} \right] \hat{\mathbf{U}} = \bar{\mathbf{U}}^T \left[\left\{ \sum_m \int_{V^{(m)}} \mathbf{N}^{(m)T} \mathbf{f}^{B(m)} dV^{(m)} \right\} + \left\{ \sum_m \int_{S^{(m)}} \mathbf{N}^{S(m)T} \mathbf{f}^{S(m)} dS^{(m)} \right\} - \left\{ \sum_m \int_{V^{(m)}} \mathbf{A}^{(m)T} \boldsymbol{\tau}^{I(m)} dV^{(m)} \right\} + \mathbf{F} \right] \tag{3.53}$$

Denoting $\hat{\mathbf{U}} \equiv \mathbf{U}$, Eqn. (3.53) reduces to

$$\mathbf{K}\mathbf{U} = \mathbf{R} \tag{3.54}$$

where

$$\mathbf{R} = \mathbf{R}_B + \mathbf{R}_S - \mathbf{R}_I + \mathbf{R}_C \tag{3.55}$$

The load vector $\mathbf{R}_B$, due to body forces, is given by

$$\mathbf{R}_B = \sum_m \int_{V^{(m)}} \mathbf{N}^{(m)T} \mathbf{f}^{B(m)} dV^{(m)} = \sum_m \mathbf{R}_B^{(m)} \tag{3.56}$$

The effect of the surface forces are given by

$$\mathbf{R}_S = \sum_m \int_{S^{(m)}} \mathbf{N}^{S(m)T} \mathbf{f}^{S(m)} dS^{(m)} = \sum_m \mathbf{R}_S^{(m)} \tag{3.57}$$

and the effect of the elemental initial stresses are given by

$$\mathbf{R}_I = \sum_m \int_{V^{(m)}} \mathbf{A}^{(m)T} \boldsymbol{\tau}^{I(m)} dV^{(m)} = \sum_m \mathbf{R}_S^{(m)} \tag{3.58}$$

and that of the concentrated loads by

$$\mathbf{R}_C = \mathbf{F} \tag{3.59}$$

The stiffness matrix **K** can be determined from

$$\mathbf{K} = \sum_m \int_{V^{(m)}} \mathbf{A}^{(m)T} \mathbf{C}^{(m)} \mathbf{A}^{(m)} dV^{(m)} = \sum_m \mathbf{K}^{(m)} \tag{3.60}$$

For a dynamic problem, using d'Alembert's principle, the inertia forces can be included as part of body forces in Eqn. (3.56),

$$\mathbf{R}_B = \sum_m \int_{V^{(m)}} \mathbf{N}^{(m)T} [\mathbf{f}^{B(m)} - \rho^{(m)} \mathbf{N}^{(m)} \ddot{\mathbf{U}}] dV^{(m)} \tag{3.61}$$

where $\ddot{\mathbf{U}}$ is the nodal acceleration and $\rho^{(m)}$ is the mass density of element m. Now the equilibrium equations become,

$$\mathbf{M}\ddot{\mathbf{U}} + \mathbf{K}\mathbf{U} = \mathbf{R} \tag{3.62}$$

where **R** and **U** are time dependent. The mass matrix **M** can be determined by

$$\mathbf{M} = \sum_{m} \int_{V^{(m)}} \rho^{(m)} \mathbf{N}^{(m)T} \mathbf{N}^{(m)} dV^{(m)} - \sum_{m} \mathbf{M}^{(m)} \qquad (3.63)$$

In practice, damping always exists in any system. Hence the equilibrium equations should be of the following form,

$$\mathbf{M}\ddot{\mathbf{U}} + \mathbf{C}\dot{\mathbf{U}} - \mathbf{K}\mathbf{U} = \mathbf{R} \qquad (3.64)$$

This equation is the same as that given in Eqn. (3.1).

Determination of the general finite element damping matrix is quite difficult, if not impossible. As stated in 3.1, in most cases, the damping can be assumed to be proportional to the mass and stiffness of the system. So generally the damping matrix is constructed using the mass matrix and the stiffness matrix, together with experimental results.

3.2.2. Thin shell element

The thin shell element formulation is based on the theory of plates with transverse shear deformations, which assumes that "particles of the plate originally on a line that is normal to the undeformed middle surface remain on a straight line during deformation, and this line is not necessarily normal to the deformed middle surface". With this theory, the displacement components can be expressed as:

$$u = z\beta_x(x,y); \quad v = z\beta_y(x,y); \quad \text{and } w = w(x,y) \qquad (3.65)$$

where w is the transverse displacement, β_x and β_y are the rotations of the normal to the undeformed middle surface in the x-z and y-z planes, respectively, see Figure 3.2. With Kirchhoff plate theory, which states "a material line that is originally normal to undeformed middle surface remains normal to that surface throughout the deformation", $\beta_x = -\partial w/\partial x$, and $\beta_y = \partial w/\partial y$.

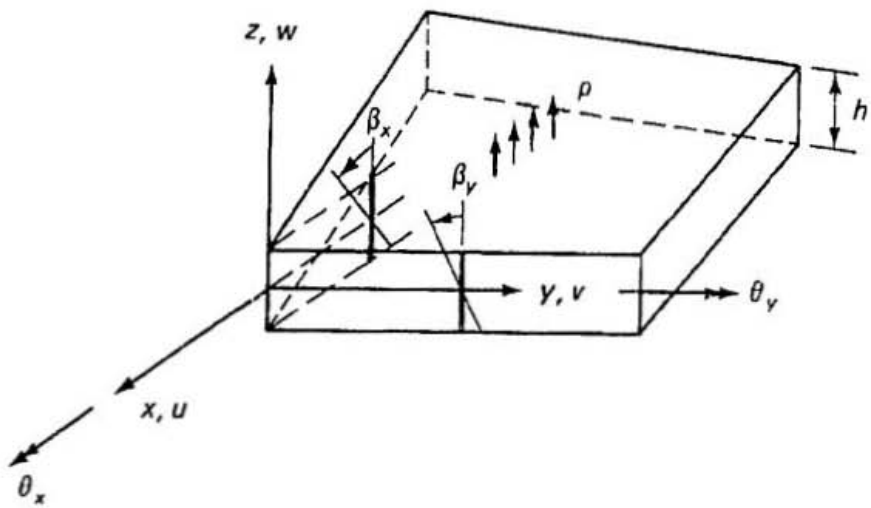

Figure 3.2 Deformations considered for a plate element

In linear analysis, the in-plane deformations present in the middle plane are not coupled with the out-of-plane deformations of w, β_x, β_y. Hence for clarity, the two types of deformations are treated separately and combined finally to give the total stiffness matrix for the element. The bending strains of the plate can be written as:

$$\begin{bmatrix} \epsilon_{xx} \\ \epsilon_{yy} \\ \gamma_{xy} \end{bmatrix} = z \begin{bmatrix} \dfrac{\partial \beta_x}{\partial x} \\ -\dfrac{\partial \beta_y}{\partial y} \\ \dfrac{\partial \beta_x}{\partial y} - \dfrac{\partial \beta_y}{\partial x} \end{bmatrix} \tag{3.66}$$

and the transverse shear strains are assumed to be constant through the thickness

$$\begin{bmatrix} \gamma_{yz} \\ \gamma_{zx} \end{bmatrix} = \begin{bmatrix} \dfrac{\partial w}{\partial y} - \beta_y \\ \dfrac{\partial w}{\partial x} + \beta_x \end{bmatrix} \tag{3.67}$$

The stresses can be written as:

$$\begin{bmatrix} \tau_{xx} \\ \tau_{yy} \\ \tau_{xy} \end{bmatrix} = z \frac{E}{1-\nu^2} \begin{bmatrix} 1 & \nu & 0 \\ \nu & 1 & 0 \\ 0 & 0 & \dfrac{1-\nu}{2} \end{bmatrix} \begin{bmatrix} \dfrac{\partial \beta_x}{\partial x} \\ -\dfrac{\partial \beta_y}{\partial y} \\ \dfrac{\partial \beta_x}{\partial y} - \dfrac{\partial \beta_y}{\partial x} \end{bmatrix} \tag{3.68}$$

$$\begin{bmatrix} \tau_{yz} \\ \tau_{zx} \end{bmatrix} = \frac{E}{2(1+\nu)} \begin{bmatrix} \dfrac{\partial w}{\partial y} - \beta_y \\ \dfrac{\partial w}{\partial x} + \beta_x \end{bmatrix} \tag{3.69}$$

and $\tau_{zz} = 0$.

The total potential of the plate element can now be expressed as:

$$\Pi = \frac{1}{2}\int_A\int_{-h/2}^{h/2}\begin{bmatrix}\epsilon_{xx} & \epsilon_{yy} & \gamma_{xy}\end{bmatrix}\begin{bmatrix}\tau_{xx}\\ \tau_{yy}\\ \tau_{xy}\end{bmatrix}dzdA + \frac{c}{2}\int_A\int_{-h/2}^{h/2}\begin{bmatrix}\gamma_{yz} & \gamma_{zx}\end{bmatrix}\begin{bmatrix}\tau_{yz}\\ \tau_{zx}\end{bmatrix}dzdA - \int_A wpdA \tag{3.70}$$

where c is a constant used to account for the actual nonuniformity of the shearing stresses. Substituting Eqn. (3.66) - (3.69) in Eqn. (3.70), one has

$$\Pi = \frac{1}{2}\int_A \boldsymbol{K}^T\boldsymbol{C}_b\boldsymbol{K}dA + \frac{1}{2}\int_A \boldsymbol{\gamma}^T\boldsymbol{C}_s\boldsymbol{\gamma}dA - \int_a wpdA \tag{3.71}$$

where

$$\boldsymbol{K} = \begin{bmatrix}\dfrac{\partial\beta_x}{\partial x}\\ -\dfrac{\partial\beta_y}{\partial y}\\ \dfrac{\partial\beta_x}{\partial y} - \dfrac{\partial\beta_y}{\partial x}\end{bmatrix};\quad \boldsymbol{\gamma} = \begin{bmatrix}\dfrac{\partial w}{\partial y} - \beta_y\\ \dfrac{\partial w}{\partial x} + \beta_x\end{bmatrix} \tag{3.72}$$

$$\boldsymbol{C}_b = \frac{Eh^3}{12(1-\nu^2)}\begin{bmatrix}1 & \nu & 0\\ \nu & 1 & 0\\ 0 & 0 & \dfrac{1-\nu}{2}\end{bmatrix};\quad \boldsymbol{C}_s = \frac{Ehc}{2(1+\nu)}\begin{bmatrix}1 & 0\\ 0 & 1\end{bmatrix} \tag{3.73}$$

Using the fact that the total potential must be stationary, Eqn. (3.71) becomes

$$\int_A \delta K^T C_b K dA + \int_A \delta \gamma^T C_s \gamma dA - \int_A \delta w \, p dA = 0 \qquad (3.74)$$

which may be regarded as the principle of virtual displacements for the plate element.

For the finite element analysis

$$w = \sum_{i=1}^{q} h_i w_i; \quad \beta_x = \sum_{i=1}^{q} h_i \theta_y'; \quad \beta_y = \sum_{i=1}^{q} h_i \theta_x' \qquad (3.75)$$

where h_i are the interpolation functions and q the number of nodes of an isoparametric plate element.

The more general shell may be constructed by superimposing the plate bending stiffness matrix and the plane stress stiffness matrix for membrane element. The major advantage of the general shell element formulation is that the geometry of any shell surface is represented accurately and all displacement compatibility conditions between elements are satisfied directly and in an

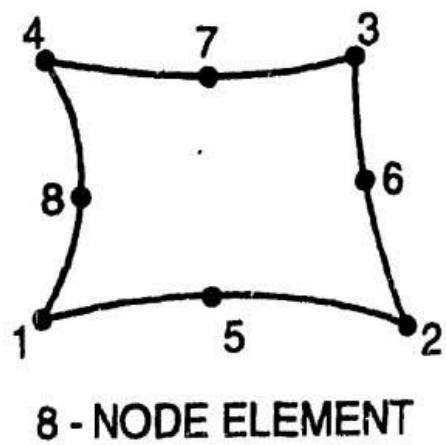

Figure 3.3 ABAQUS's S8R5 8-noded shell element

effective manner.

In this study, ABAQUS finite element analysis package (Hibbitt, Karlsson & Sorensen, 1995) was used, and shell element type S8R5 was used for most part of the plated T-joint. This type of element has 8 nodes (as shown in Figure 3.3), each node having five degrees of freedom. It is a doubly curved shell element, with 3x3 middle surface integration for mass, body forces and surface pressure calculation and a 2x2 integration for constitutive equation calculation and output. Five integration points are chosen through the shell thickness for stress and strain output; this is based on the conclusion from an earlier study (Nwosu, 1993).

3.2.3 Line spring element for modelling crack

Line spring element is designed to model part-through cracks in shell-type structures. It is based on replacing the part-through crack with an equivalent distributed spring which matches the compliance introduced into the structure by the crack. The stiffness of the spring varies with the crack depth a.

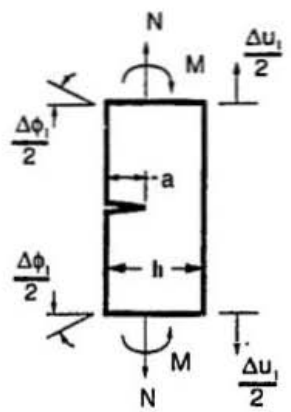

Figure 3.4 Single edge notched specimen

The stiffness calculation is

based on matching the local compliance of the crack with that of a single edge notched specimen (see Figure 3.4).

From Figure 3.4, assume that the specimen is under remote tension N, and moment M, with conjugate displacement Δu_1 and rotation $\Delta\phi_1$. Consider these as generalized forces $Q_1 = N$ and $Q_2 = M$ and conjugate generalized displacements $q_1 = \Delta u_1$ and $q_2 = \Delta\phi_1$. Since the stress intensity factor varies linearly with load, we can write

$$K_I = c_1 N + c_2 M = \sum_{i=1}^{2} c_i Q_i \tag{3.76}$$

where $K_I = K_I(a,h)$ are the stress intensity factors for a single edge notched specimen under unit remote tension or bending, which are known functions of the crack depth a, and specimen thickness h (refer to Hibbitt, Karlsson & Sorensen, Inc., 1991 "Fracture Mechanics Notes").

The complementary energy of the cracked single edge notched specimen is

$$\Omega_C = \frac{1}{2}[Q]^T[C][Q] \tag{3.77}$$

where $C_{ij}(a,t)$ is the compliance of the cracked specimen and

$$q_i = \sum_j C_{ij} Q_j \tag{3.78}$$

It is known that the stress intensity factor is related to the energy release rate per unit crack tip advance according to

$$\frac{K_I^2}{E/(1-\nu^2)} = G = \frac{\partial \Omega_C}{\partial a}\Big|_0 \tag{3.79}$$

Then

$$\frac{K_I^2}{E/(1-\nu^2)} = \frac{1}{2}[Q]^T \frac{\partial [C]}{\partial a}[Q] \tag{3.80}$$

Since K_I^2 is also defined as

$$K_I^2 = [Q]^T [c_1 \; c_2] \begin{bmatrix} c_1 \\ c_2 \end{bmatrix} [Q] \tag{3.81}$$

For any Q_i and Q_j, this defines the element of compliance matrix by

$$\frac{\partial C_{ij}}{\partial a} = \frac{2}{E/(1-\nu^2)} c_i c_j \tag{3.82}$$

which gives

$$C_{ij} = \frac{2}{E/(1-\nu^2)} \int_0^a c_i(s) c_j(s) ds \tag{3.83}$$

The stiffness for the line spring finite element model is simply $[K] = [C]^{-1}$.

The stiffness of the line spring per unit length of crack front is thus known from the

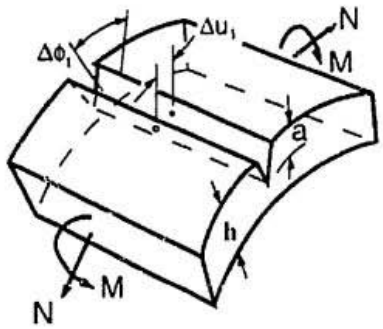

Figure 3.5 Line spring element

crack depth, and a distributed spring element can be constructed, linking the nodal displacements and rotations across the line spring to conjugate forces and moments (Figure 3.5).

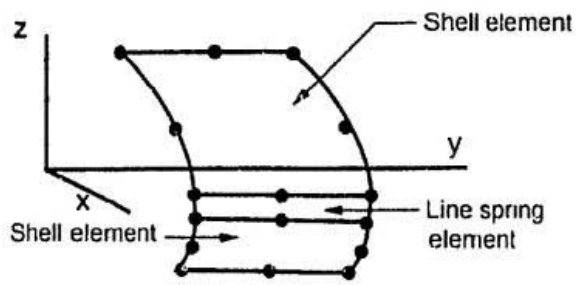

Figure 3.6 Line spring element in a shell mesh

This line spring element is then inserted into a shell mesh, to represent a part-through crack in the shell (Figure 3.6).

3.3 Model Updating for Damage Detection

The model updating for damage detection methods is based on the modification of structural model matrices such as mass, stiffness, and damping, to reproduce responses as closely as possible to the measured responses. These methods solve for the updated matrices (or perturbations to the nominal model which produce the updated matrices) by forming a constrained optimization problem based on the structural equations of motion, nominal model and measured data.

Many techniques have been investigated for the model updating procedure. Most of them use modal parameters in their objective functions. Some of them use experimental FRFs directly, which has the advantage that no curve fitting is needed. In this study, a two step approach similar to the approach used by Kim et al. (1995) is utilized.

First, an approximate crack area is located by examining the changes in the strain mode shape. From a previous study by Chen (1993), the changes in the strain mode shapes, especially the dominant mode shapes, gave a good indication of the location of the crack. The first dominant mode, which in this study is the first bending mode of the bottom plate, has the largest changes in modal strains in the area around the crack region. Also, for a known structure, it is

not possible, nor necessary, to apply strain gauges all over the structure, to obtain the strain mode shapes. Only those areas with high stress levels need to be examined. In this case, the modal strains obtained from those points are examined. Those points with large changes in the modal strains, are examined for possible crack formation. After that, a more detailed study using model updating procedure is used.

The basic idea for model updating is to minimize the error between the experimental and analytical models. There are many expressions for error functions and they depend on the parameters which are chosen for the objective function. Jeong and Nagamatsu (1992) suggested an approach in which the error function between analytical and experimental FRFs was used as the objective function. The error S is given by

$$S = \sum_{i=1}^{n}\sum_{j=1}^{m}\left\{W_{Rj}(\omega_i)\left[H_{Rj}^{a}(\omega_i) - H_{Rj}^{e}(\omega_i)\right]^2 + W_{Ij}(\omega_i)\left[H_{Ij}^{a}(\omega_i) - H_{Ij}^{e}(\omega_i)\right]^2\right\} \tag{3.84}$$

where W_{Rj} and W_{Ij} are the weighting coefficients, H^a is the analytical FRF and H^e the experimental FRF. The subscripts R and I denote, respectively, the real and imaginary parts of the complex value, m is the number of referenced FRF for identification, and n is the number of eigenvalues to be considered.

The use of FRFs directly, instead of other parameters such as natural frequencies or mode shapes, avoids curve fitting procedures, which introduce more errors in the whole

procedure. It would also be helpful in examining the regions of FRFs away from the resonant points.

One way to minimize the error S is to attach certain constraint conditions, and then use Lagrangian multipliers for these constraining conditions. The orthogonality of the modal matrix can be used as a constraining condition, and can be expressed as

$$[\phi][\phi]^T = [0] \quad \text{or} \quad g(Z) = 0 \tag{3.85}$$

where Z is a design parameter.

To minimize the error S, one can minimize the following function Λ by introducing the Lagrangian multiplier λ

$$\Lambda = S(Z) + \lambda g(Z) \tag{3.86}$$

The differentiation of Eqn.(3.86) with respect to Z must be zero; hence

$$\frac{\partial S(Z)}{\partial Z} + \lambda \frac{\partial g(Z)}{\partial Z} = 0 \tag{3.87}$$

Using Eqns. (3.85) and (3.87), the Lagrangian multiplier λ and the design parameter Z can be determined.

This method requires the calculation of $\partial S/\partial z$, which would require the computation of derivatives of FRFs [H^a and H^e in Eqn. (3.84)] with respect to the design parameters (crack location, length and depth). This requirement was found to be very difficult to implement in real structures unless an analytical expression for H in terms of design parameters was available. Hence a perturbation based approach is used in this thesis along with a modified form of Eqn. (3.84); the perturbation procedure described by Kim et al. (1995) is adopted and described as follows.

Let {Z} be the design vector, which is a function of location, length and depth of the crack.

$$\{Z\} = \begin{Bmatrix} D \\ L \\ C \end{Bmatrix} \tag{3.88}$$

where D, L and C are the depth, length and location of the crack, respectively.

The changes in H^a can be expressed as

$$\Delta H^a = Q\Delta Z \tag{3.89}$$

Using linear perturbation theory, the modified state vector, H^a, with respect to the change in design vector ΔZ can be approximated without solving the eigenvalue problem, as,

$$H_n^a = H_0^a + \Delta H^a \approx H_0^a + Q\Delta Z \tag{3.90}$$

where Q is called the sensitivity matrix.

The sensitivity matrix Q is a function of D, L and C. It is calculated by applying different line spring elements, to simulate various trial cracks, into the finite element model. Similar to the element by element approach used by Doebling et al. (1993), varying length and depth line spring elements are applied to different locations. This method is based on the idea that since an initial crack estimate has already been made, only a small area needs to be examined in detail for greater accuracy. The final design vector Z which minimizes the error S is designated as the final predicted crack with accurately determined crack depth, length and the location.

3.4 Summary

This chapter covers the basic theories that are used in this study. Section 3.1 discusses the basic theories of modal analysis and testing, provides guidance for experimental part of the study from which the dynamic characteristics such frequency response functions of strain/acceleration, natural frequencies, mode shapes and damping ratios are obtained. The theories of finite element analysis, which are needed to generate a finite element model through ABAQUS and obtain meaningful results, are discussed in Section 3.2. Finally, in Section 3.3, a model updating procedure, which uses two sets of data, one from the model testing, and the

other from the finite element analysis, is described. The updating procedure updates the finite element model by introducing different locations, lengths and depths of the crack into the finite element model, through the use of line spring elements, until the right crack profile is found (by the minimized error S). The model updating procedure minimizes the error using a perturbation approach.

CHAPTER 4

EXPERIMENTAL STUDY ON PLATED T-JOINTS UNDERGOING FATIGUE CRACKING

4.1 Methodology

Any physical changes that occur in a structure will inevitably cause changes in the physical properties. These changes normally will be expressed in terms of changes in mass, stiffness and/or damping of the structure. As mentioned earlier, a structure's dynamic behaviour can also be expressed in modal space, which is expressed in terms of natural frequencies, mode shapes and damping value. Therefore the characteristics of fatigue cracks (such as crack location, depth, width etc.) occurring in a structure, which change its physical properties, can be determined by examining the changes in the modal properties (or parameters).

As stated earlier, many research studies have been carried out using modal parameters

for crack detection. The first modal parameter that was used for crack detection was the natural frequency. The natural frequency of a structure is the most important modal parameter, and the easiest to obtain. Unfortunately the changes in natural frequencies, due to the presence of a fatigue crack or any other flaw, are very small. Also, it is difficult to find out the location of the crack if one uses the natural frequency alone.

In this study, the changes in experimental and analytical frequency response functions (FRFs) are used to identify and locate the crack. These FRFs would include all the dynamic parameters that need to be considered in any investigation, such as natural frequencies, modal damping ratios, mode shapes and other modal constants. In addition, FRFs could be obtained for displacements, velocities, accelerations, strains, stresses and any other variable that needs to be examined. Hence FRF seems to be the proper function that needs to be considered for crack detection and identification. The method of using the whole FRF instead of one or several of the modal parameters makes use of the advantage that modal parameter extraction procedure could be eliminated, resulting in less accumulation of errors in the numerical estimation techniques. Also, the structural response at both the resonant and non-resonant regions could be examined by this method.

From a previous study (Chen, 1993), it was observed that the surface strain FRF around the crack region gave a much better indication of cracking in plate-like structures than the displacement/acceleration FRFs. In this study, a detailed investigation is carried out using both experiments and analyses to verify the previous indications from theoretical studies. The

methodology used for experimental investigation was based on the fact that strain and acceleration FRFs experience changes when fatigue cracks initiate and propagate. In some cases, especially for strain FRFs at certain locations and certain directions, these changes are very significant. Therefore, strain gauges and accelerometers were used to record responses of the plated T-joints at salient points. Fatigue loading was applied to the structure to develop fatigue cracking at critical locations; after the crack had developed to an assumed level, modal testing/analysis was carried out to determine the frequency response functions. This was repeated for various stages of crack development until the specimen failed. The fatigue crack profiles, at different fatigue cracking intervals, were recorded using ink staining and beach marking procedures. Seven plated T-joint specimens were tested during the experimental part of this study.

4.2 Experimental Setup

4.2.1 Instrumentation for experiment

Two pieces of 16 mm thick structural steel plates were welded together to form a plated T-joint (see appendix II for the welding procedure specifications). Figure 4.1 shows the dimension of a single plated T-joint. Tensile testing was carried out to determine the Young's modulus of the steel; results are shown in Table 4.1. It is observed that the average value for E is 207.03 GPa with a variation of $\pm$ 6.2 %

Table 4.1 Young's modulus of steel used for plated T-joint

Young's modulus from test #1	Young's modulus from test #2
219.89 GPa	194.17 GPa

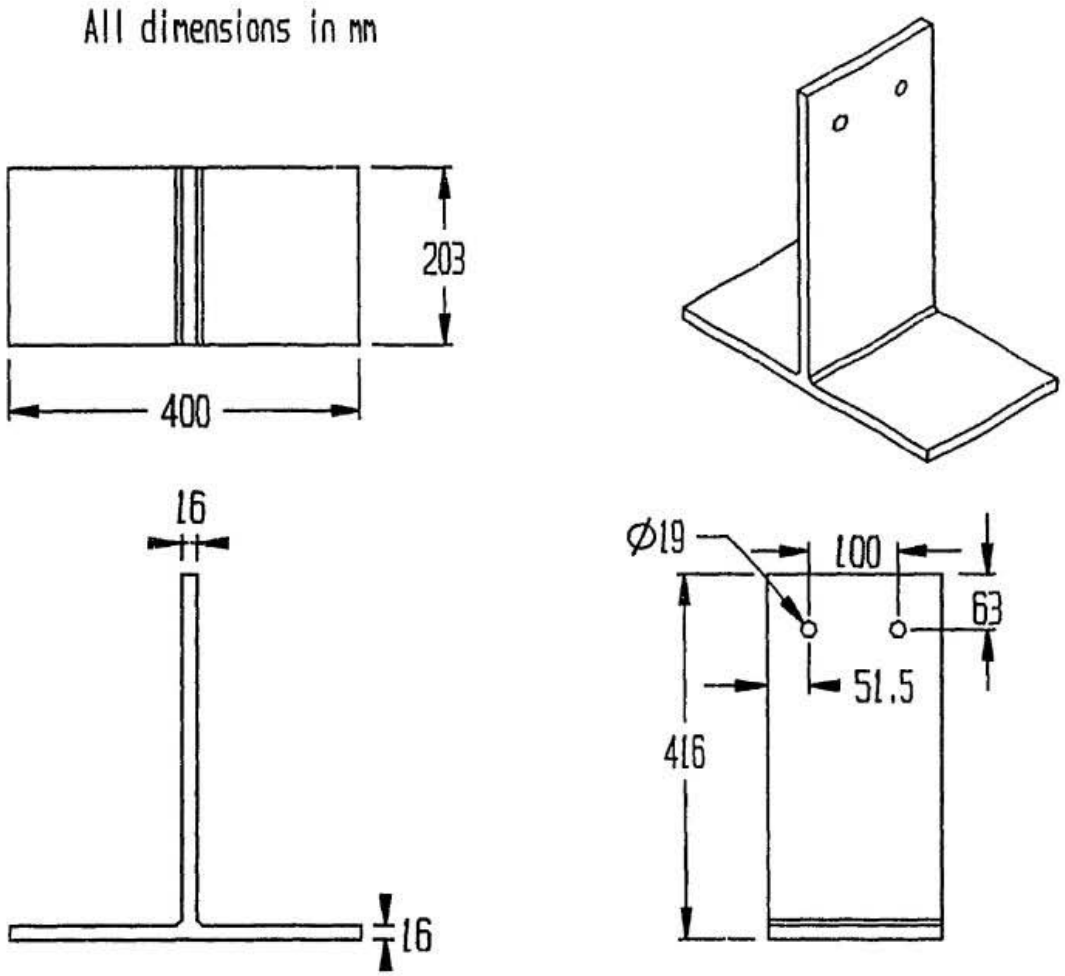

Figure 4.1 Dimensions of a plated T-joint

The plated T-joint was simply supported at both ends of the base plate. Since fatigue load was applied at both the upward and downward directions (cyclic load), the upward and downward movements of the base plate were restrained, at the supporting points; the rotations of the base plate were allowed at these points. To achieve these support conditions two cylindrical rods were placed, above and beneath the plate, at the supporting points. Figure 4.2 shows the supporting mechanism used for the plated T-joint.

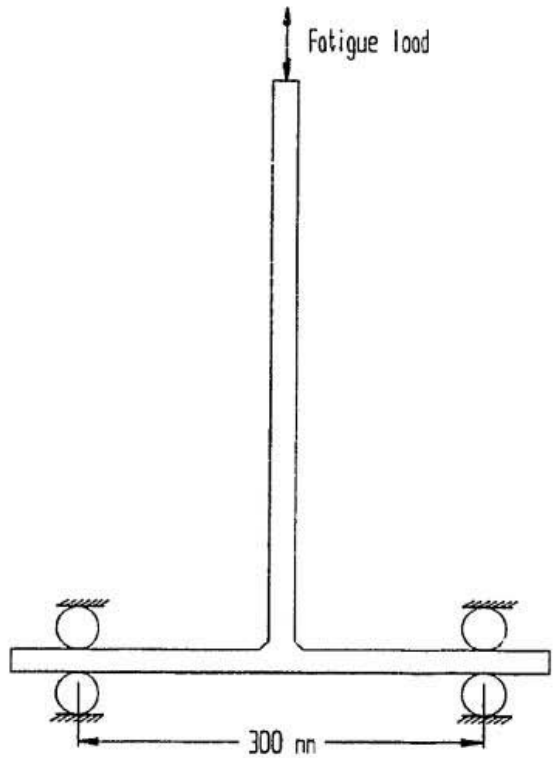

Figure 4.2 Supporting mechanism for the T-joint

The cylindrical rods were in turn connected to a solid steel frame, which was bolted onto the structural laboratory's 0.9 m thick concrete floor. Since stiff supporting conditions are needed for carrying out modal testing of the plated T-joint, the supporting frame was stiffened

at salient points and bolted onto the heavy floor at three points (325 N.m torque). During modal testing, the excitation frequencies were swept through a certain predefined frequency range; the range was selected so as to give better strain frequency response functions and usually the range included one or two natural frequencies. Any resonances other than that of the plated T-joint caused by supporting members would modify the results of modal testing. With the rigid support mechanism as shown above, the resonance effects caused by supporting members are reduced to a minimum. Figure 4.3 shows the photo of the actual experimental setup.

The fatigue load was applied to the attachment plate of the T-joint as shown in Figure 4.2. The connection between the actuator and plated T-joint was made through two equal angle steel sections bolted to the actuator using 12 mm diameter bolts (Figure 4.4). Figures 4.5 and 4.6, respectively, show the connection and disconnection of the actuator from the plated T-joint.

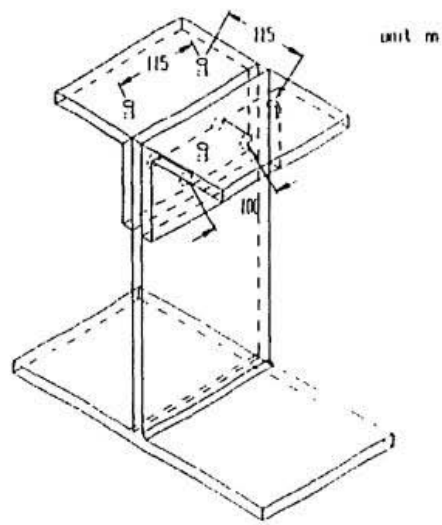

Figure 4.4 The connection between the plate and the actuator

During the fatiguing process, a cyclic sinusoidal fatigue load (as shown in Figure 4.7) was applied to the plated T-joint. The magnitude of the fatigue load was set so as to cause a nominal maximum weld-toe stress range of nearly 200 - 250 MPa. Some slight variation from these stress ranges occurred for different specimens.

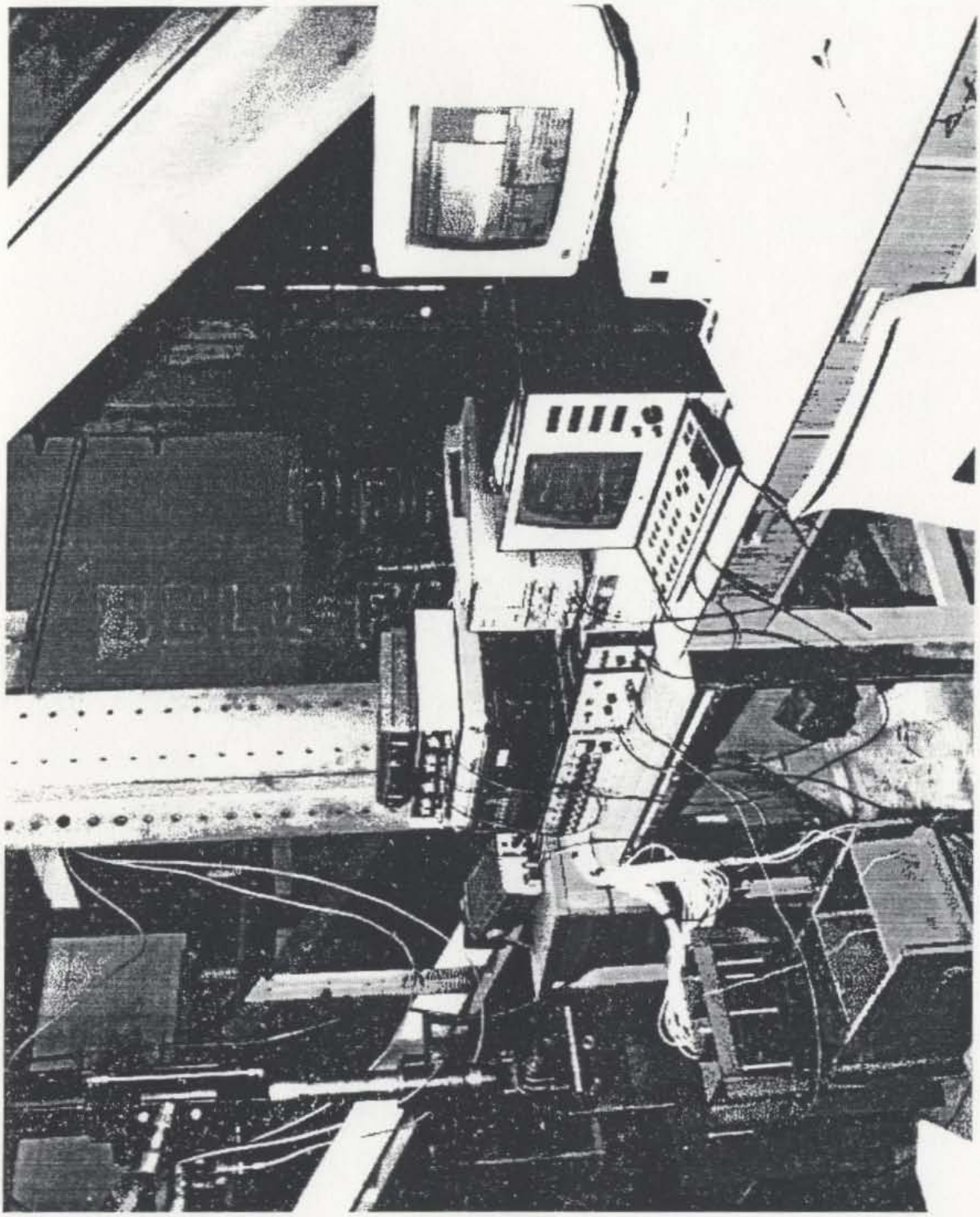

Figure 4.3 Photo of the whole experimental setup

The frequency of fatigue cycles was fixed at 5 Hz. This value was chosen mainly due to the limitation of the hydraulic pump, which reduced the maximum load output if operated at higher frequencies. Table 4.2 gives different fatigue loadings, load ratios and stress ranges near the weld toe as measured by the strain gauges for different specimens. The maximum stress range at the weld toe is calculated from the load range obtained as the difference between the maximum and minimum loads; the mean load was given by half the load range value.

To record the crack profile at each of the predefined fatigue interval, ink staining and beach marking techniques were utilized. For ink staining, which was made after the first crack initiation was observed (by eye using a magnifying glass), a slow drying red ink (made from finger nail polish diluted by 100 % pure isopropyl alcohol) was poured into the crack, while maximum fatigue load was held constant (till the ink dried); this ink staining (pink in colour) stays permanently and depicts the initial crack profile when the cracked plate is broken open. Beach marking technique is based on the fact that a fatigue crack propagates at a different rate when growing at a different fatigue frequency and stress level; this decrease in growth rate gives a distinct coloration to the cracking interface during the beachmark cycling. Therefore cycling the specimen at a different frequency and load level will form a mark at the crack surface similar to the mark observed at the beach during successive wave run ups (from where the name has come). In this study, beach marking procedure was performed at each of the predefined fatigue cycles, at a frequency of 10 Hz (twice the fatiguing frequency); the magnitude of the load range was reduced to half while keeping P_{mean} as constant.

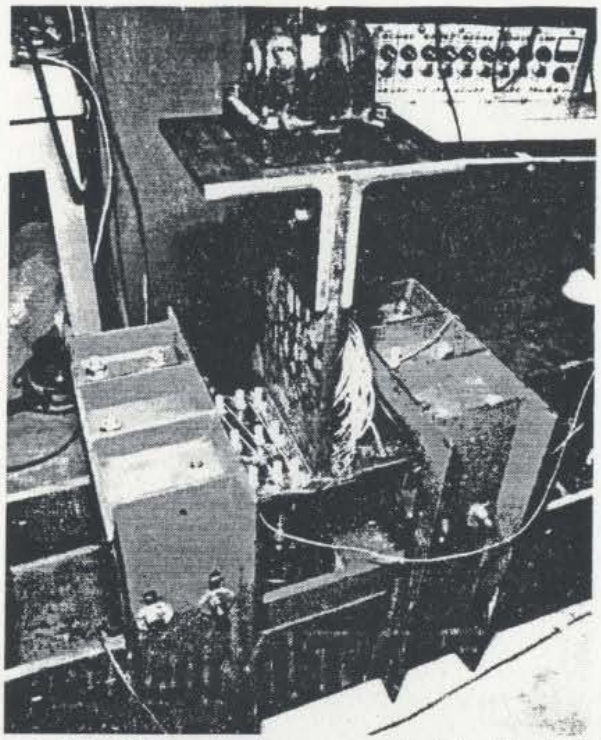

Figure 4.5 The actuator connected to the T-joint

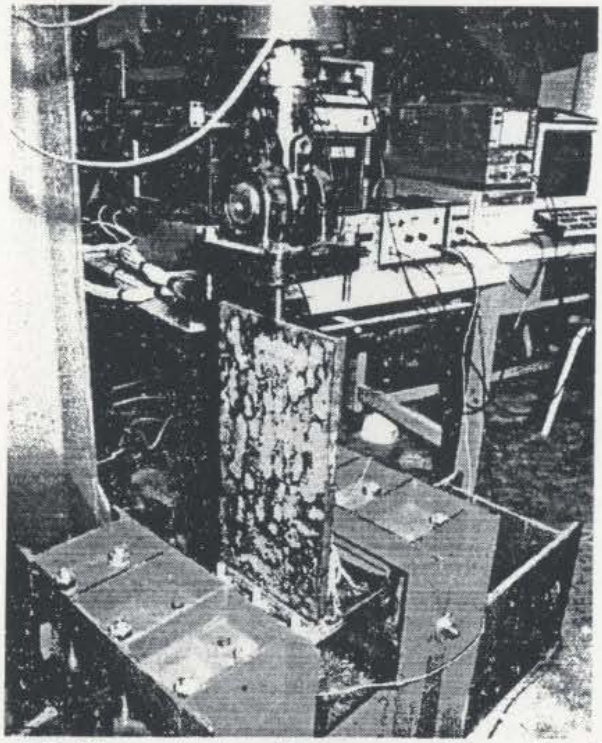

Figure 4.6 The actuator disconnected from the T-joint

Table 4.2 Fatigue loads and stress ranges used for different plated T-joint specimens

Specimen #	P_{max} (KN)	P_{min} (KN)	P_{mean}	Load ratio $R=P_{min}/P_{max}$	Max strain ($\mu\varepsilon$)	Stress range (MPa)
1	17.8	-17.8	0.0	-1.0	-	-
2	17.9	-17.9	0.0	-1.0	600	248
3	18.6	-18.6	0.0	-1.0	640	264
4	22.5	-22.5	0.0	-1.0	850	358
5	27.6	1.2	13.2	0.04	525(+518)	218
6	27.1	-0.3	13.7	-0.01	537(+535)	222
7	30.3	-0.9	15.6	-0.03	494(+513)	204

Note:

1) All the data were obtained from the initial test of each intact specimen.
2) The maximum strain for the specimen #1 was not recorded.
3) Strain values are those recorded from gauge s31.
4) Numbers inside the brackets are the strain values corresponding to P_{mean}.

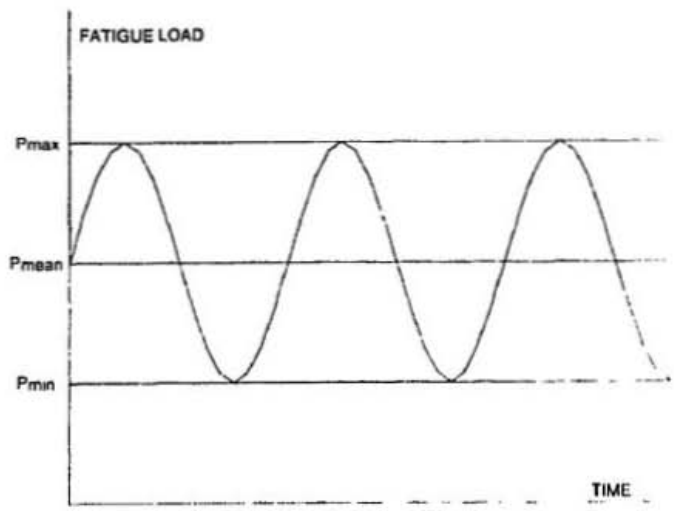

Figure 4.7 Cyclic sinusoidal fatigue load

4.2.2 Modal testing

Modal testing was done initially (before any fatigue load cycling was applied) and at each of the different predefined fatigue cycles, to record the dynamic response of the plated T-joint, from which the modal parameters would be extracted. Frequency response function method was used for modal testing; that is, frequency response function, which has been discussed earlier in Chapter 3, was obtained first. Modal parameters, such as natural frequencies, damping ratios, and mode shapes (or modal constant at a certain point and a certain mode) were then extracted from the corresponding FRFs. B&K 2034 Signal Analyzer (Brüel & Kjær, 1987) was used for data acquisition and FRF generation; and STAR STRUCT software (Spectral Dynamics, Inc., 1994) which was resident in a personal computer was used for the modal parameter extraction.

Excitation

Many different methods have been developed to obtain the frequency response function. These can be divided into transient and continuous excitation tests. The transient test is basically an impact test and is carried out using a modal hammer. A load cell is mounted at the head of a hammer. Each time the hammer strikes the specimen, the impact load is recorded at the same time as the response from a sensor (an accelerometer or a strain gauge) is recorded. From these responses, frequency response functions could be computed. The advantage of the transient test using a hammer is that the hammer can be very easily used to excite any location on the specimen and obtain the FRF at that location. With a number of sensors mounted at preselected

locations and directions (actually one is enough in many cases), and the hammer impacting a different location each time, one row of the frequency response function matrix **H** can be obtained. As discussed in Chapter 3, the response matrix **H** is a symmetric matrix, and one row or one column of the matrix **H** is sufficient to describe the system in terms of natural frequencies, damping ratios and mode shapes. Thus, the hammer test provides a quick and inexpensive method for determining frequency response functions. However, the hammer test has many disadvantages which limits its usefulness for performing tests which require high precision and accuracy. These include such items as lack of repeatability, excitation of few resonant frequencies, difficulty of maintaining an exact application point, requirement of many successive tests (averaging) to reduce noise, and low signal to noise ratio. Also for crack detection to have a better accuracy, the condition of each consecutive modal test has to be as close as possible, with the difference being only in the growing of the fatigue crack. Thus, the transient test using impact hammer is not suitable for crack detection.

On the other hand, the continuous excitation test can provide sufficient power into the system to excite as many frequencies as required. It has a good signal to noise ratio; since the exciter is fixed at a certain point, and it has good repeatability. Once a good forcing signal is used, and good response signals recorded, a high precision and accuracy of measurement and computation can be achieved. For the excitation forcing function, normally two types of signals are used: random and sine sweep signals (see Figure 4.8). The random signals include true random, pseudo random and periodic random signals [Figure 4.8(a)]. The big advantage of a random forcing function is that this type of signal covers a wide range of frequencies. This also

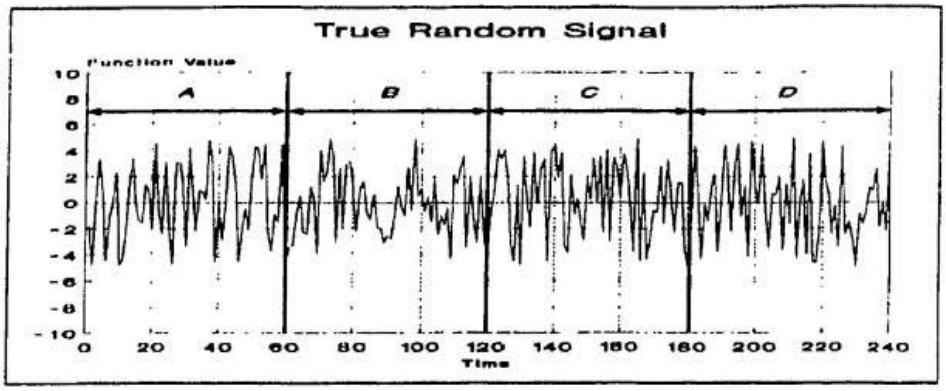

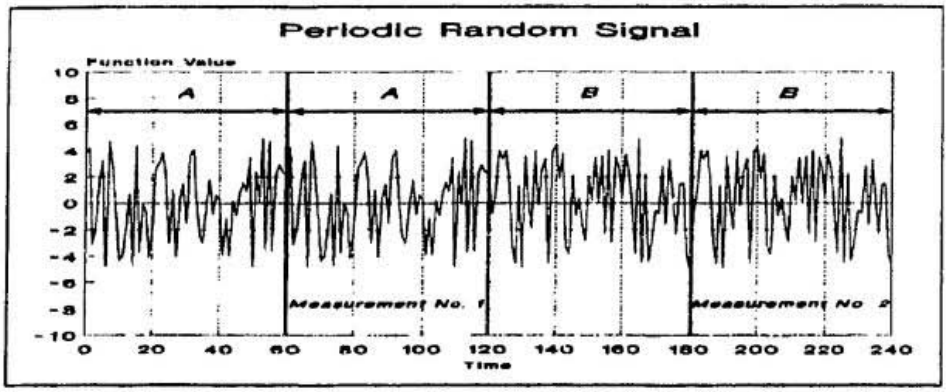

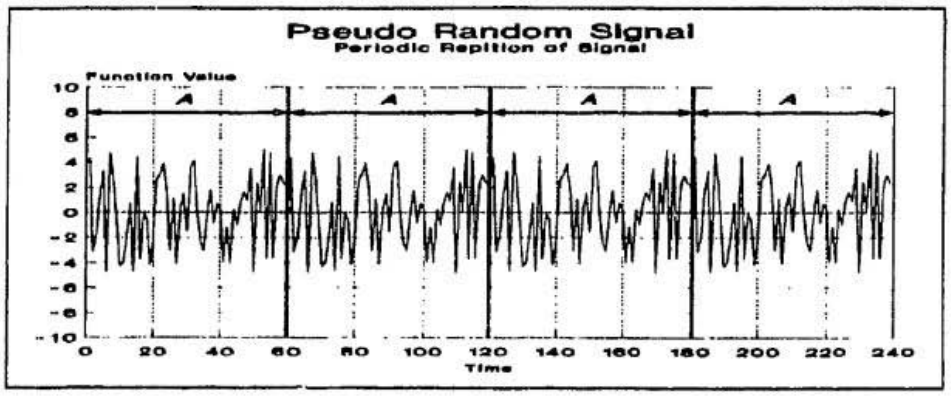

Figure 4.8(a) Samples of random signals

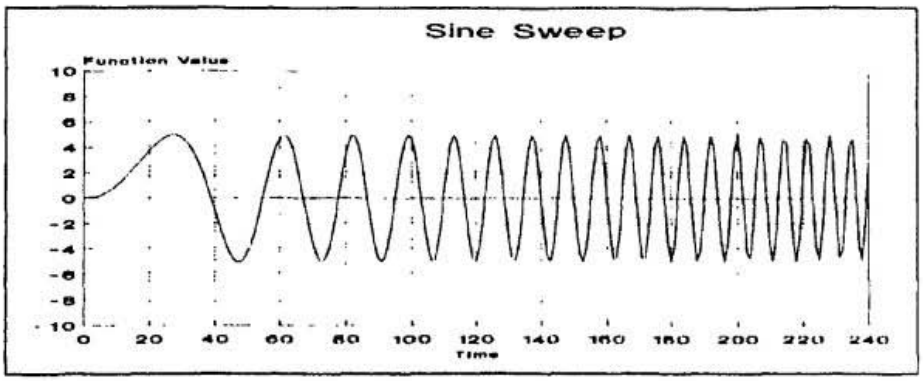

Figure 4.8(b) Samples of sine sweep signals

has a disadvantage, in that this type of excitation needs a large number of averaging to obtain a stable, smooth frequency response function.

The sine sweep function is a sinusoidal signal, with a constant amplitude, which continuously increases in frequency from a preset lower limit to a higher limit. The advantages of sine sweep excitation include: reduced noise (resulting in clean spectra), high signal to noise ratio, and minimized signal leakage. Few averages are required to achieve a smooth spectrum. It also has the advantage of being able to observe the response over a certain frequency band by zooming over a particular frequency range. The disadvantage of this type of excitation is that it does not represent the realistic service environment.

For crack detection, a repeatable and accurate measurement procedure is needed. Also, frequency response functions at a certain frequency range with high resolution are needed to examine the changes caused by fatigue cracking. Based on the discussion above, fixed point

excitation with sine sweep forcing signals was chosen for this study.

Response sensors

In order to have a good understanding of the modal behaviour of plated T-joints with a fatigue crack, a large number of sensors were used in this study. This was purely for the sake of detailed research investigation wherein mode shapes also could be obtained. For practical purpose, the number of sensors can be greatly reduced to only a few. Figure 4.9 shows the distribution of sensors (strain gauges and accelerometers) used in this experiment.

Along the weld-toe, where the crack was expected to occur, three strip gauges were used (s26-30, s31-35, and s36-40 in Figure 4.9). Each strip gauge had five individual gauges packed together. The total length of the strip gauge was 15 mm, with a 1 mm gap between each individual gauge, on either side. Two rosette gauges (s41-43 and s44-46 in Figure 4.9) were placed in between the strip gauges. The 45° rosette has a total length of 6.99 mm, with 3.18 mm length for each section. For the rest, general-purpose gauges with an overall length of 2.9 mm and a gauge length of 1.57 mm were used (s1 to s24, s25, s47 and s48).

STRUCTCEL light weight accelerometers (each accelerometer weighs 2.0 grams) were used to measure the accelerations. This type of accelerometers employ a mass loaded, differential structure as its sensing element with integral microelectronics. Encased in a plastic cap and a 3-pin transistor-header configuration, the accelerometer provides low cost, low mass

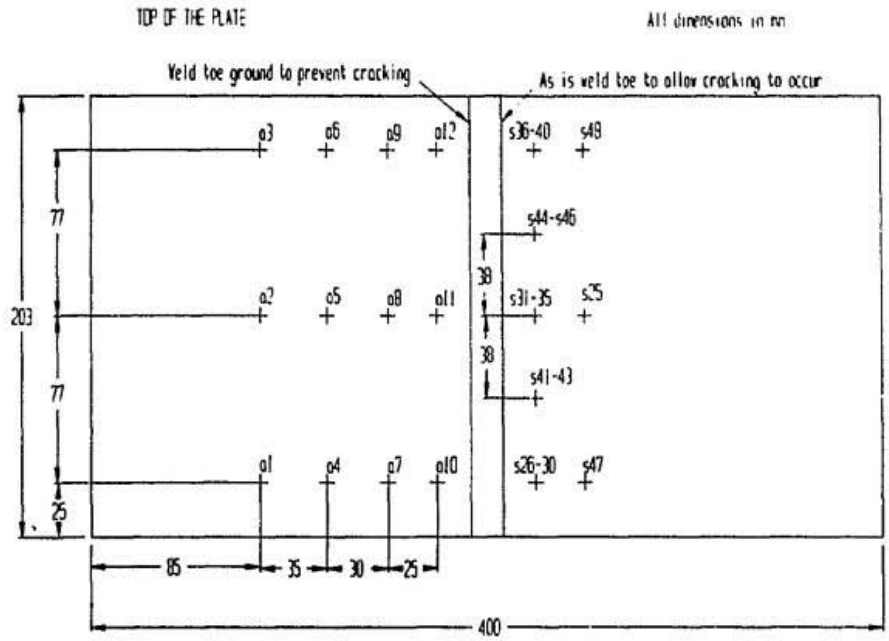

s26-30, s31-35, s36-40 are strip gauges; s41-43, s44-46 are rosette gauges; s25, s47 and s48 are single gauges

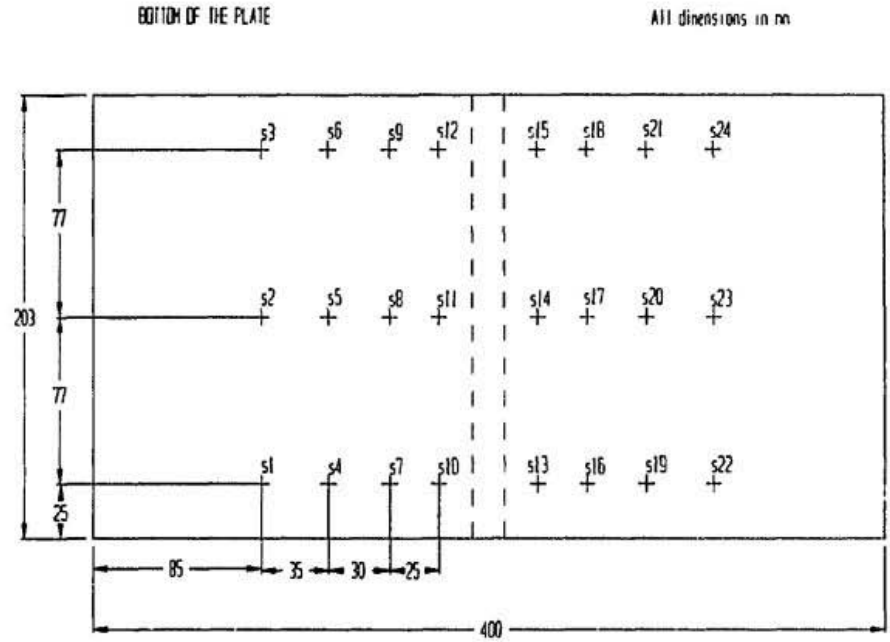

s1 - s24 are single strain gauges

Figure 4.9 Distribution of strain gauges and accelerometers

acceleration measurements. Some of the specifications of this type of accelerometers are listed in Table 4.3.

Table 4.3 Specifications of STRUCTCEL accelerometer

SPECIFICATION: STRUCTCEL ACCELEROMETER (Model No. 330A)	
Sensitivity (mV/g)	200
Range (±10V) (g)	10
Resolution (g)	0.001
Frequency range (±5% sens. dev.) (Hz)	1 - 1000
Resonant frequency (Hz)	3000
Excitation (±VDC)	15
Temperature range (°F)	0 - 130
Shock (max) (g)	5000
Weight (gm)	2
Connector (pin)	3

Strip gauges were placed very close to the weld toe in order to find the stress concentration around this area. Figure 4.10 shows the normalized modal strain obtained from the nearest gauge of a set of strip gauges located at the centre of the plate (s31 - s35) in specimen #3, for the first bottom plate bending mode, which is similar to the static bending of the bottom plate under an in-plane load on the plated T-joint. The nominal stress range at the weld toe for the plated T-joint is observed to be between 0.88 to 0.90 times the value of the maximum stress range given in Table 4.2 (it must be borne in mind that the gauge s31 is located at a distance of 1-3 mm from the weld toe and consequently that distance also must be taken into account while computing the nominal weld toe stress range).

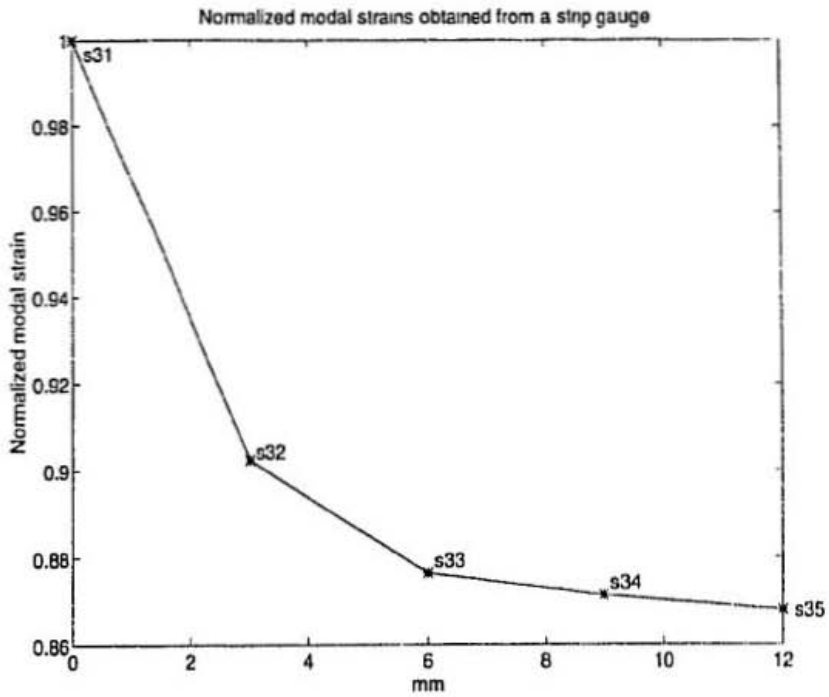

Figure 4.10 Normalized modal strains from a strip gauge

Signal processing

Figure 4.11 shows the diagram of the procedure for signal acquisition and subsequent data processing. Noise inevitably exists in most experimental setups. Therefore conditioners and filters are used to amplify the signal and reduce the noise level. Since the conditioners for the load cell and accelerometers have built-in filters, the signals received from them are relatively clear. For strain gauges, additional filters were used to eliminate any frequencies below and above the frequency range of interest. Shielded cables were used for all connections to shield out any interference from the laboratory's environment.

Aliasing and leakage errors were eliminated by choosing the right data acquisition frequency and record time length. Hanning window and signal averaging were used to further

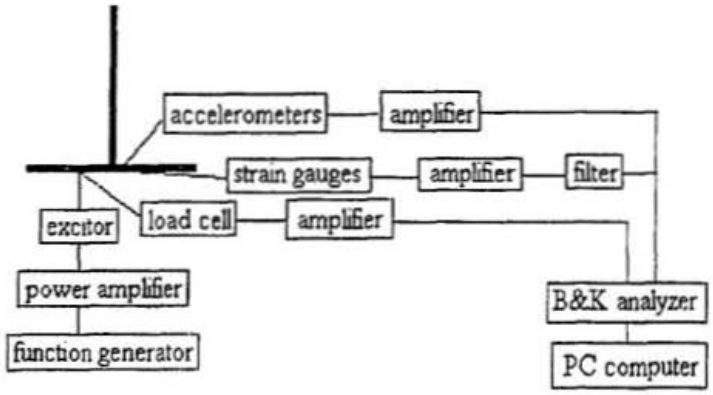

Figure 4.11 Procedure for data acquisition and signal processing

reduce the effect of noise. In order to have an efficient use of recorded data an overlap procedure, in which a block of time history data used for one analysis contained a certain amount of previously processed data, was used. Figure 4.12 shows a 50 % overlap procedure. This procedure is most useful when applying certain window techniques (e.g. Hanning window), since a portion of the data is reduced in amplitude by the window application. In this study a 75% overlap procedure with a Hanning window, available in the B&K analyzer, was used.

In the study, a sine sweep function was generated from a function generator and sent to the excitor. The excitation force was recorded through a load cell located in between the excitor and the plated T-joint. The force signal output from this type of connection had very small noise. Therefore, to obtain the frequency response function, the H_1 estimator, which reduces the noise in the response, was used. As described in Chapter 3, the H_1 is calculated from the cross spectrum of response and force, and the autospectrum of force. The formula of the H_1 estimator

can be expressed as:

$$H_1 = \frac{\sum F^* \cdot U}{\sum F^* \cdot F} = \frac{G_{FU}(\omega)}{G_{FF}(\omega)} \qquad (4.1)$$

where F is the forcing signal, U is the response signal, and * indicates the complex conjugate of the corresponding parameter.

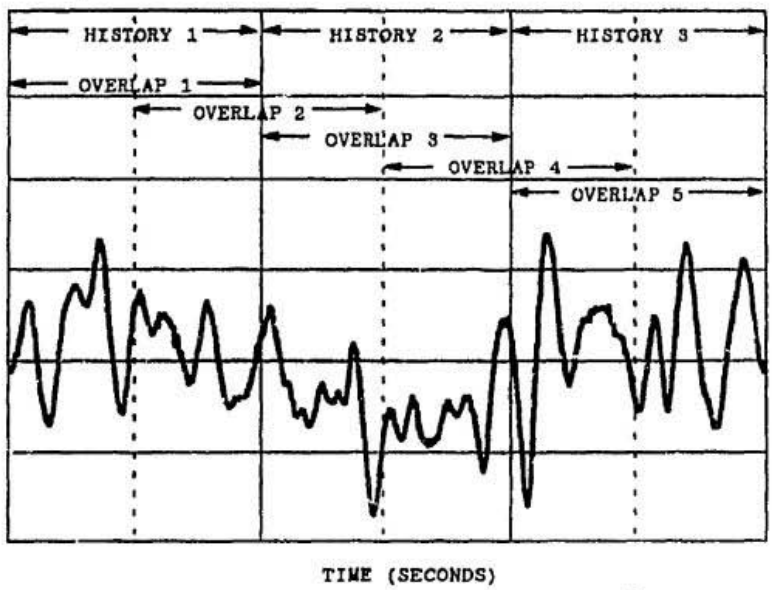

Figure 4.12 Overlap in signal processing

4.3 Results and Discussion

4.3.1 Natural frequencies and damping ratios

The first modal parameter to be examined is the natural frequency. It is not surprising to find out the small decrease of natural frequencies as the fatigue crack grew. Figures 4.13 (a) -

(f) show the changes in natural frequencies and damping ratios as the fatigue crack grew, for each of the seven specimens tested. Table 4.4 gives the fatigue cycles for each fatigue interval, for each of seven specimens tested. See Apperdix II for all the frequencies and damping values for all seven specimens at all predefined fatigue cycles. It is observed that the crack produces noticeable changes only towards the end of its life. Most of the changes in modal parameters such as natural frequencies, amplitude of strain frequency response functions, etc. occurred only after the ink staining was done. Also it should be noted that at the fatigue cracking interval wherein ink staining was done, modal strain values around the crack area dropped significantly, while changes in natural frequencies were barely noticeable.

It should also be noted that the fourth resonant frequency is missing from Figures 4.13(a-f). From the finite element analysis which will be discussed in the next chapter, the fourth resonant frequency was observed to be a torsional mode of the top plate, while the bottom plate barely moved (see Figure 5.3). Therefore, sensors located at the bottom plate were not able to pick up this resonant frequency.

From these figures, it can be seen that the changes in natural frequencies were very small; only towards the end of fatigue life, during which time the plate was almost broken (the crack was throughout the width and the depth of crack was more than half the plate thickness), the natural frequencies showed some large, reliably detectable changes. The patterns for changes of damping ratios as the fatigue crack grew, were not well defined.

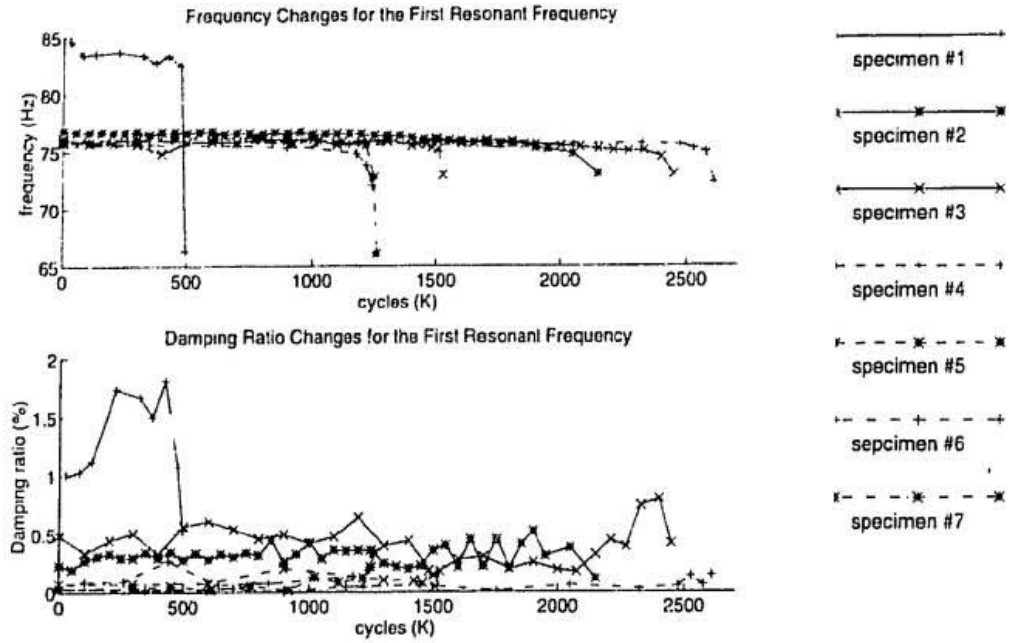

Figure 4.13(a) Changes in frequency and damping ratio for first resonant frequency

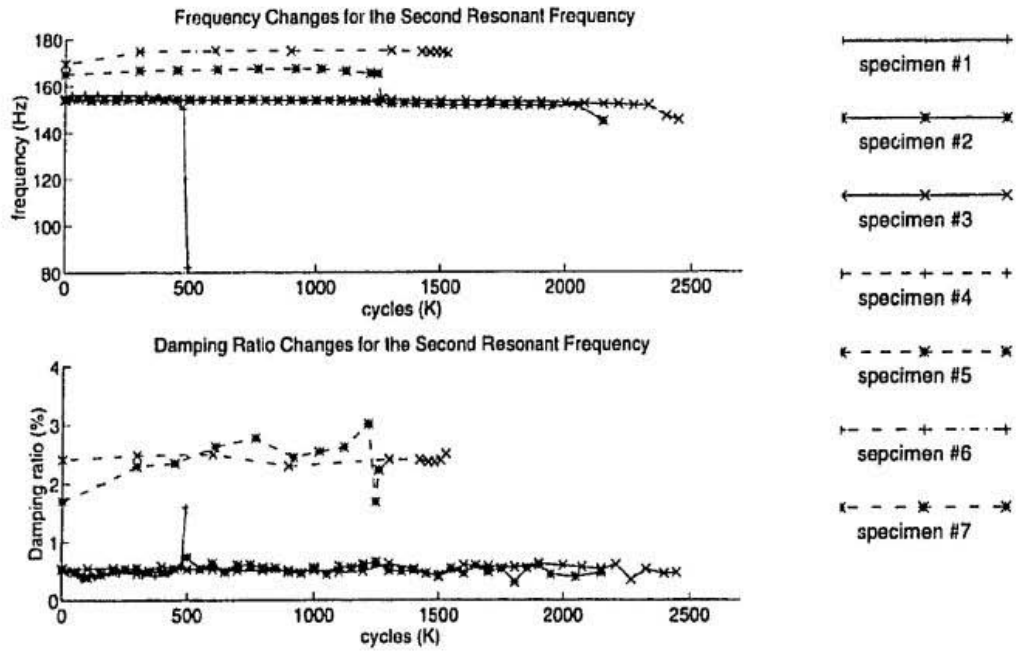

Figure 4.13(b) Changes in frequency and damping ratio for second resonant frequency

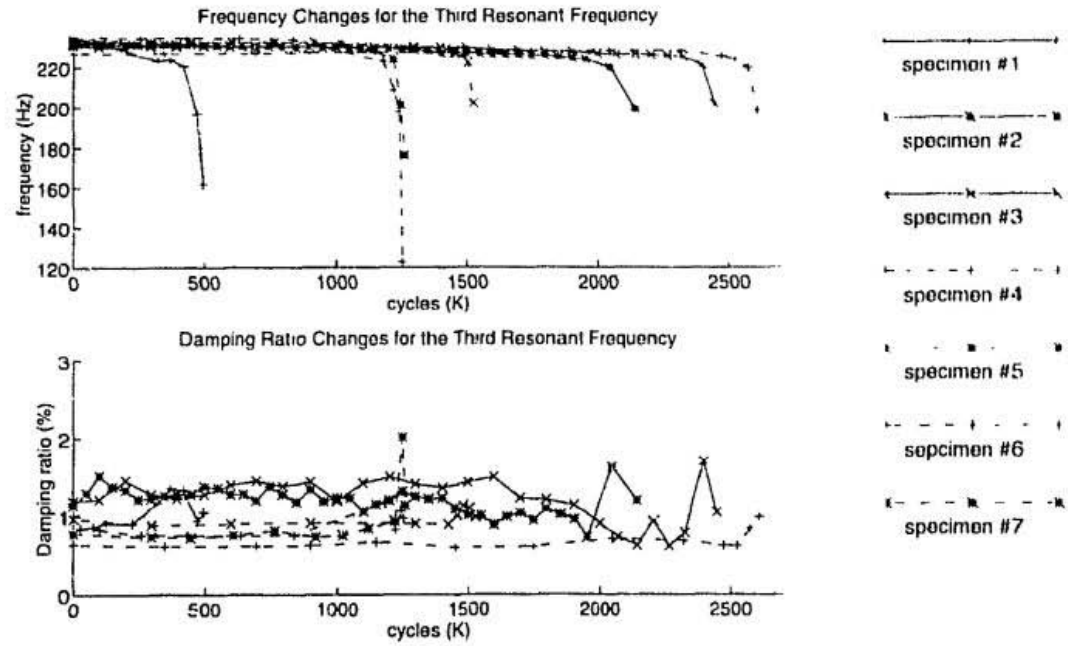

Figure 4.13(c) Changes in frequency and damping ratio for third resonant frequency

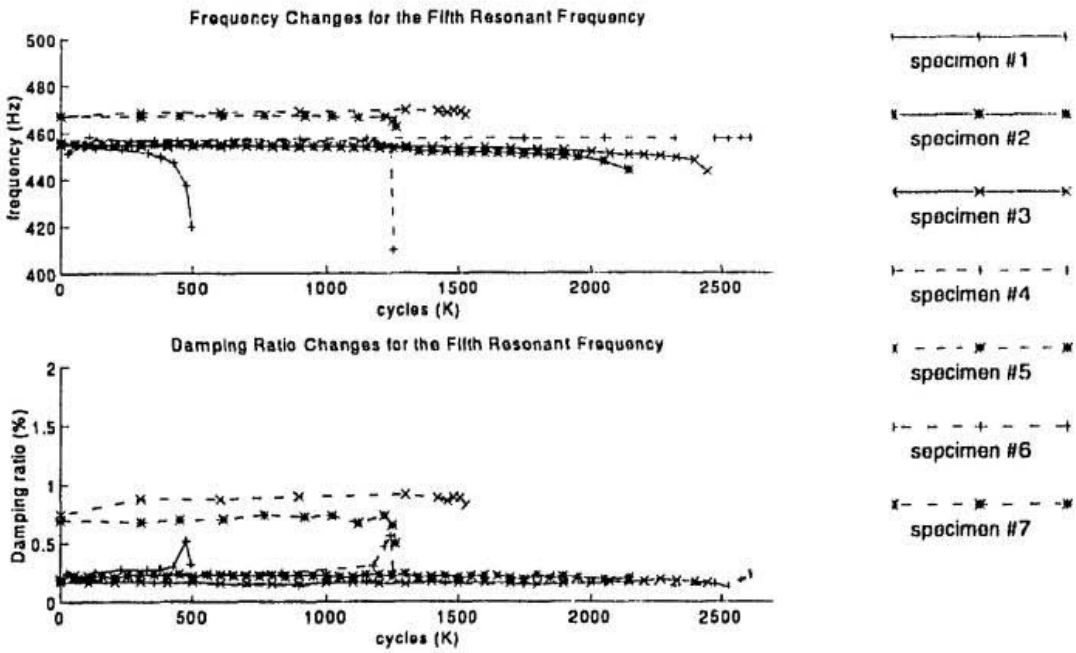

Figure 4.13(d) Changes in frequency and damping ratio for fifth resonant frequency

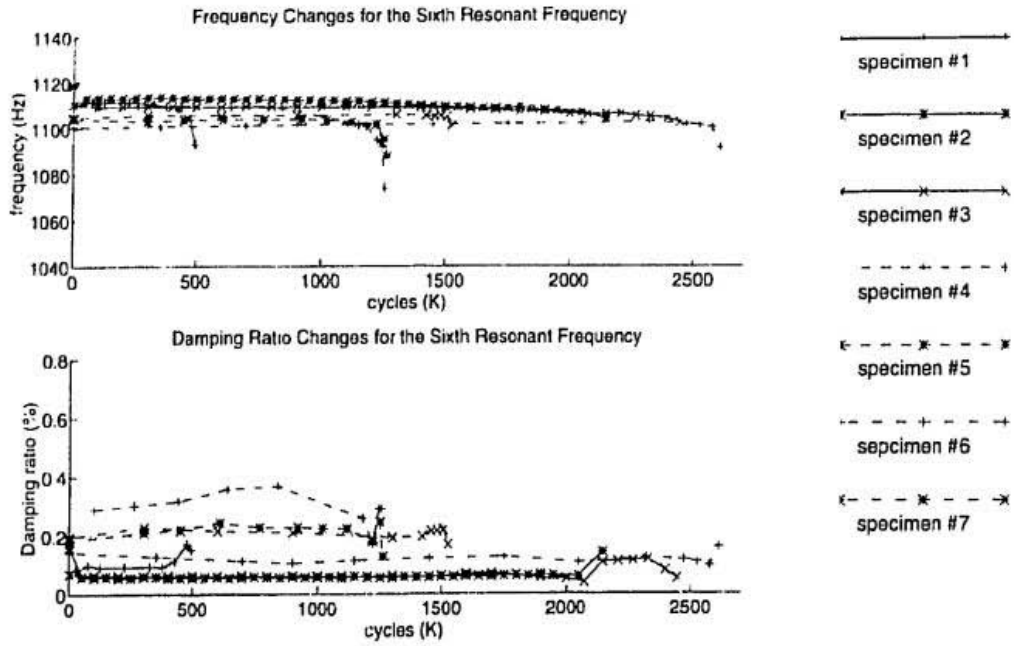

Figure 4.13(e) Changes in frequency and damping ratio for sixth resonant frequency

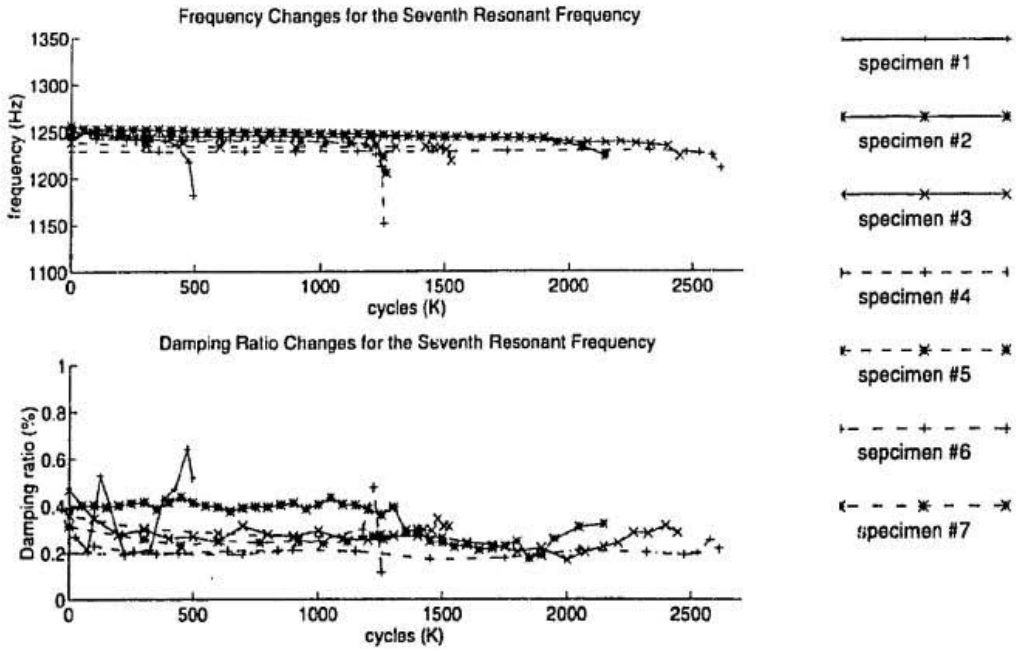

Figure 4.13(f) Changes in frequency and damping ratio for seventh resonant frequency

4.3.2 Frequency response functions for accelerations

Twelve accelerometers were used on each specimen to record acceleration responses at 12 points. Figure 4.14 shows the changes in acceleration frequency response functions of two points, one of which was located close to the weld toe, and the other close to the supporting edge. The results of FRF for specimen #7 is given below; and all other specimens show a similar pattern and due to the space limitation, they are not shown in here.

It can be seen from Figures 4.14(a) and (b), that the changes in acceleration FRFs are small, both near and far away from the crack; the acceleration FRFs change a little bit more in locations further from the crack than near the crack. The last fatigue interval represented in Figure 4.14 is interval 6, of specimen #7, which represents a crack length of 114.0 mm, and depth of 7.5 mm (specimen width is 203 mm and thickness 16 mm). This size of crack should be considered as quite significant for the structure, and should be detected to prevent failure of the structure. Obviously from acceleration FRFs alone, it would be very difficult to detect the crack since the changes are very small.

4.3.3 Frequency response functions of surface strains.

In order to find more sensitive parameters for fatigue crack detection, strain gauges were used, and were applied all over the base plate of the plated T-joint at 32 points. Figure 4.15 shows the strain FRFs at a point away from the crack while Figure 4.16 shows the FRFs at a

Table 4.4 Fatigue cycles for each crack growth interval of the seven plated T-joint specimens

Specimen #1		Specimen #2		Specimen #3		Specimen #4		Specimen #5		Specimen #6		Specimen #7	
Fatigue interval	Growth cycles (k)	Fatigue interval	Growth cycles (k)	Fatigue interval	Growth cycles (k)	Fatigue interval	Growth cycles (k)	Fatigue interval	Growth cycles (k)	Fatigue interval	Growth cycles (k)	Fatigue interval	Growth cycles (k)
1	25	1	50	1	100	0	100	0	300	0	350	0	300
2	75	2	100	2	200	1	260	1	450	1	700	1	600
3	125	3	150	3	300	2	440	2	610	2	900	2	900
4	225	4	200	4	400	3	640	3	770	3	1,150	3	1,300
5	325	5	250	5	500	4	840	4	920	4	1,450	4*	1,422
6	375	6	300	6	600	5*	1,180	5*	1,020	5	1,750	5	1,457
7	425	7	350	7	700	6	1,222	6	1,120	6	2,050	6	1,482
8	475	8	400	8	800	7	1,243	7	1,220	7*	2,325	7	1,507
9	495	9	450	9	900	8	1,253	8	1,249	8	2,475	8	1,527
failure	497	10	500	10	1,000	failure	1,332	9	1,261	9	2,525	failure	1,533
		11	550	11	1,100			failure	1,265	10	2,575		
		12	600	12	1,200					11	2,610		
		13	650	13	1,300					failure	2,611		
		14	700	14	1,400								
		15	750	15	1,500								
		16	800	16	1,600								
		17	850	17*	1,700								
		18	900	18	1,800								
		19	950	19	1,900								
		20	1,000	20	2,000								
		21	1,050	21	2,075								
		22	1,100	22	2,150								
		23	1,150	23	2,210								
		24	1,200	24	2,270								
		25	1,250	25	2,330								
		26	1,300	26	2,400								
		27	1,350	27	2,448								
		28	1,400	failure	2,467								
		29	1,450										
		30	1,500										
		31	1,550										
		32*	1,600										
		33	1,650										
		34	1,700										
		35	1,750										
		36	1,800										
		37	1,850										
		38	1,900										
		39	1,950										
		40	2,050										
		41	2,150										
		failure	2,198										

* Initial cracking was observed and ink staining was carried out at this interval.

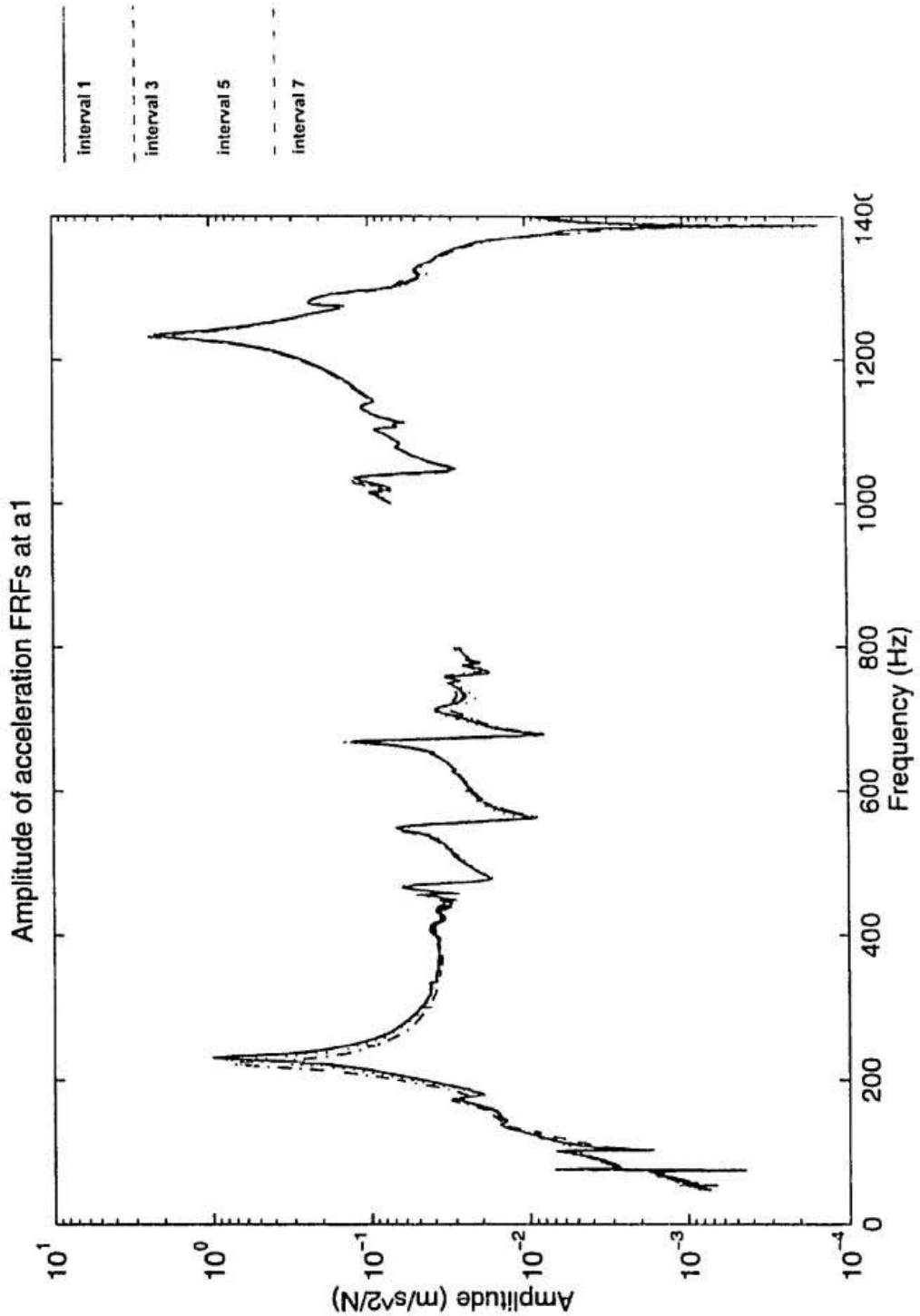

Figure 4.14(a) Acceleration FRFs at a1 for various crack growth intervals; close to the supporting edge (specimen #7)

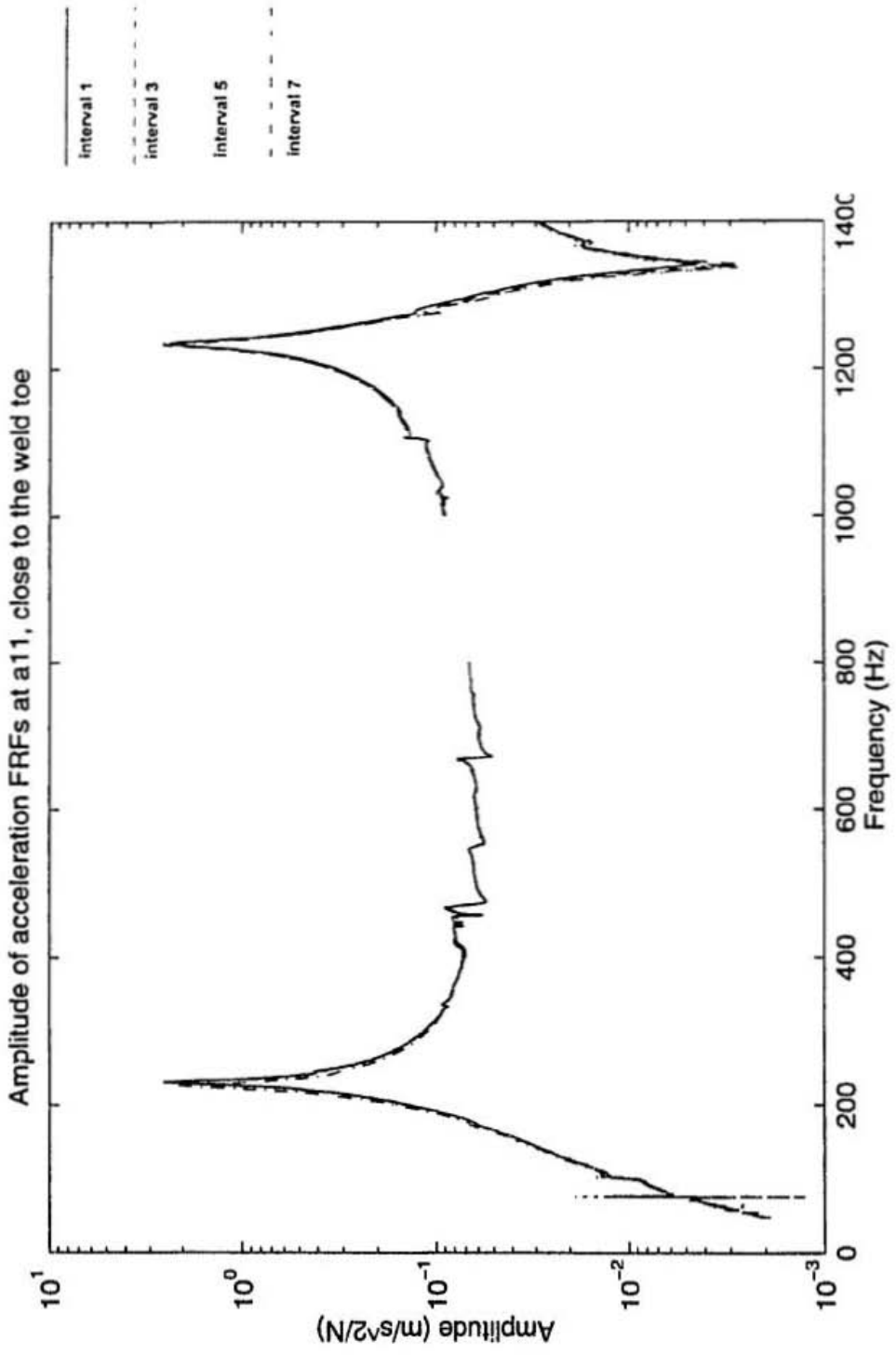

Figure 4.14(b) Acceleration FRFs at a11 for various crack growth intervals; close to the weld toe (specimen #7)

region close to the crack: Figure 4.17 shows the FRFs at a point between the above two points. It is observed that strain gauges have a much greater sensitivity to cracks than accelerometers at locations near to the crack: at locations far away from the crack, the accelerometers and strain gauges have almost the same sensitivity. One problem with the strain gauges is that the data is noisy at strain levels below 10^{-2} micro-strain/N. Also it could be seen from the strain gauge data, that in spite of its noise levels, the trend in amplitude decrease is the same as in non-noisy regions, if not better.

Rosette gauges are also used to measure the response of the structure to the dynamic excitation. Figure 4.18 shows the FRFs at different crack levels for a rosette gauge located at node s41-43 (see Figure 4.9), with one gauge at 45°, second at 90° and the third at 135°.

From Figures 4.15 - 4.18, it is seen that strain FRFs undergo significant changes at regions close to the crack. This close-to-the-crack region can be defined as a circle, with a diameter slightly larger than the surface crack length. This definition of close-to-the-crack region should have a practical meaning, since in real structures, it is always possible to find out the critical regions, where high stress values would exist (obtained by finite element analysis). Thus a small number of strain gauges can be placed at these critical regions. If significant changes in FRFs were observed in one of these regions located at various critical locations in the structure, it indicates that some damage might have occurred in that region. More detailed investigation, such as the model updating procedure discussed in next chapter, should be used to determine the extent of damage.

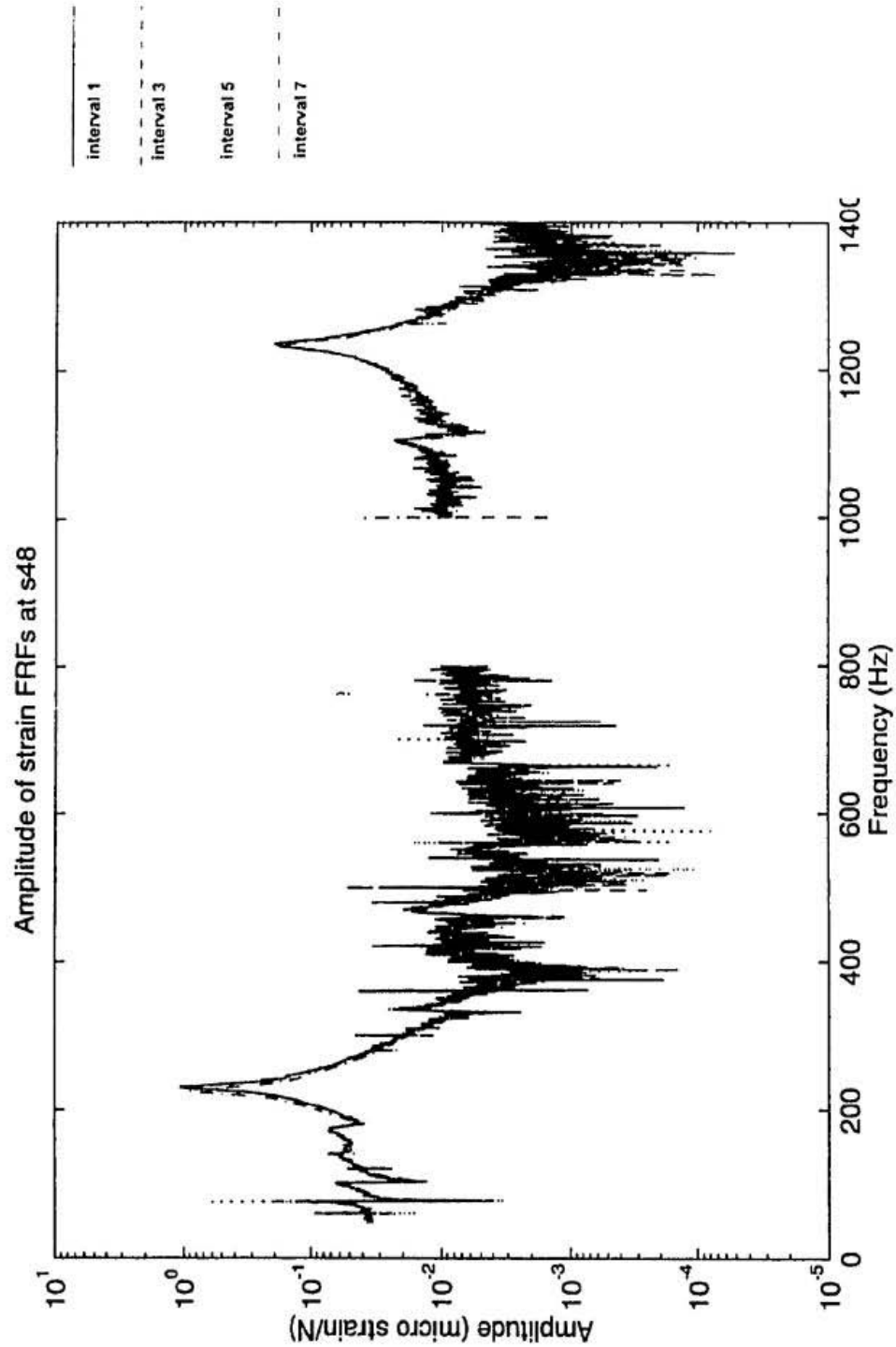

Figure 4.15 Strain FRFs at s48 (single gauge) for various crack growth intervals; s48 is located away from the crack (42 mm) (specimen #7)

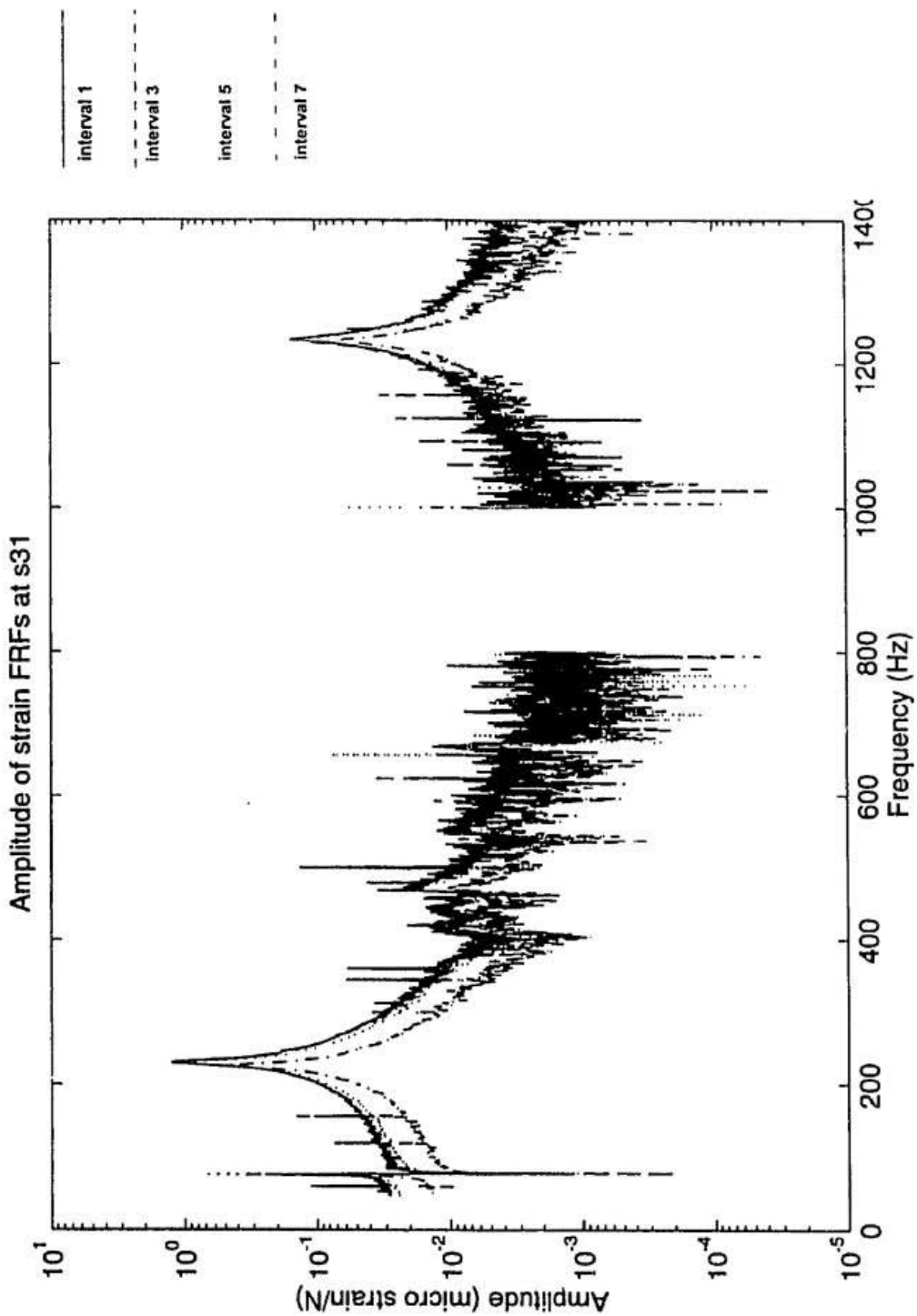

Figure 4.16 Strain FRFs at s31 (strip gauge) for various crack growth intervals; s31 was located very close to the crack at the centre of the bottom plate (1-3 mm) (specimen #7)

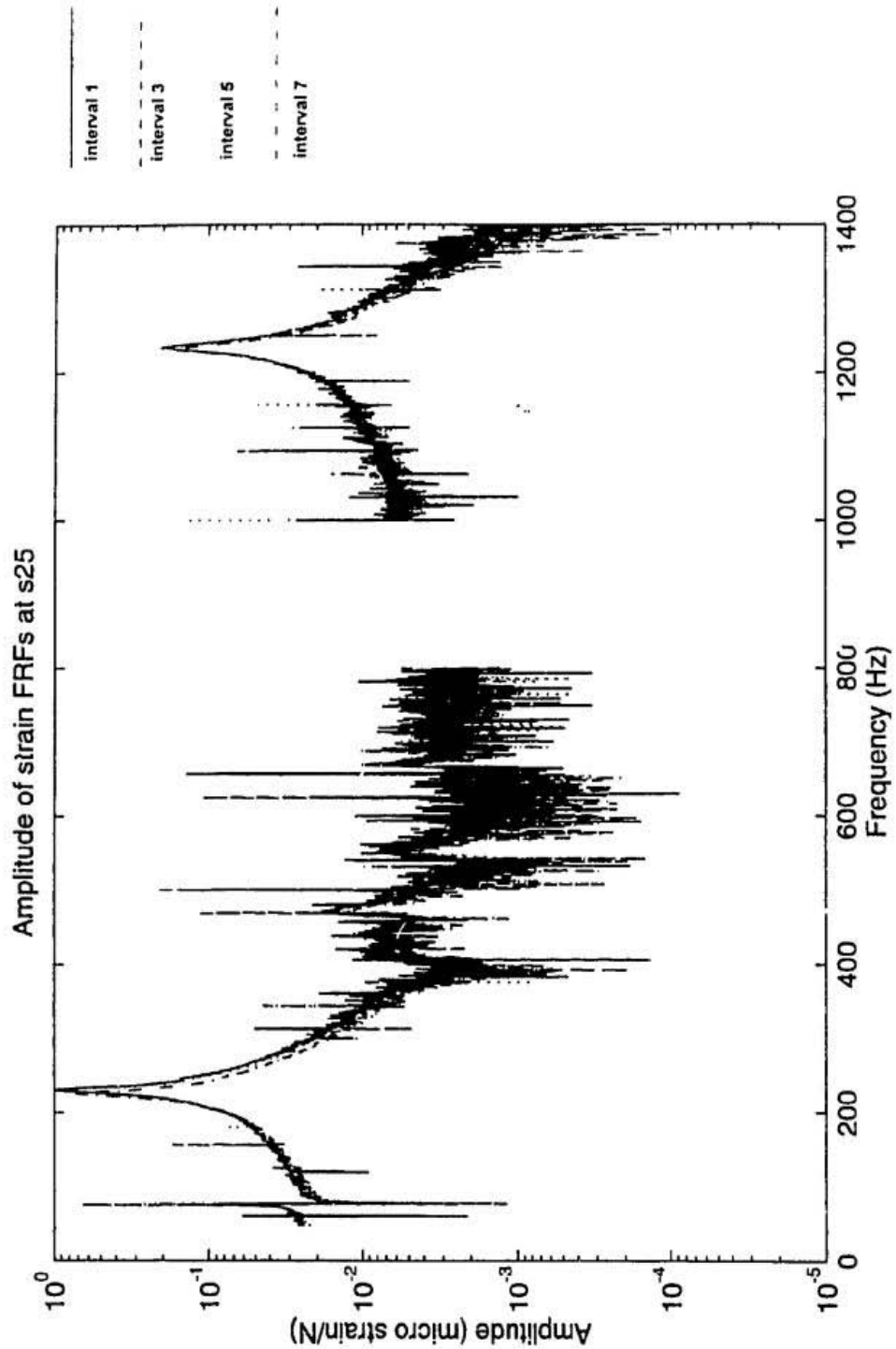

Figure 4.17 Strain FRFs at s25 (single gauge) for various crack growth intervals; s25 was located away from the crack at the centre of the bottom plate (42mm) (specimen #7)

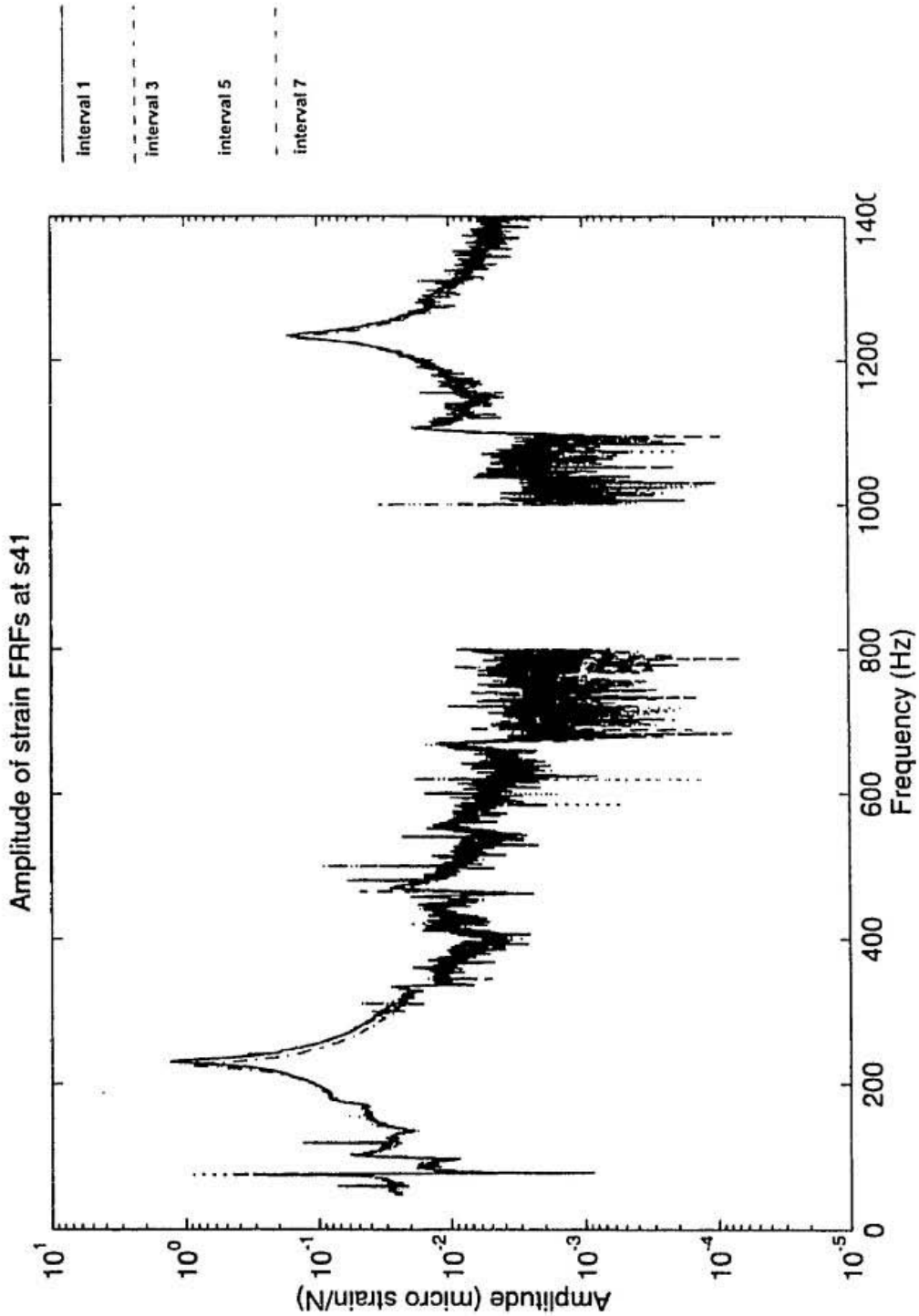

Figure 4.18(a) Strain FRFs at s41 (rosette gauge) for various crack growth intervals; s41 was located close to the crack at 45° to the crack (5-8 mm) (specimen #7)

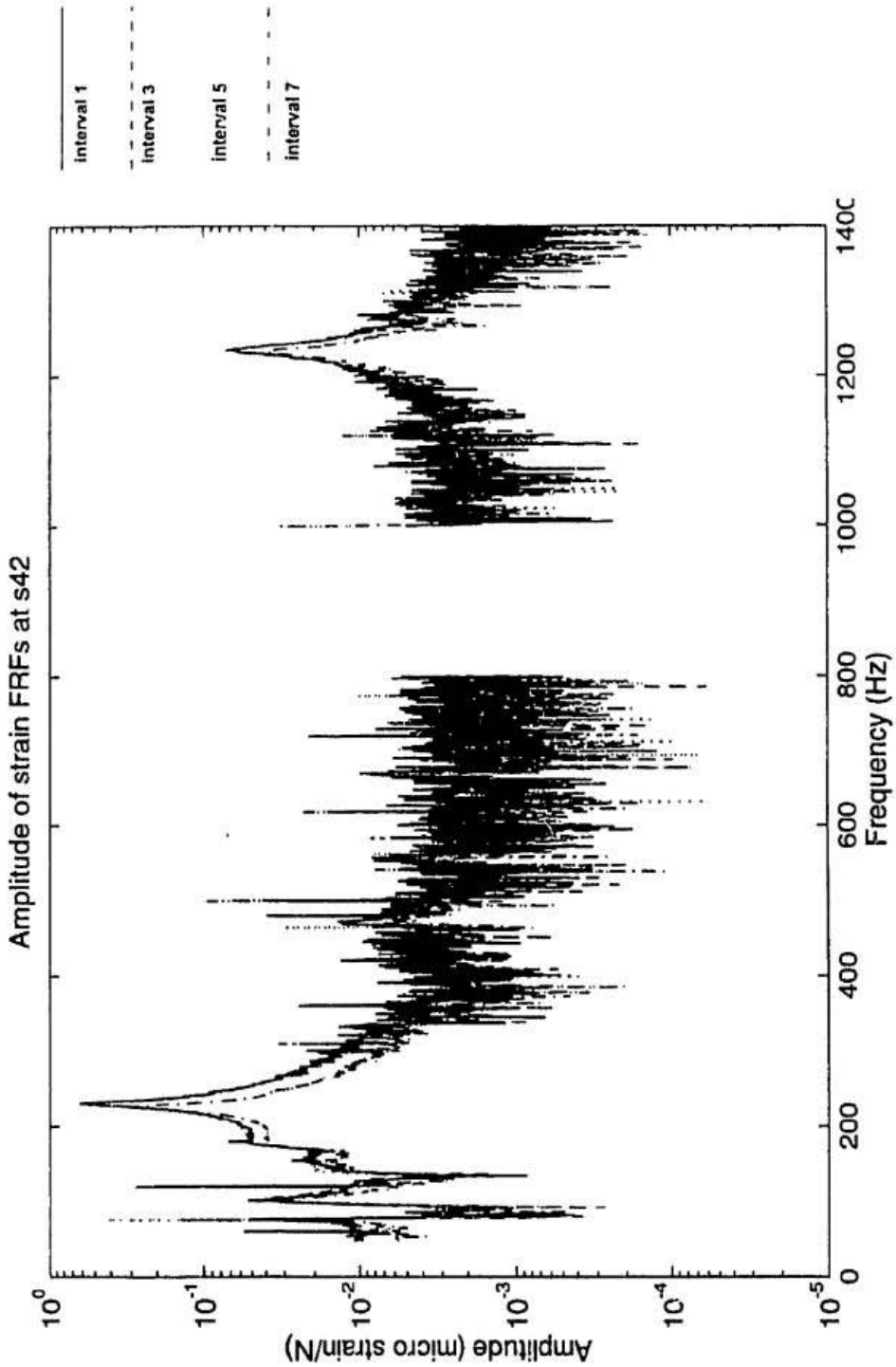

Figure 4.18(b) Strain FRFs at s42 (rosette gauge) for various crack growth intervals; s42 was located close to the crack at 90° to the crack (5-8 mm) (specimen #7)

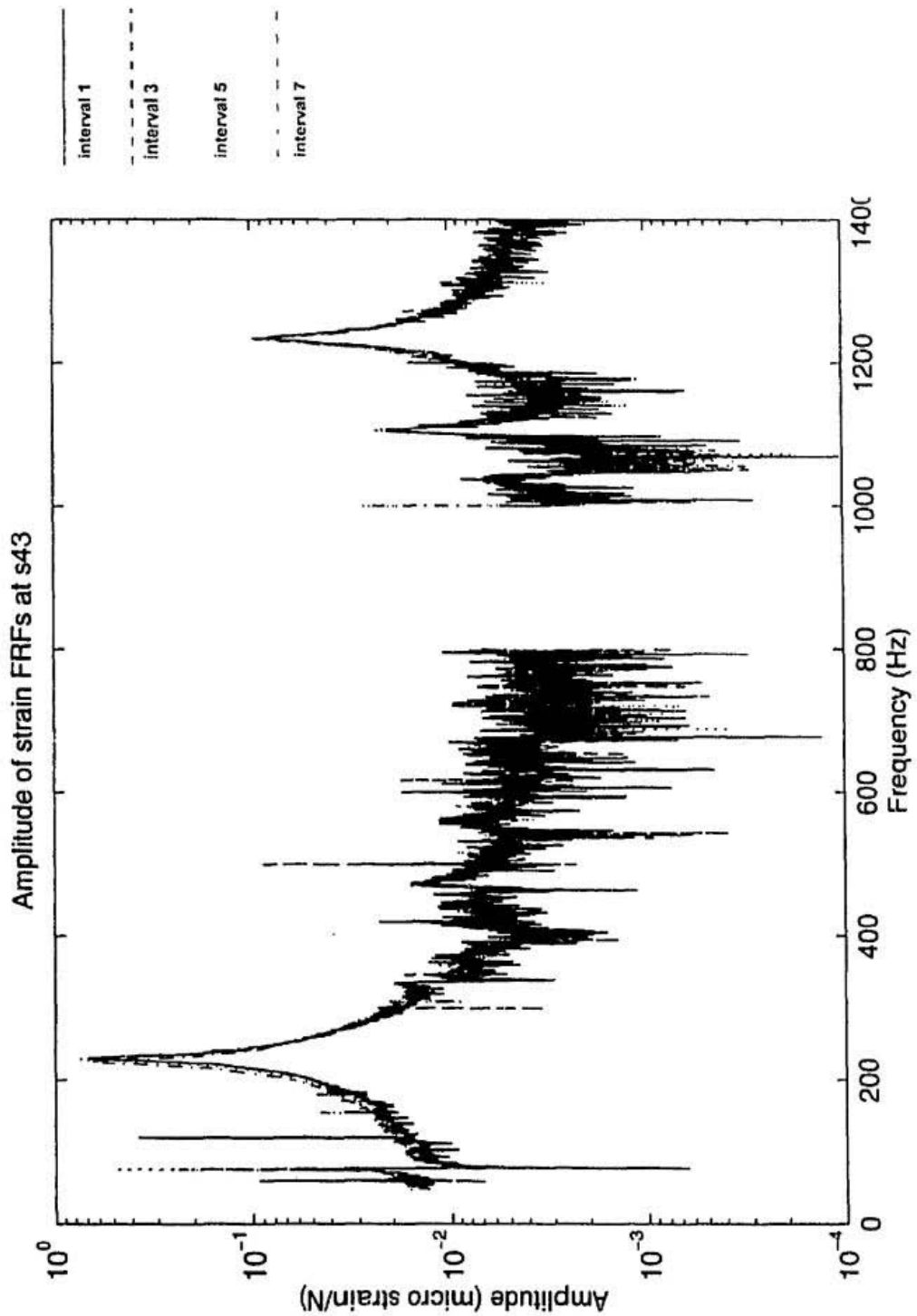

Figure 4.18(c) Strain FRFs at s43 (rosette gauge) for various crack growth intervals; s43 was located close to the crack at 135° to the crack (5-8 mm) (specimen #7)

4.3.4 Mode shapes

Displacement mode shapes were obtained from accelerometers located on the left half of the bottom plate. Figure 4.19 shows six displacement mode shapes of left half portion of the bottom plate. The other half of plate, which had no accelerometers on it, was also plotted for comparison purposes. The mode shapes showed in Figure 4.15 (and the following figures) was obtained from specimen #3. From these mode shapes, it was observed that the first mode was a bending mode, the second a torsional mode, the third a bending mode, the fifth a bending mode (again the fourth mode was missing from the experimental data due to the location of the sensors, as explained early), the sixth a torsional mode and the seventh a bending mode. The experimental results match very well with the results obtained from the finite element analysis which will be discussed in the next chapter. It can be seen here that the major purpose of displacement mode shapes in this study, is to classify the experimental results and separate the bending modes from torsional modes.

Strain mode shapes are obtained from the strain gauges located on the bottom plate of the T-joint. As stated earlier, the changes in the strain mode shapes were used for the initial identification of fatigue crack occurring in the structure. Figure 4.20 shows the strain mode shapes of the intact plated T-joint; Figure 4.21 shows the strain mode shapes of the cracked plated T-joint (from specimen #3). Figure 4.22 shows the crack profile of that specimen. At the fatigue cracking interval where the above mode shapes were obtained, the surface crack length was 36.0 mm and the crack depth was 7.5 mm, with the deepest point being almost

mode 1

mode 2

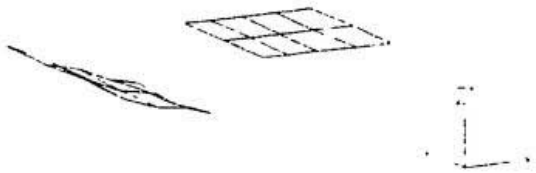

mode 3

mode 5

mode 6

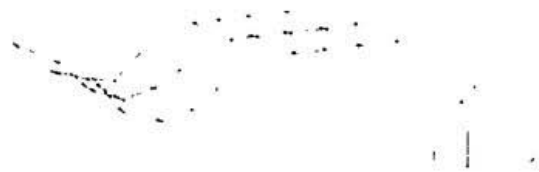

mode 7

Figure 4.19 Displacement mode shapes

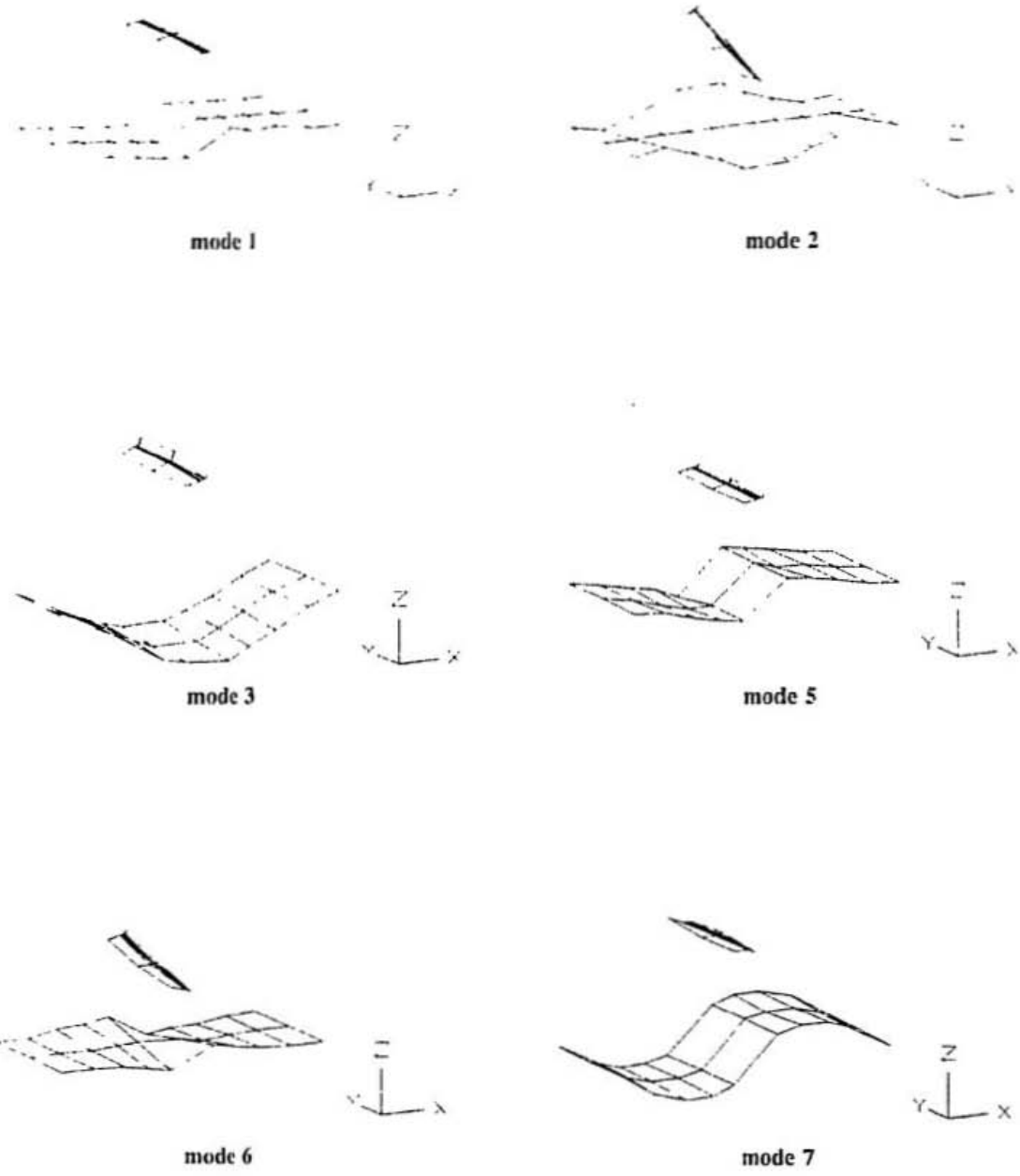

Figure 4.20 Strain mode shapes for the intact T-joint

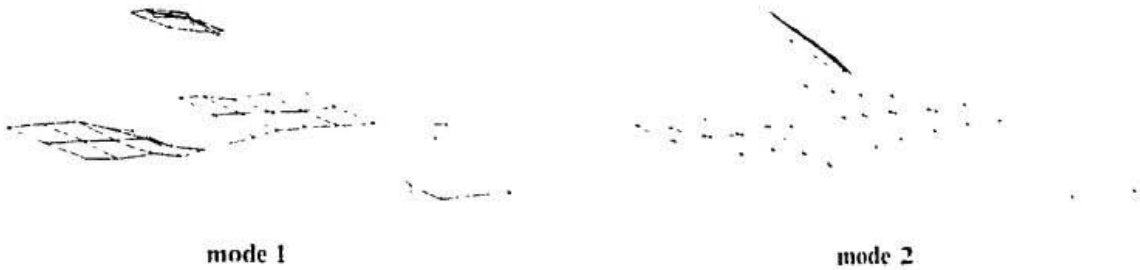

mode 1

mode 2

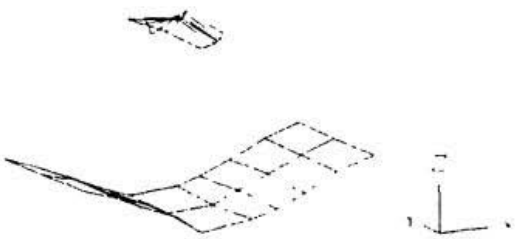

mode 3

mode 5

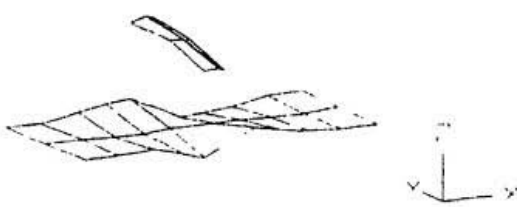

mode 6

mode 7

Figure 4.21 Strain mode shapes for the cracked T-joint

Figure 4.22 Crack profile for specimen #3

towards one edge of the plate (the dark area in Figure 4.22). It can be seen from Figure 4.21 that at top of the plate, near the weld-toe, the modal strain on one side has a very large drop. This drop is especially clear in the third mode, since this is the dominant mode around this area (from frequency response functions). All other specimens show a similar pattern, with a difference that the largest drop in modal strain occurs either near the edge of the plate, or at the centre of the plate, depending on where the crack has initiated. Based on this observation, the initial crack detection can be made; more detailed analysis is carried out in the next chapter.

4.4 Summary

In this chapter, the procedure used for the experimental study and the instrumentation used for the purpose were described. Seven plated T-joints were tested under fatigue loading, modal tests were carried out for each of seven specimens at each of the predefined fatigue cycle levels. Modal parameters such as natural frequencies, strain FRFs and acceleration FRFs were examined as the fatigue crack grew in depth and surface length. It was found that the changes

in natural frequencies, as a fatigue crack grew, were very small; whereas the changes in modal strains near the crack area were very significant. From these changes obtained through examination of the changes in strain mode shapes, an initial crack detection which predicted the approximate cracking area was made. Strain/acceleration frequency response functions were recorded at each of the predefined fatigue cycle levels and these are to be used in further analyses, which will be carried out in the next chapter.

CHAPTER 5

FINITE ELEMENT ANALYSIS OF PLATED T-JOINTS AND MODEL UPDATING FOR CRACK DETECTION

5.1 FE Model

A FE model was generated for the plated T-joints using shell elements available in the general purpose computer program ABAQUS (Hibbitt, Karlsson & Sorenson Inc., 1995). Line spring elements were used to model the surface crack on the plate. The S8R5 element, which is an 8-node doubly curved thin shell element with reduced integration and having five degrees of freedom per node, was used for most of the parts of T-joint; the S4R5 element, which is a 4-node doubly curved thin shell element with reduced integration and having five degrees of freedom per node with hourglass control, was used around the line spring elements. The reason for using the S4R5 element with the line spring element is for hourglass control. Since line spring elements assume plane strain conditions, the linear interpolation used for 4-noded shell elements provide a much better solution to this condition. It was found that the use of the 8-

noded S8R5 element around the line spring elements, displayed hourglass phenomena for some higher modes. Hence, 4-noded S4R5 elements were used to connect the line spring elements with the S8R5 elements. Some triangular thin shell elements, STRI56, were used for proper transition between the finite element meshes. Figure 5.1 shows the FE model of the plated T-joint. Figure 5.2 shows the expanded view of anticipated crack region, with a very fine mesh around the line spring elements. The weld thickness was modelled by increasing the thickness of the shell elements associated with the weld toe region. Table 5.1 shows the natural frequencies obtained from this intact FE model.

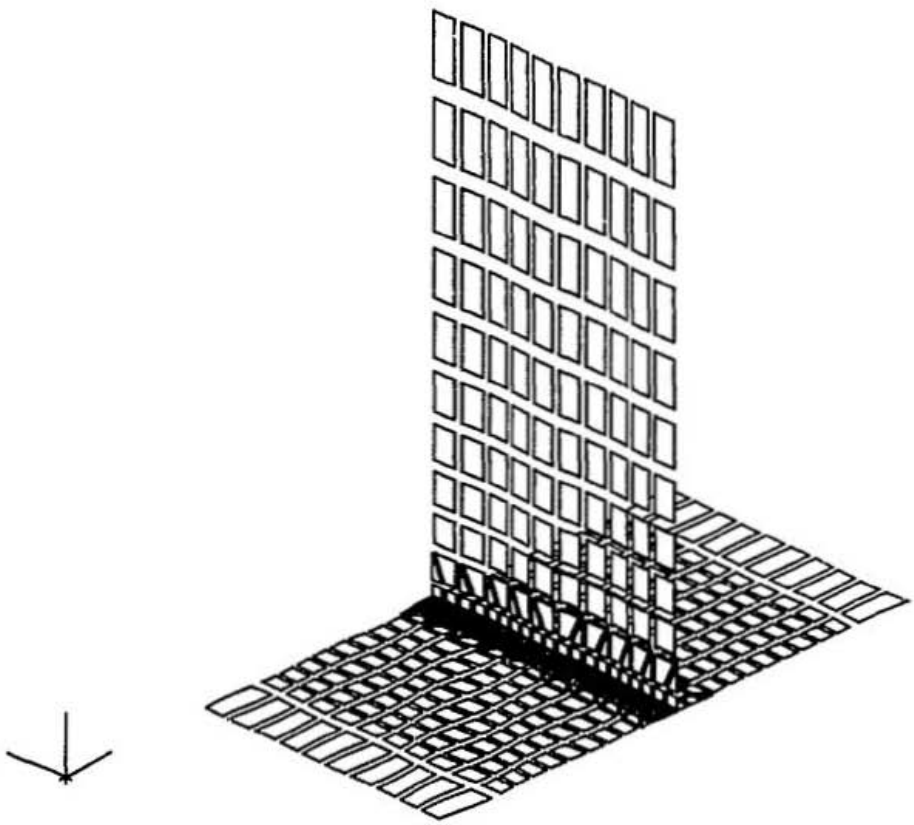

Figure 5.1 FE model of the plated T-joint

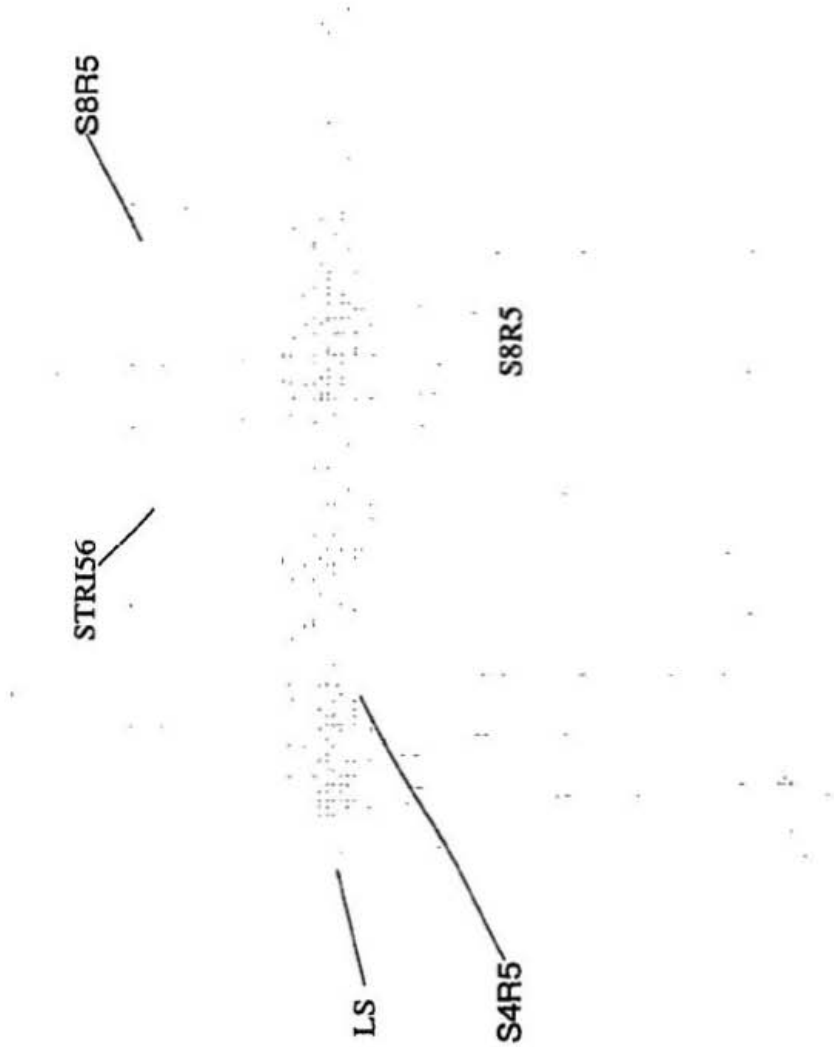

LS - 6 noded line spring element; S4R5 - 4 noded thin shell element; S8R5 - 8 noded thin shell element; STRI56 - 6 noded triangular thin shell element

Figure 5.2 Fine mesh around the anticipated crack region

Table 5.1 Natural frequencies obtained from the FE model (uncracked) [experimental frequencies (from specimen #3) within bracket]

Mode	1	2	3	4	5	6	7
Freq. (Hz)	75.295 (75.73)	137.67 (153.78)	220.05 (230.44)	336.82 -	470.80 (454.21)	1088.7 (1109.63)	1291.1 (1246.36)
Error (%)	0.6	10.5	4.5	-	-3.7	1.9	-3.6

Mode shapes from this FE model were also obtained and are shown in Figure 5.3. It can be found from Figure 5.3 that the first mode is a bending mode (top plate bending dominant); the second mode is a bending mode for the top plate in the in-plane direction (for the bottom plate, the same mode becomes to a torsional mode); the third mode is a bending mode with dominant bottom plate bending; the fourth mode is a torsional mode of the top plate (bottom plate shows very small deformation); the fifth mode is a bending mode of both top and bottom plates; the sixth mode is a torsional mode with top plate torsion being dominant; and the seventh mode is another bending mode for both top and bottom plates. All these modes agree with the results from experiments (shown in Figure 4.15), except mode 4. The reason for which the fourth mode was not identified from experimental data is that the deformations at the bottom plate are very small. Since all sensors are located on the bottom plate, this resonant mode is not picked up.

Also it is noticed from Table 5.1, that the natural frequencies obtained from this initial FE model do not match closely with the experimental results. There are several reasons that could have generated these differences: (i) Boundary conditions in the experimental set up were

not modeled properly in this initial FE model; (ii) Thickness variations in the weld toe area were not modeled properly in the initial FE model; (iii) Variations that occur in the Young's modulus values as shown in Table 4.1 (for the initial FE model, it was set to be 210 GPa); and (iv) Small variations in the thickness that occur throughout the T-joint; in the initial FE model, the thickness was taken to be 16 mm everywhere. Although the errors shown in Table 5.1 are not very large for most of the modes, for crack detection using model updating procedure, a more accurate FE model must be generated. Also some variations in thickness, Young's modulus and boundary conditions occur for each specimen tested; hence a refined FE model, discussed in the next section, is introduced for each specimen of the plated T-joint.

5.2 Refining of FE Model to be Compatible with Experimental Results

It is seen from Table 5.1 that the results obtained from the FE model will be usually different from that of the experimental model due to the discretion used in FE model. In order to make these two sets of results compatible, the FE model is normally refined to match the experimental results. It is assumed that the experimental model represents the "true" model of the structure. Although this may not be true always, it can be assumed to be true for most of the cases. In a FE model, some simplifications are always inherent in order to generate a workable model. There is also a limitation for the size and the number of elements one can use in a FE model. Thus, there is usually some scope for refining the FE model.

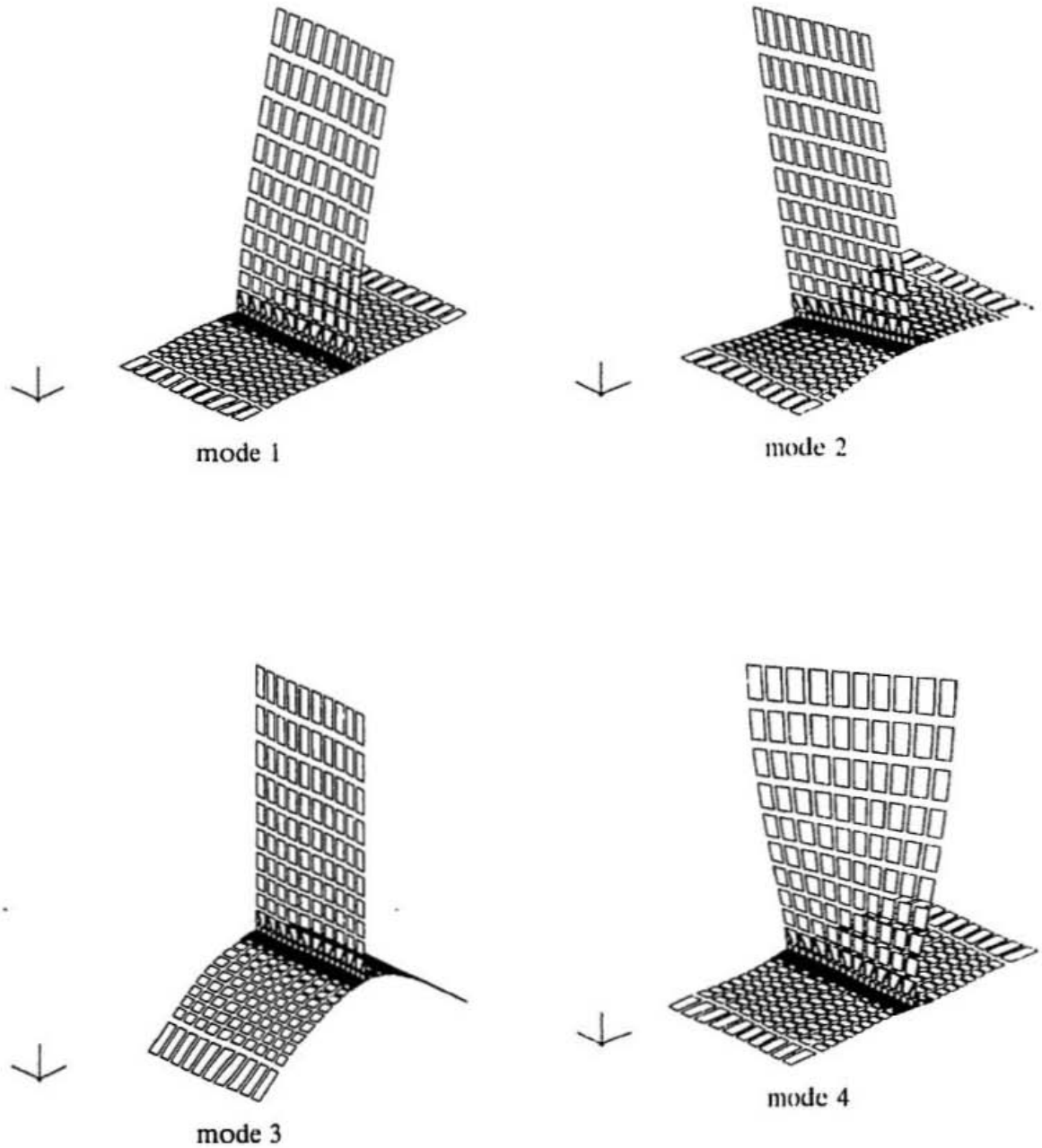

Figure 5.3 Mode shapes of the plated T-joint

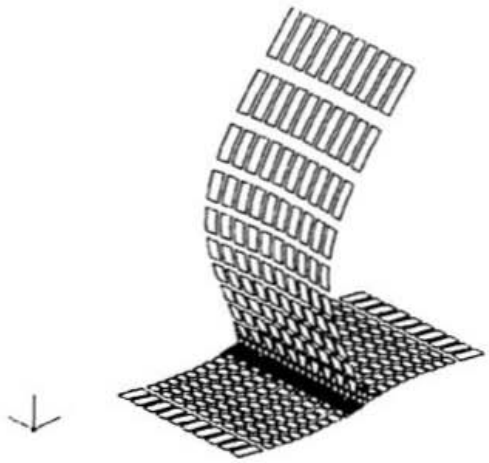

mode 5

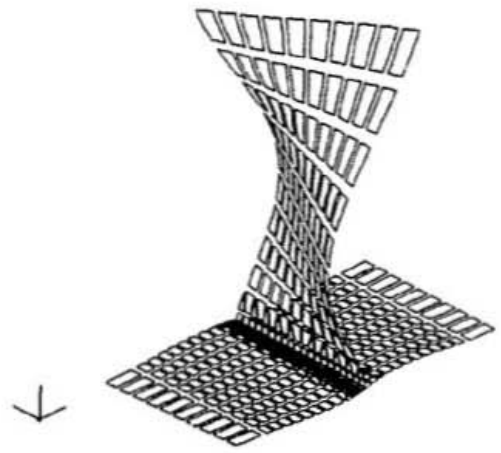

mode 6

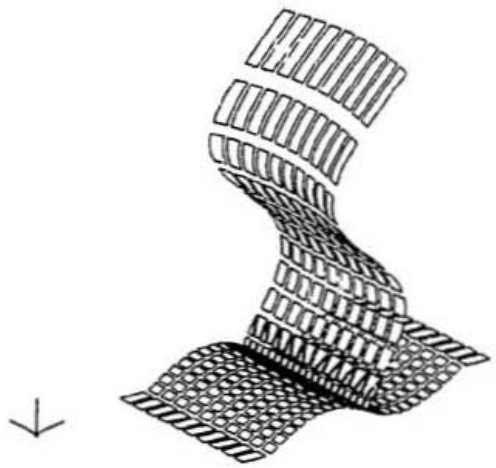

mode 7

Figure 5.3 (cont'd)

In the present study, it was found that the simply supported condition applied to the FE model, did not truly represent the supporting conditions provided for the laboratory setup. In the laboratory setup, the base plate of the T-plate joint was kept in position by two cylindrical steel rods with a certain amount of bottom plate projection outside these steel rod supports. This projection introduces some rotational restraints at these simply supported points. Further more, the welded region of the experimental plated T-joint would be much stiffer than the plated T-

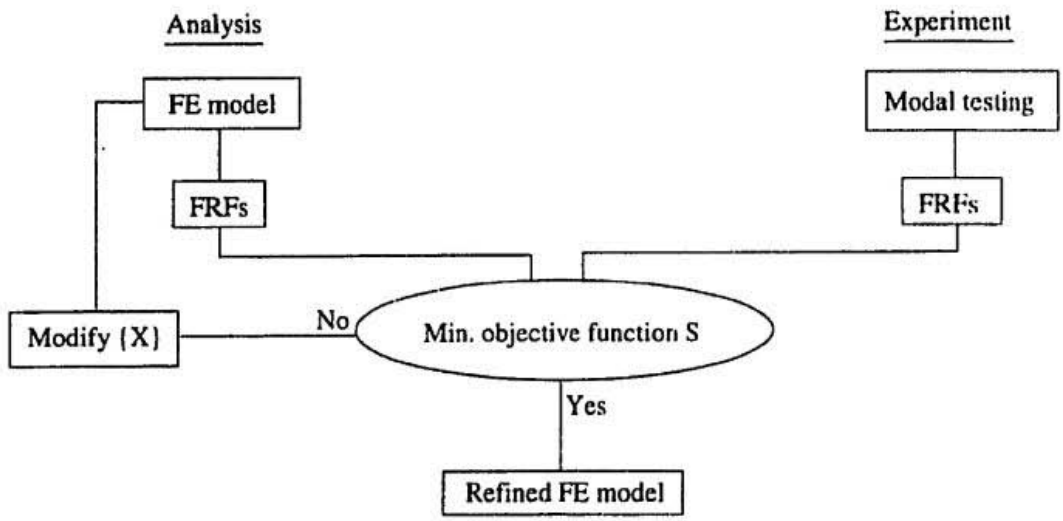

Figure 5.4 Procedure used for refining the FE model; {X} represents parameters that are varied

joint generated in the initial FE model; the FE model was obtained by joining together meshes of two finite elemented plates, perpendicular to one another. The thickness of the experimental plated T-joint was also not the same throughout. All these variations were taken into

consideration while refining the FE model. Figure 5.4 shows the procedure used to obtain the refined FE model, where the objective function S is the same as that discussed in Section 3.3, expressed as:

$$S = \sum_{i=1}^{n} \sum_{j=1}^{m} \left\{ \sum_{k=1}^{l} W_i \left[H_{jk}^{a}(\omega_i)^2 - H_{jk}^{e}(\omega_i)^2 \right] \right\} \qquad (5.1)$$

Damping ratios obtained from experiment were used in the FE model to generate the analytical FRF curves.

Table 5.2 compares the natural frequencies obtained from the refined model and experiment. For each specimen, the T-joint welding profile and the end supporting conditions would be slightly different from those of others. These differences have resulted in the variation between experimental and analytical natural frequencies. Therefore, a refined FE model has to be generated for each specimen. In this study, due to the improper inking and beach marking for the first two specimens, the crack profiles were not properly obtained for these two specimens. Therefore, the model updating procedure was applied only to the specimens #3 - #7.

During the process of model refinement, several parameters were slightly changed. They included Young's modulus, thickness plate, length and width of the plate, thickness around the weld toe and the boundary conditions at the supporting edges (by adding some rotational restraints).

Table 5.2 Natural frequencies obtained from each experimental specimen and the corresponding refined FE model

Natural freq. (Hz)		1st	2nd	3rd	4th	5th	6th	7th
	Initial FE model	75.295	137.67	220.05	336.82	470.80	1088.7	1291.1
speci. #3	Refined FE model	74.42	143.79	230.56	358.80	458.13	1110.1	1246.9
	Expt. model	75.73	153.78	230.44	-	454.21	1109.63	1246.36
speci. #4	Refined FE model	75.13	149.49	235.75	351.35	456.96	1094.4	1243.6
	Expt. model	75.84	153.10	235.19	-	457.89	1109.2	1242.1
speci. #5	Refined FE model	75.455	146.40	234.77	355.35	457.97	1102.0	1245.7
	Expt. model	75.998	165.17	234.15	-	467.13	1103.9	1245.6
speci. #6	Refined FE model	75.07	145.92	227.62	358.46	452.84	1100.8	1228.9
	Expt. model	75.54	-	227.26	-	456.44	1100.6	1228.7
speci. #7	Refined FE model	76.57	173.58	230.71	338.10	475.51	1090.0	1233.9
	Expt. model	76.03	174.63	230.39	-	468.56	1105.6	1233.2

As stated previously, the fourth mode could not be identified from the experiments due to the nature of that mode shape and the location of the sensors. Also it can be observed from Table 5.2, that the second natural frequency is not matched closely. In specimen #6, around the second resonant frequency double peaks were located very close to one another in the experimental FRFs, probably due to the vertical plate being welded non-centrally and at an

inclination to the plane perpendicular to the horizontal plate, providing two dissimilar configurations during the in-plane vibration of the vertical plate. Consequently the natural frequency of that particular mode could not be extracted. Also the deformation for this mode (second mode) was very small where the sensors were located. The signal level was comparable to the noise level, which made it very difficult to identify this mode exactly; this could have contributed heavily to the large differences observed between analytical and experimental FRFs around the second mode. Apart from these two modes, the rest of the five modes showed a very good match. More importantly if one looks at the generated FRFs as shown in Figure 5.5, the whole spectrum, especially at the dominant modes (i.e. third and seventh modes), is well matched between the FE and experimental models.

Figure 5.5 shows the FRFs of the refined analytical model and intact experimental model, obtained at points a1 and a11 for accelerations, and at s25 and s31 for surface strains, for specimen #7. It can be seen that differences between these two models become very small at the first, third, fifth, sixth and seventh modes. The two dominant modes, which are the third and seventh modes, are perfectly matched.

Similarly, for specimens #3 - #6, refined finite element models were generated. The strain FRFs of refined analytical model and intact experimental model, obtained at point s31, are given in Figures 5.6 - 5.9 for all the other specimens. It can be found that good agreements have been obtained between the two models around the dominant peaks. Analytical strain FRF seems to diverge considerably from the experimental strain FRF at low signal levels, for

specimens #3 and #4. It was found later on that this was produced due to the vibration of the supporting frame. After tightening the bolts connecting the floor and frame again, the fit between the refined FE model and intact experimental model was found to be very good, as seen for the specimens #5 - #7. It is noticed that at certain frequency ranges, the response output signals were very small; in the case of strain gauge output, these signals fall to the same level as the noise produced by this type of strain gauge in laboratory environments. For a better understanding of the behaviour around this frequency region, better strain gauges and instrument setup are required. However, in this study, the model updating procedure is based on the strain FRFs around the resonant frequencies (of T-joint), where good matchings were obtained between the analytical and intact experimental FRFs.

5.3 Model Updating With Experimental Data For Crack Detection

5.3.1 Initial step using changes in strain mode shapes

The idea of using model updating for crack detection is to modify the properties of the finite element model by introducing cracks into the structure. Since a finite element model normally consumes a large amount of computational time, it is essential to restrict the area of modification to a small number of elements so as to make the whole process practical and efficient. The initial step of using changes in the strain mode shapes could identify this small group of elements. From a previous study (Chen, 1993), it was known that changes in strain mode shapes were very sensitive to cracking compared to the changes in displacement mode

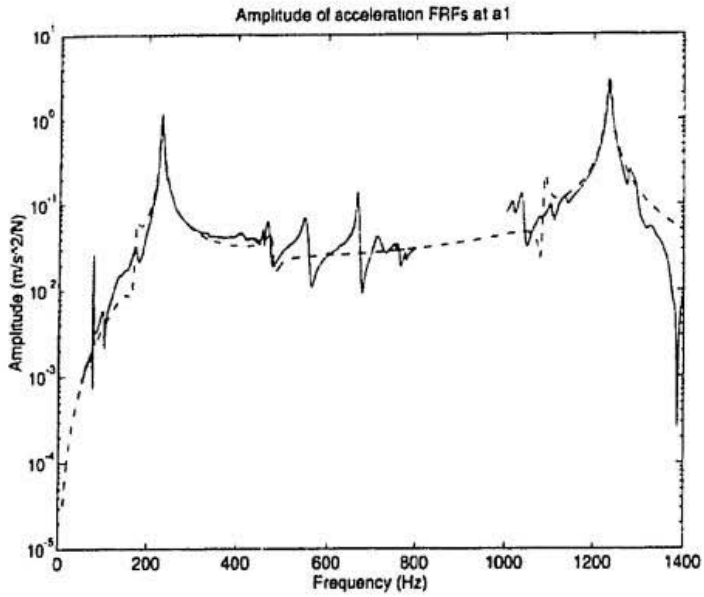

Figure 5.5 (a) Acceleration FRFs obtained from refined FE model and intact experimental model at location a1 for specimen #7. Solid line is for experimental model and dashed line is for FE model

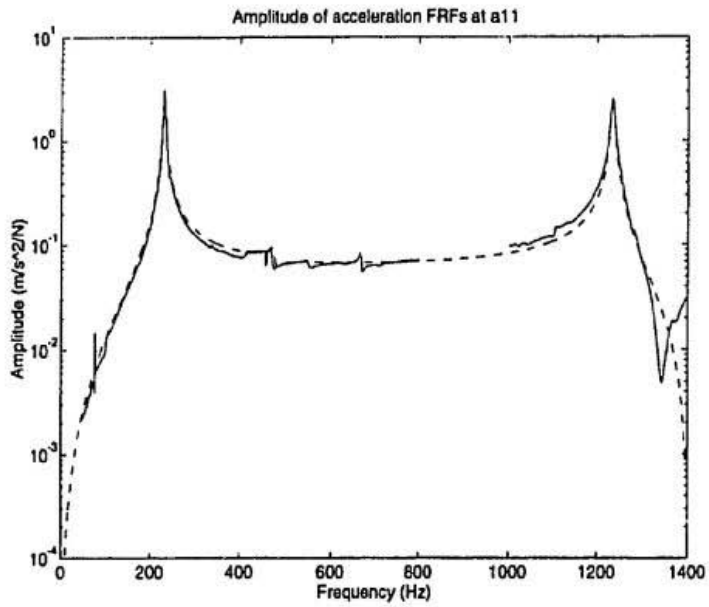

Figure 5.5(b) Acceleration FRFs obtained from refined FE model and intact experimental model at location a11 for specimen #7. Solid line is for experimental model and dashed line is for FE model

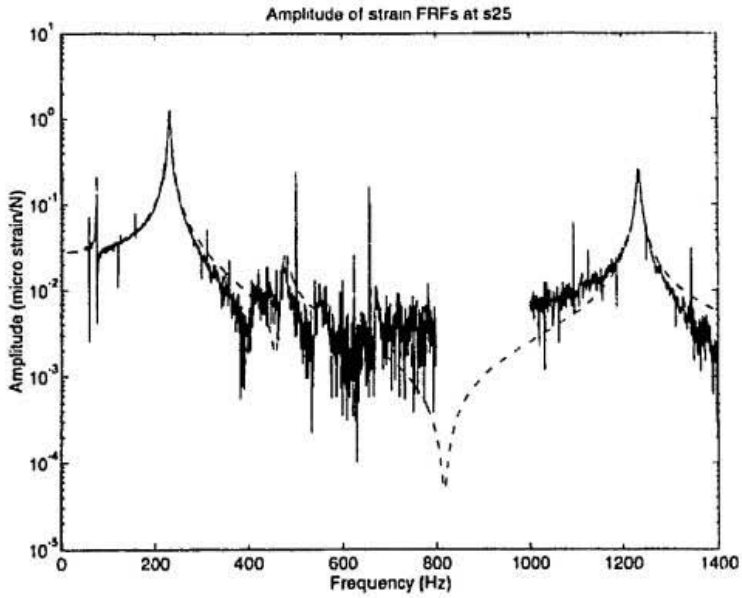

Figure 5.5 (c) Strain FRFs obtained from refined FE model and intact experimental model at location s25 for specimen #7. Solid line is for experimental model and dashed line is for FE model

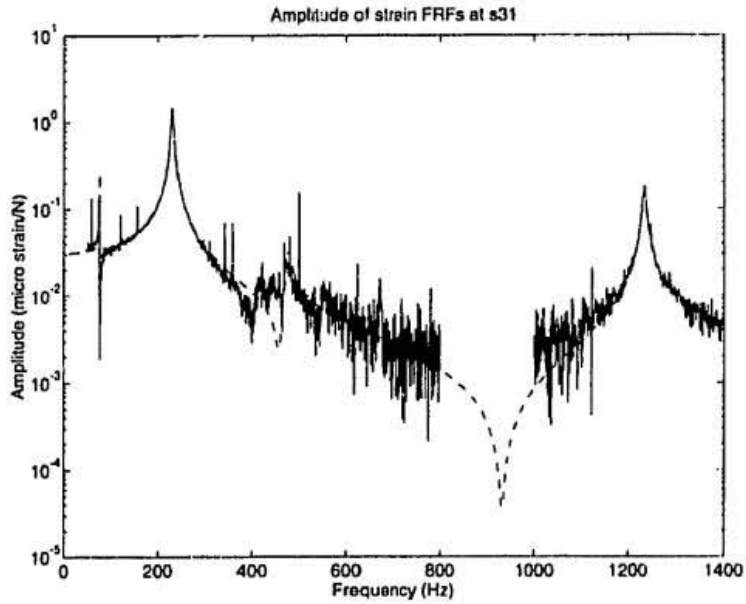

Figure 5.5(d) Strain FRFs obtained from refined FE model and intact experimental model at location s31 for specimen #7. Solid line is for experimental model and dashed line is for FE model

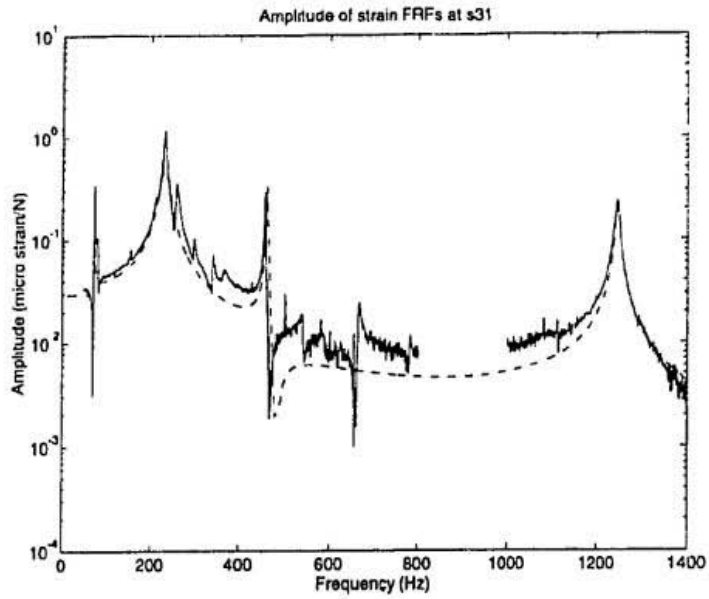

Figure 5.6 Strain FRFs obtained from refined FE model and intact experimental model at location s31 for specimen #3. Solid line is for experimental model and dashed line is for FE model

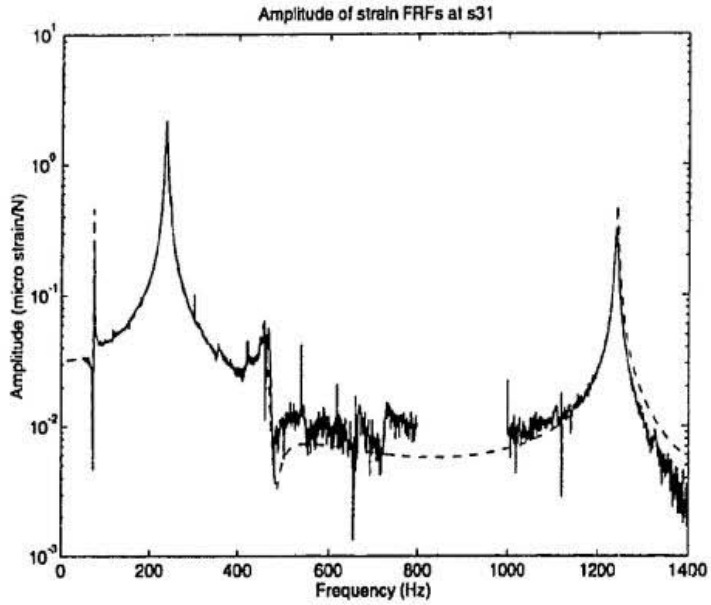

Figure 5.7 Strain FRFs obtained from refined FE model and intact experimental model at location s31 for specimen #4. Solid line is for experimental model and dashed line is for FE model

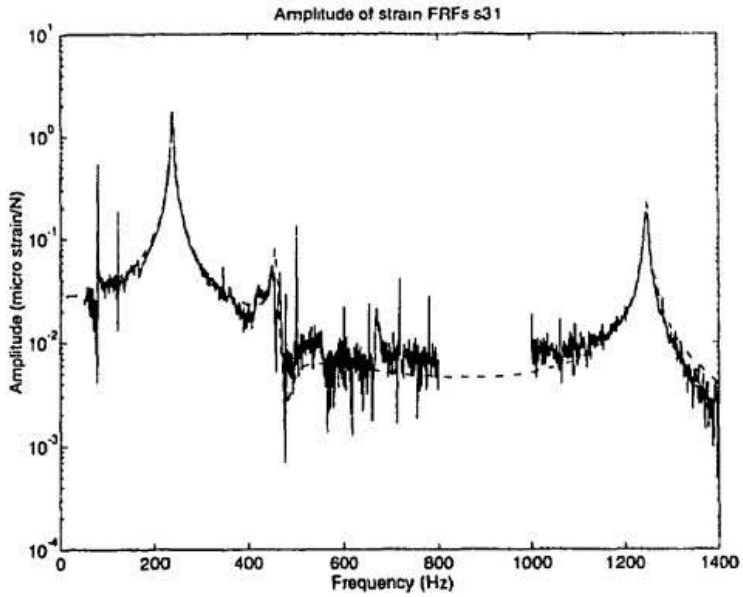

Figure 5.8 Strain FRFs obtained from refined FE model and intact experimental model at location s31 for specimen #5. Solid line is for experimental model and dashed line is for FE model

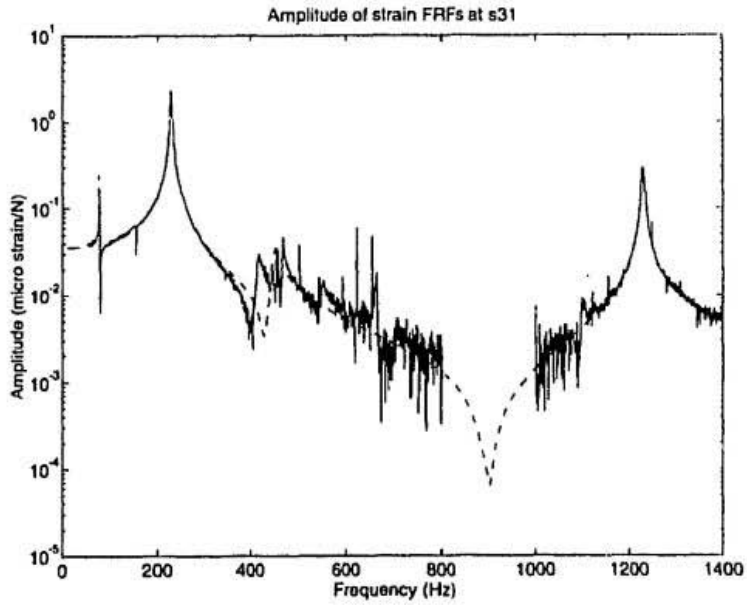

Figure 5.9 Strain FRFs obtained from refined FE model and intact experimental model at location s31 for specimen #6. Solid line is for experimental model and dashed line is for FE model

shapes. A sharp change in the strain mode shape would indicate a damaged zone around this area, although the quantity of damage would be difficult to determine by considering this change alone. Therefore, the initial step of crack detection using changes in strain mode shapes can approximately determine the zone of the possible crack, thereby reducing the number of finite elements that need to be modified in the model updating procedure. Figure 5.10 shows the first bending strain mode shape of specimen #3; it is observed from the figure that significant changes have occurred around the weld-toe, near one end of the weld-toe. The other specimens also show a similar pattern, wherein large changes occur somewhere along the weld-toe region. The main difference between various specimens is that this change could occur on either side of the centre of the weld toe region, or at the centre, depending on where the crack has initiated.

For complex structures, it may be difficult to obtain the experimental strain mode shapes. The modal constant (or the magnitude of the strain FRF at a point for a specific resonant mode) can be used to determine the strain mode shape value at any point under consideration. The possible crack area will be near the location (where the strain gauge is applied) corresponding to the largest change of magnitude in strain FRFs (refer Figure 4.16, where the largest change in strain FRFs occurred in gauge s31, close to the weld-toe). Thereafter a detailed investigation has to be carried out using the model updating procedure described below.

5.3.2 Perturbation based approach of model updating procedure for crack detection

As stated in Chapter 3, the objective function for the model updating procedure was chosen

The first bending strain mode shape of the intact T-joint

The first bending strain mode shape of the cracked T-joint (after ink staining)

Figure 5.10 Strain mode shapes, before and after cracking (specimen #3)

as follows:

$$S = \sum_{i=1}^{n}\sum_{j=1}^{m}\left\{\sum_{k=1}^{l} W_i\left[H_{jk}^{a}(\omega_i)^2 - H_{jk}^{c}(\omega_i)^2\right] - \Delta_{ijk}\right\} \qquad (5.2)$$

where H^a is the FRF obtained from the refined FE model, with a crack; H^c is the FRF obtained from the cracked experimental model. W_i is the weighting coefficient; Δ_{ijk} is the difference between the refined FE model and the intact experimental model; n is the number of natural frequencies to be considered; m is the number of the referenced FRF; and l is the number of points around the natural frequency in the FRF. Only the sections around the resonant region, that is the points on either side of the resonant frequency, were used in the calculation of the

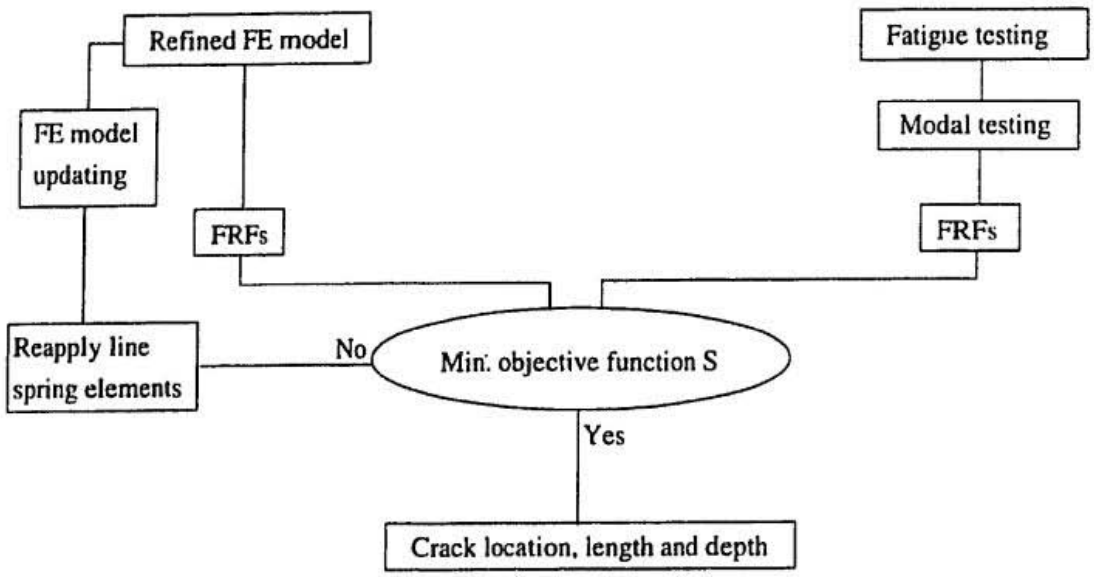

Figure 5.11 Procedure of model updating for crack detection

objective function. Figure 5.11 shows the procedure of model updating for crack detection.

Δ_{ijk} can be expressed as follows,

$$\Delta_{ijk} = \left[H_{jk}^{a}(\omega_i)\right]_0 - \left[H_{jk}^{e}(\omega_i)\right]_0 \tag{5.3}$$

It is assumed that the Δ_{ijk} is very small, and will continue to be a constant as the crack grows.

Because of the high sensitivities of strain FRFs at regions close to the crack, they were used in the model updating procedure. In this study, strain FRFs obtained from gauge numbers s26, s31 and s36 were used in the calculation of the objective function (refer to Figure 4.9 for

the positions). FRF values for five natural frequencies (1st, 3rd, 5th, 6th and 7th) were used in Eqn. (5.2) during model updating. As shown in Section 5.2, the refined FE model had a very good match with the intact experimental model for 1st, 3rd, 5th, 6th and 7th resonant frequencies, while 2nd and 4th frequencies were not very well matched in all the five specimens. From Figure 5.5, it can be seen that the dominant modes were the two bending modes of the bottom plate, namely, 3rd and 7th modes. If the crack occurs at the centre of the bottom plate then it will have a major influence on these two modes. Also, it is seen from Figure 5.5 that strain FRFs of the finite element model (of the intact structure) and the intact experimental model have a very good match at these two modes. Considering the above effects, the weighting coefficients W_i were chosen accordingly. It should also be pointed out that it is almost impossible to have a perfect match between the refined FE model and the intact experimental model, although a very close match is a necessary condition. These residual differences were taken into consideration in the objective function by the introduction of Δ_{ijk} in Eqn. (5.2). Also, in the experimental FRFs, there were some resonant peaks which were caused by the resonance of supporting frames. These resonant peaks will also affect the other peaks in the FRFs. Since the effect of these resonant peaks would rather tend to be a constant around the resonant peaks under consideration, this would also be represented by the term Δ_{ijk}.

The perturbation method discussed in section 3.3 was used in the model updating procedure. In this study, the design parameters were chosen as the surface length of the crack (L), the depth of the crack (D) and the location of the centre of surface crack (C), and the function S was minimized by changing these three parameters L, D and C. The final value of

L, D and C that gave the best fit to the experimental curves were taken as the correct length, depth and location of the crack. Line spring elements were used to simulate the surface crack present in the weld toe region of T-joint. During model updating, different crack depths were assigned to the nodal points with which line spring elements were associated; thus location, length and depth of the crack for all associated nodal points were obtained. While choosing the crack depth of line spring elements, it was assumed that the fatigue crack had a semi-elliptical profile.

Use of line spring elements with shell elements is an approximate method to model the surface crack on a plate. The assumption of a semi-elliptical profile for a fatigue crack may also differ from the real crack profile. The results from this study, presented in this chapter, show that these approximations are acceptable for practical situations.

The complete software programming for the model updating procedure was carried out in the following manner: The main control program, and programs for FRF plots and predicted crack profile plots were written using MATLAB. A sub-program that controls the running of ABAQUS, calculates the objective function S, and obtains the H^e from outputs of STAR STRUCT software was developed using C language. Another small sub-program was developed to obtain the H^a from the ABAQUS binary output file using FORTRAN language. The choice of different computer languages is based on efficiency and convenience.

As mentioned before, specimens #3, #4, #5, #6, and #7 were examined using model

updating procedure for crack detection. Furthermore, only specimen #7 was examined in detail for different crack growth intervals. For the remainder of the specimens, only the crack depth with ink staining mark was used to compare the results obtained from model updating. In this study, the element-by-element approach which utilizes three design parameters was used. Therefore the iteration steps required for a complete model updating procedure were quite large. It normally takes about 120 steps, and over 48 hours of total computer time (CPU + disk storage + output time in a multi-tasking environment) to complete one model updating procedure. For specimen #7, it was assumed that the crack occurred symmetrically and therefore C was taken as zero; thus the number of iteration steps was reduced considerably.

First, specimen #7 was examined for four different crack growth intervals. Figures 5.12-5.15 show the FRFs of the T-joint for different crack growth intervals, and the FRFs from the updated FE model corresponding to these crack growth intervals. These figures also compare the FRFs of cracked plate with the FRFs of intact plate (shown in dotted line). The final results of model updating procedure, which end up with the location, lengths and depths of the crack, are shown in Figure 5.16. The photo of the cracked cross-section of the plate was enhanced and sharpened to show the ink staining and beach marks which depict profiles of the crack at different crack growth intervals. When the crack initiated, of the three locations whose strain FRFs (at s26, s31 and s36) were used for calculating the error S, only the gauge s31 for which crack initiation occurred nearby, contributed heavily to the error S. As the crack grew, the FRFs at the other two points (s26 and s36) also experienced larger FRF magnitude changes around the resonant frequencies.

Table 5.3 gives the length and depth of crack computed for specimen #7 by the model updating procedure, and compares them with actual measured data.

Table 5.3 Predicted and measured crack length and depth at various crack growth intervals for specimen #7

Crack growth interval	4			5			6			7		
	C	L	D	C	L	D	C	L	D	C	L	D
measured (mm)	0.0	76.0	6.5	0.0	97.0	7.0	0.0	114.0	7.5	0.0	148.5	8.5
predicted (mm)	0.0	80.0	6.7	0.0	100.0	7.2	0.0	120.0	7.5	0.0	150.0	8.5
error (%)	0	-5.3	-3.1	0	-3.1	-2.9	0	-5.3	0	0	-1.4	0

C = centre of crack; L = length of crack; D = depth of crack.

For the remainder of the specimens, the same model updating procedure was utilized. Only one fatigue crack growth interval was investigated, namely the crack growth interval at which ink staining was used to mark the crack profile. Figures 5.17 - 5.24 show strain FRFs at s31 obtained by model updating procedure, and the measured/predicted crack profiles for specimens #3, #4, #5, and #6. Table 5.4 gives the location, length and depth of the crack for these specimens.

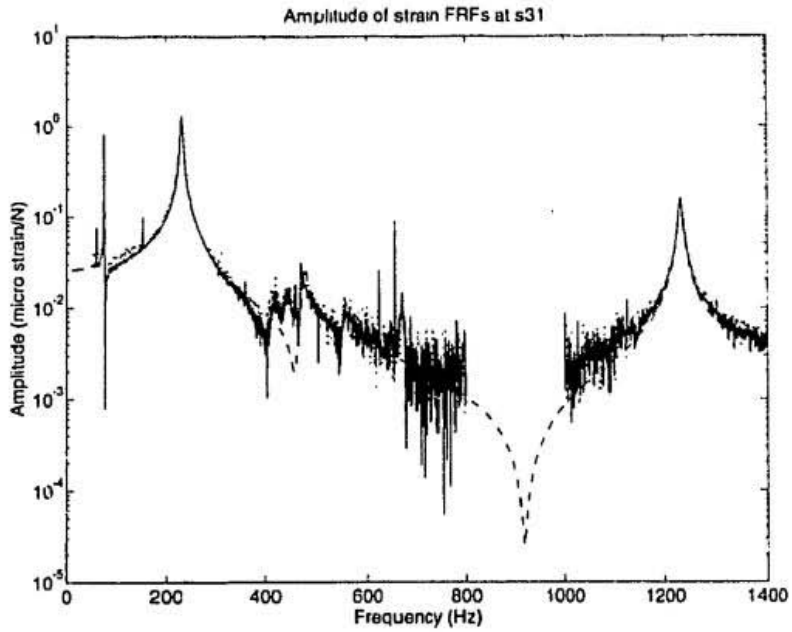

Figure 5.12 Strain FRFs at crack growth interval 4 for T-joint #7 at location s31. Solid line: cracked specimen; dashed line: FE model; dotted line: intact specimen

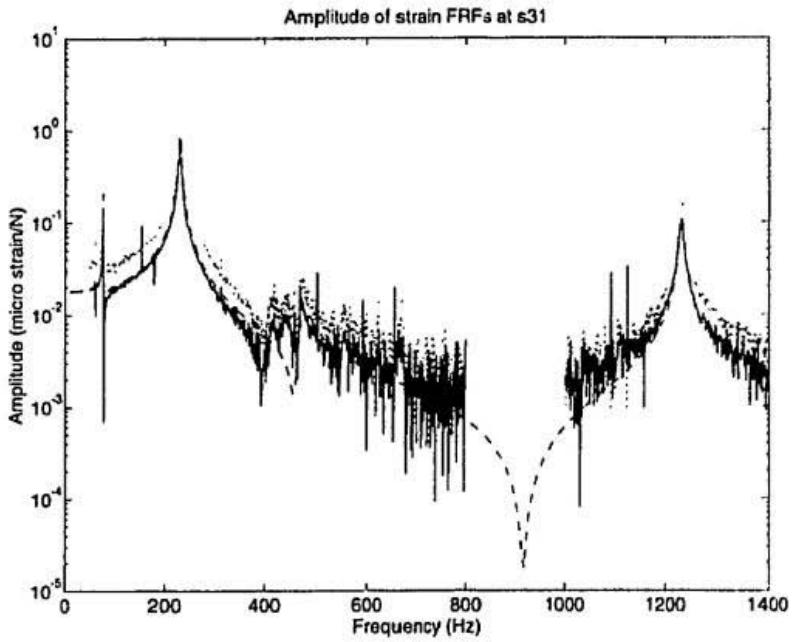

Figure 5.13 Strain FRFs at crack growth interval 5 for T-joint #7 at location s31. Solid line: cracked specimen; dashed line: FE model; dotted line: intact specimen

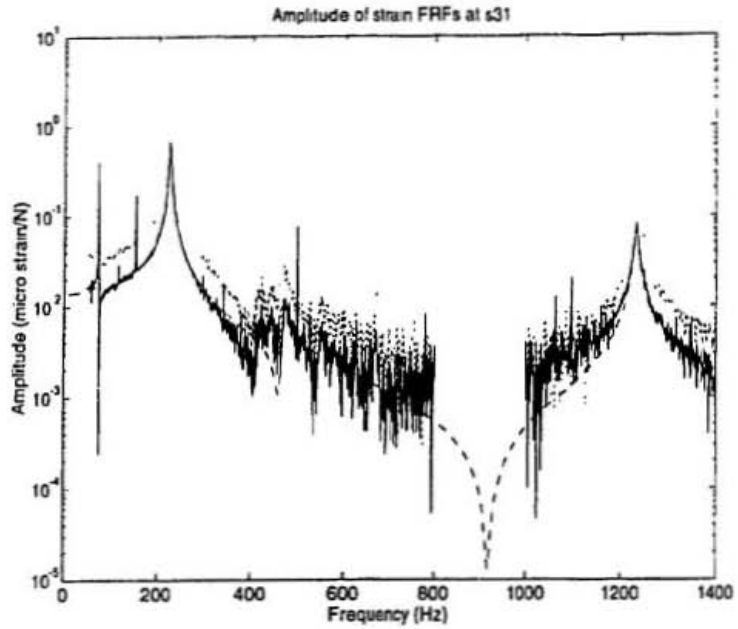

Figure 5.14 Strain FRFs at crack growth interval 6 for T-joint #7 at location s31. Solid line: cracked specimen; dashed line: FE model; dotted line: intact specimen

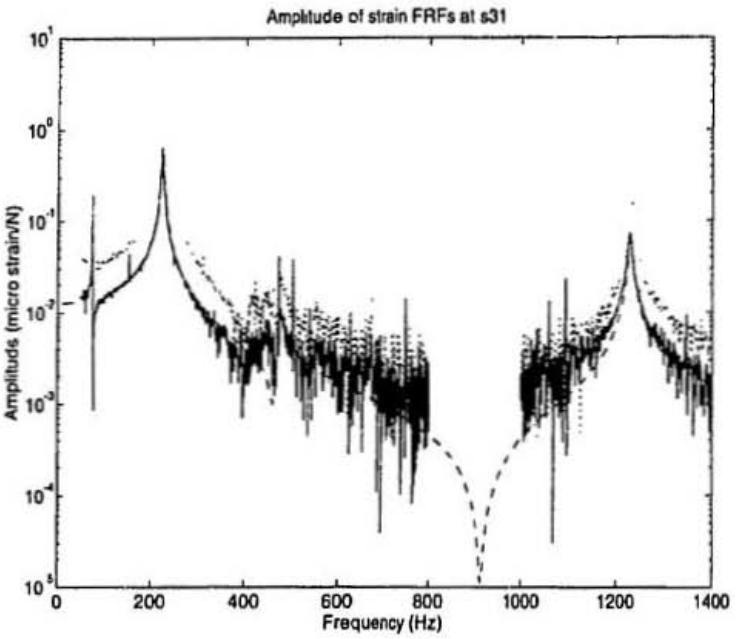

Figure 5.15 Strain FRFs at crack growth interval 7 for T-joint #7 at location s31. Solid line: cracked specimen; dashed line: FE model; dotted line: intact specimen

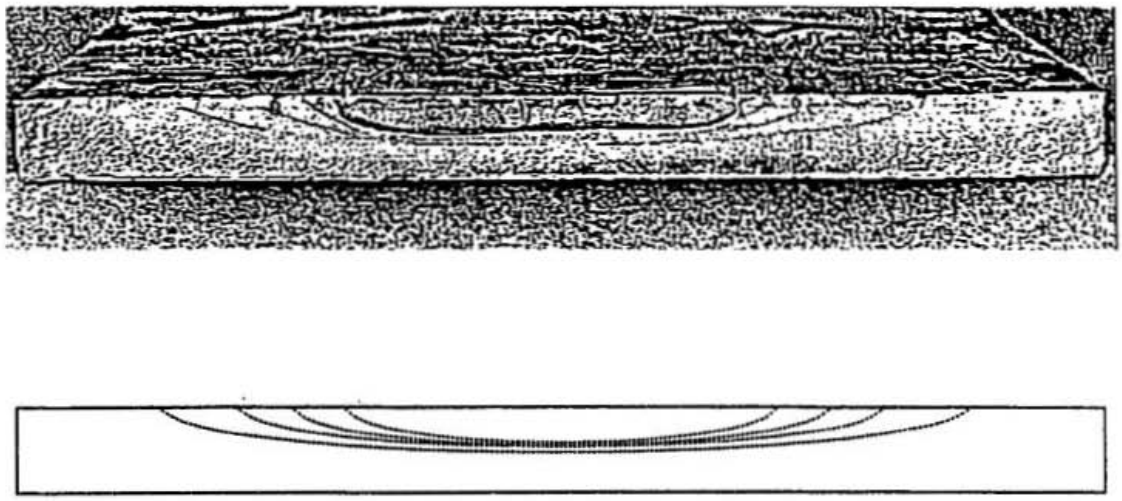

Figure 5.16 Measured and predicted crack profile for the specimen #7, at different crack growth intervals

From Tables 5.3 and 5.4, it can be seen that the crack length, depth and location were successfully predicted using the model updating procedure. When the crack initiated symmetrically, which occurred for specimen #7, the model updating procedure gave more accurate prediction than others. Invariably there are still some residual errors existing in this procedure. One reason for this error is that the refined finite element model was not exactly the same as that of the experimental model. From Figures 5.5 - 5.9, it can be seen that although the FRFs from the finite element model and the experimental model were very close around the resonant regions, there are still some differences; this difference is given by Δ as defined in Eqn. (5.3). Since changes in FRFs caused by the crack are also small, errors will inevitably be introduced. Another reason for this error is that the length (L) increment in model updating procedure was chosen as 5 mm; this is justified by the fact that the change in length of the crack

was not as sensitive as the change in depth for modifying the magnitude of strain FRFs. Moreover this increment was also adopted to reduce the number of iterations needed for the whole updating procedure.

Table 5.4 Predicted and measured crack location, length and depth for the remainder of test specimens

Particulars	specimen #3			specimen #4			specimen #5			specimen #6		
	L	D	C	L	D	C	L	D	C	L	D	C
measured (mm)	36.0	7.5	101.5	119.0	8.5	42.0	48.0	4.5	68.0	41.0	7.5	34.0
predicted (mm)	40.0	8.0	90.0	125.0	8.8	40.0	50.0	4.9	60.0	45.0	7.9	30.0
error (%)	-11.1	-6.7	11.3	-5.0	-3.5	4.8	-4.2	-8.9	11.8	-9.8	-5.3	11.8

L: length of crack; D: depth of crack; C: centre of crack (from the middle of the plate).

5.4 Discussions and Summary

It is found from this study that a very important aspect in using model updating procedure for crack detection is the obtaining of a refined finite element model. In Eqn. (5.3), it is shown that the differences between FRFs of the finite element model with no crack and the intact experimental model is given by,

$$\Delta = H_0^a - H_0^e \tag{5.4}$$

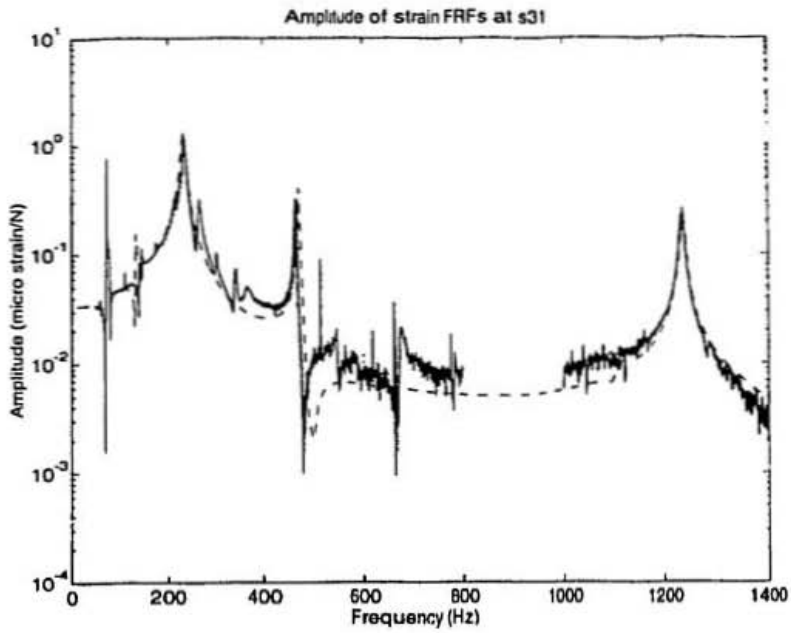

Figure 5.17 Strain FRFs of specimen #3 at location s31. Solid line: cracked specimen; dashed line: FE model; dotted line: intact specimen

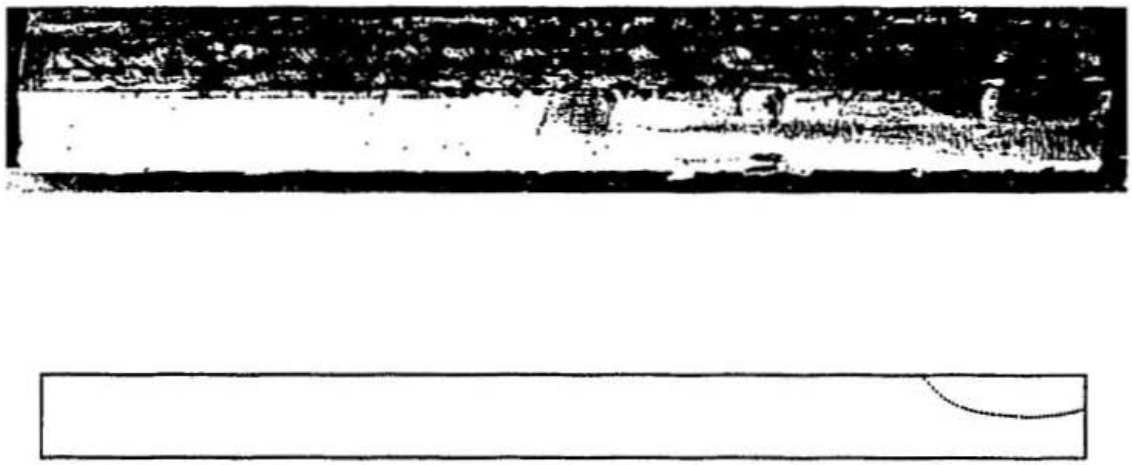

Figure 5.18 Measured (ink staining) and predicted crack profile for specimen #3

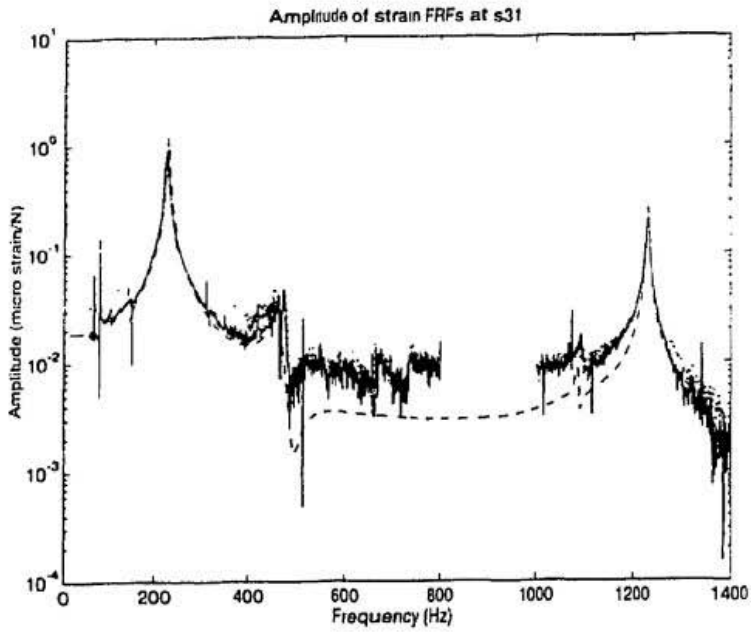

Figure 5.19 Strain FRFs of specimen #4 at location s31. Solid line: cracked specimen; dashed line: FE model; dotted line: intact specimen

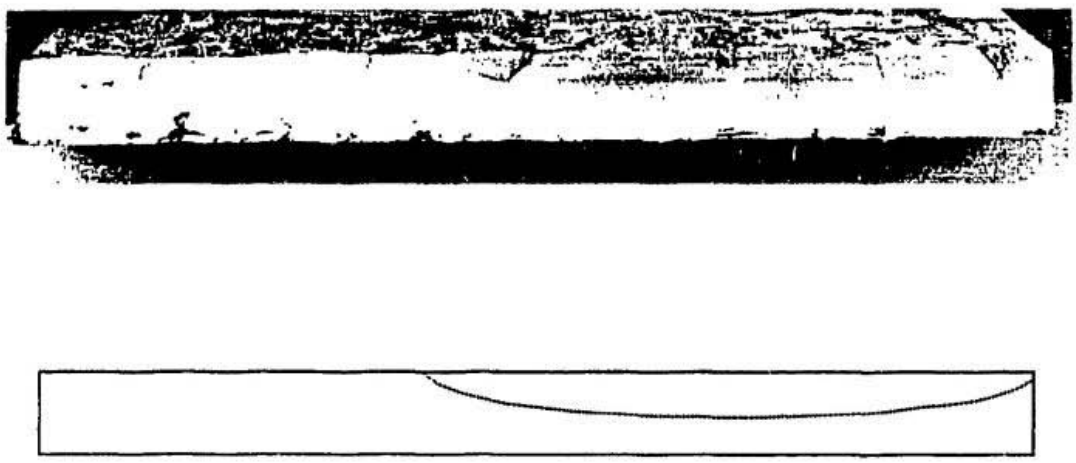

Figure 5.20 Measured (ink staining) and predicted crack profile for specimen #4

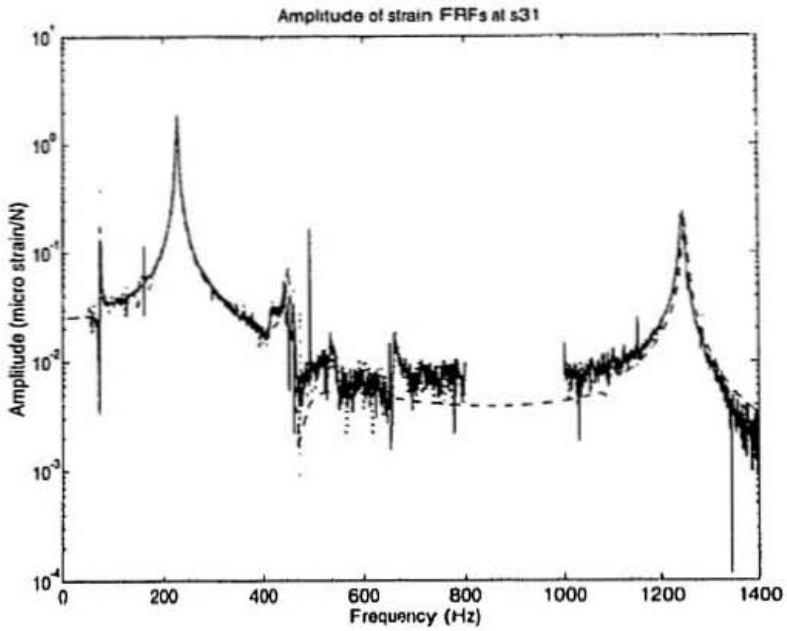

Figure 5.21 Strain FRFs of specimen #5 at location s31. Solid line: cracked specimen; dashed line: FE model; dotted line: intact specimen

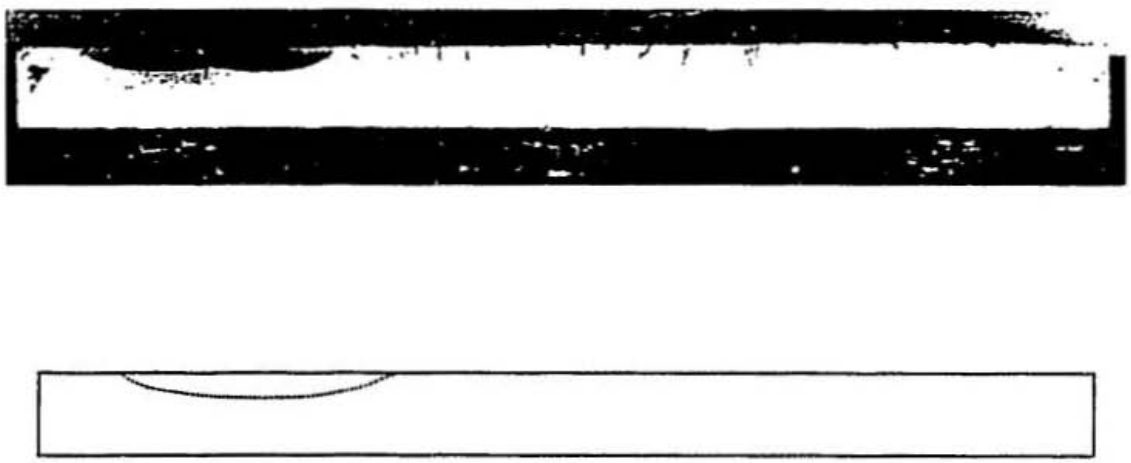

Figure 5.22 Measured (ink staining) and predicted crack profile for specimen #5

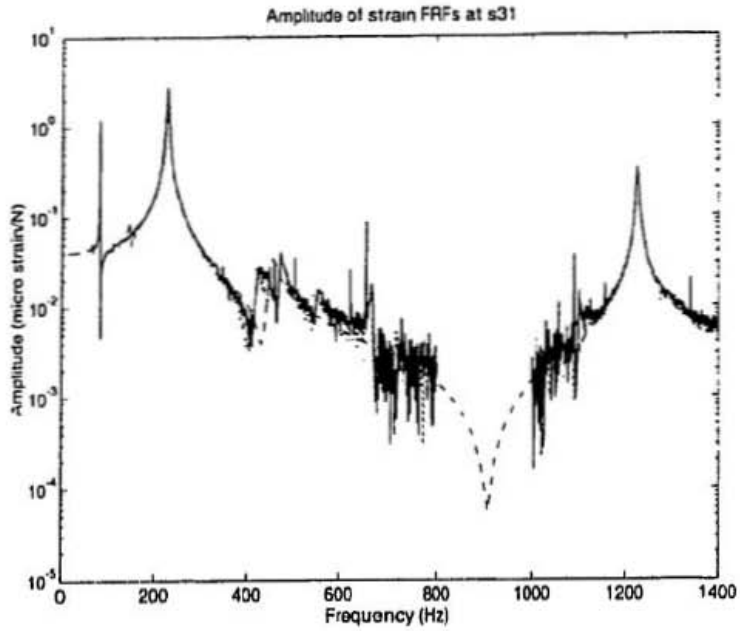

Figure 5.23 Strain FRFs of specimen #6 at location s31. Solid line: cracked specimen: dashed line: FE model; dotted line: intact specimen

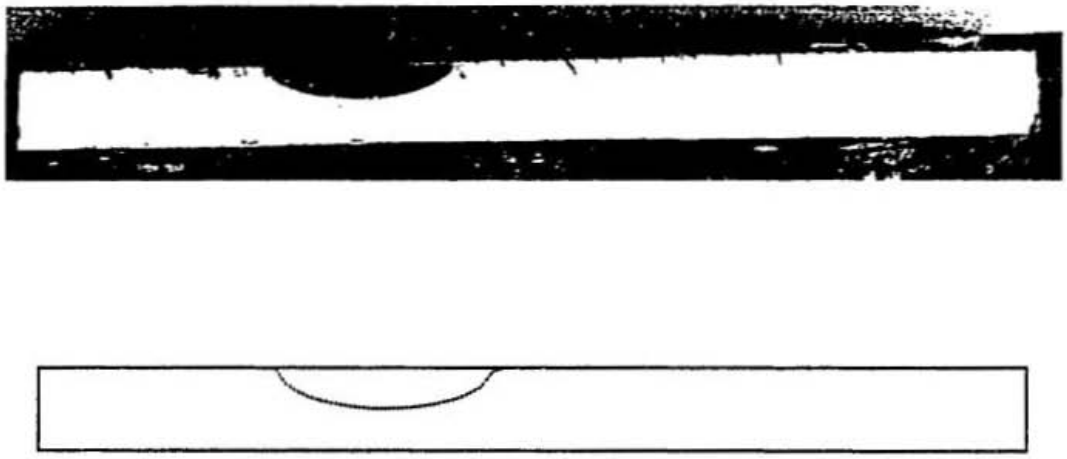

Figure 5.24 Measured (ink staining) and predicted crack profile for specimen #6

Let us denote the changes of experimental FRFs caused by crack as,

$$\delta^c = H_c^c - H_0^c \tag{5.5}$$

In using the model updating procedure it was observed that the procedure gave a good prediction only when δ^c was larger than Δ. When δ^c was comparable or less than Δ, unreliable results were obtained. In this study, an effort was made to use the FRFs at s25 or a11 in the objective function of Eqn. (5.2) and determine the crack location, length and depth; the updating procedure failed to give a reasonable crack prediction. In order to have a good prediction using model updating procedure, one should have either a lower Δ, or a higher δ^c.

First, let us see how Δ could be lowered. In order to lower it, an accurate and fine tuned finite element model has to be generated. In this study, for example, one will obtain more accurate results if the T-joint hot spot area was modelled using 3-D finite elements and 3-D singular crack elements. This approach would require a computer with a very large in-core memory and efficient computational algorithms. Also the model updating procedure would require a large number of iterations to minimize the error S, which would mean that the speed of the computer had to be fast enough to be practically usable.

Second, let us see how δ^c could be increased. This approach would save a lot of time spent on computer modelling and computations. It is shown from this study that local strain FRFs around the crack area are very sensitive to cracking. Although the T-joint was modelled complete with plate elements (instead of 3-D elements at brace-chord junctions and plate

elements everywhere else), and the crack was simulated by line spring elements (instead of singular crack elements), a good crack prediction has been achieved (as shown from the results). One drawback of this approach in real structures is finding this critical area. It means that a certain number of strain gauges have to be applied around critical areas.

In general, this study provides a new methodology for crack detection in plate-type structures. The critical joint area can be modelled using shallow shell elements and line spring elements can be used to simulate the crack. Local strain frequency response functions, which are very sensitive to cracking, can be used in the objective function for the model updating procedure. By carefully choosing the location of strain gauges, certain pre-assigned accuracy in generating the refined finite element model, and using proper weighting coefficients for calculating the error S, a good prediction which will give results close to the actual crack length, depth and location can be achieved.

Some of the salient results reported in this chapter include: (i) Prediction of detailed crack profiles (location, surface length and depth) that compare very well with the measured experimental values for all the plated T-joints tested; (ii) Development of a refined FE model that matches closely the FRFs of the experimental model; and (iii) The application of model updating procedure for crack detection in plate-type structures.

CHAPTER 6

CONCLUSIONS

A crack detection method using model updating procedure was presented in this study. In order to develop a perspective view of the problem, a state-of-art study on crack identification and detection was carried out identifying salient development and methodologies.

Two different methods based on (i) An optimization procedure followed by minimization using Lagrangian multipliers, and (ii) Minimization based on perturbation of pertinent parameters were investigated and the perturbation-based minimization method adopted for investigating the problem, due to its suitability and applicability. An experimental study was carried out on seven plated T-joints fatiguing them to a predefined cycle level and then carrying out dynamic modal testing to identify characteristic dynamic modal parameters. For the seven tests different fatigue load ratios were used (viz., -1 and 0) to make the procedure more general. Ink staining and beach marking procedures were used to delineate the experimental crack profiles obtained during the fatigue crack growth interval. After the experiment the joint was broken open, the crack profile photographed and transferred to computer images by scanning and stored in computer

files.

Finite element studies were carried out for uncracked plated T-joint model and combined with the results of the above mentioned experimental study on uncracked T-joints (using model updating procedure) to generate a refined uncracked analytical model. Using this refined analytical model and line spring elements to model the crack, the results of the experimental study were combined with the progressive crack growth development in the analytical model to identify crack location and size. The error between the identified cracked analytical model and cracked experimental model varied between 0 to 12 %, the minimum error obtained being for symmetric central cracking in plated T-joints and the maximum error for asymmetric noncentral cracking.

Based on these studies, major contributions of this study are given as: (i) Use of model updating procedures based on the perturbation method, and the use of the difference of the strain mode shapes to locate the crack; (ii) Development of a model updating procedure (using line spring elements) that can adjust the length and depth of the crack automatically for model updating; and (iii) Determination of the location, length and depth of fatigue cracks in a plate-type structure and verifying the accuracy of this procedure on five tested T-joints. The methodology developed and presented here and the accuracy the method was able to achieve in solving a crack detection problem have not been available in the open literature to-date.

As a consequence of this study, a crack detection methodology using model updating

procedure for plate-type structures can be described as follows:

i) Apply strain gauges around critical areas of the structure, determined earlier from finite element analysis or any other applicable method.

ii) Then carry out modal tests on the initial intact prototype structure, and record the FRFs.

iii) Thereafter generate a calibrated finite element model, and refine it as close as possible to the real intact structure by matching the corresponding FRFs.

iv) When the structure has undergone some fatigue cracking, due to in-situ loading conditions, carry out modal testing once again and obtain FRFs for this damaged structure.

v) Compare these FRFs with the calibrated FRFs of the prototype structure. If no changes occur between the refined analytical model and the experimental model, then the structure has not developed any further crack growth; if there are some changes, especially when there are frequency shifts and amplitude changes at certain points, more detailed investigations are required to determine whether these changes are caused by a crack or by other changes that occur in a structure such as soil erosion and strength degradation around pile embedment locations, biogrowth on the structure or mass changes occurring on the top of the offshore platform (due to drill pipe stacking or

usage, drill mud storage or depletion etc.)

vi) If the changes are identified as those due to cracking, then modify the refined finite element model by introducing cracks at those points where the magnitude of the FRFs decreased/increased the most. Use model updating procedure to determine the location and extent of cracking. By varying the length and the depth of the crack and the location of the crack, within some small range, the final accurate estimation of the crack could be made at the end of the procedure.

Although the study was applied only to plated T-joints, the procedure mentioned above could be applied to any kind of structure. The real challenge for a complex structure would be the creation of the refined finite element model. Because a small crack will have a significant effect only locally, which would be shown by the changes in the local strain FRFs, a fine mesh is necessary for the FE model to simulate the exact geometry and boundary conditions. Based on this fine mesh, cracks could be introduced into the refined finite element model to simulate the real fatigue cracks. Use of these fine meshes in certain areas may require a large amount of computer space and a faster computer speed so that a workable finite element model could be made for complex structures. Since the computer industry is developing at a rapid speed, this technique could be easily applied to more complex structures.

The other advantage of the model updating procedure, besides the accurate estimation of the fatigue crack profile, is the identification of changes caused by other effects. For example,

in offshore structures, many factors besides cracking will affect the dynamic behaviour of structures. Marine growth, change of deck weights, soil erosion at base of platforms, etc. will also affect the various modal parameters. But, the type of changes caused by the above mentioned factors, would be different from that obtained due to cracking at the welded joints of these structures. One major difference will be the changes obtained for strain FRFs. Occurrence of a crack at one joint of a structure will cause comparatively larger changes in magnitude of strain FRFs around the cracked area as well as frequency shifts and show only frequency shifts for FRFs of other areas. Other factors such as marine growth, soil erosion and mass changes will normally cause global changes all over the structure. By examining the updated finite element model, and comparing it with the experimental FRFs of the real structure, it should be possible to distinguish the changes in FRFs caused by fatigue cracks from other factors. It is suggested that further research investigation be carried out in this area using the model updating procedure presented in this study for more realistic structures under realistic environments (other than laboratory conditions); also validity of the model updating procedure to ascertain changes due to sub-sea marine growth, soil erosion and deck mass changes needs to be established for laboratory or prototype conditions.

REFERENCES AND BIBLIOGRAPHY

Adams, R.D., Cawley, P., Pye, C.J. and Stone, B.J., 1978. "A Vibration Technique for Non-Destructively Assessing the Integrity of Structures", Journal of Mechanical Engineering Science, V. 20, pp. 93 - 100.

Allemang, R., 1993. "Modal Analysis - Where Do We Go From Here?", Proceedings of the 11th International Modal Analysis Conference, Vol. I, pp. xxii - xxxi.

Bathe, K., 1982. "Finite Element Procedures in Engineering Analysis", Prentice-Hall, Inc., ISBN 0-13-317305-4.

Bernasconi, O. and Ewins, D.J., 1989. "Modal Strain/stress Fields", The International Journal of Analytical and Experimental Modal Analysis", Vol. 4, No. 2, April, pp. 68 - 76.

Brüel & Kjær (DK - 2850, Naerum, Denmark), 1987. "Dual Channel Signal Analyzer Type 2034, Instruction Manual".

Chen, Y., 1993. "Dynamic Characteristics and Modal Parameters of a Plate With a Surface Crack", Master's thesis, Memorial Univ. of Nfld., St.John's, NF, Canada, 95 pages.

Chen, Y. and Swamidas, A.S.J., 1993. "Modal Changes to Crack Growth in a Tripod Tower Platform", Canadian Journal of Civil Engineering, Vol. 20, pp. 801 - 813.

Chondros, T.G. and Dimarogonas, A.D., 1980. "Identification of Cracks in Welded Joints of Complex Structures", Journal of Sound and Vibration, Vol. 69(4), pp. 531 - 538.

Chondros, T.G. and Dimarogonas, A.D., 1989. "Dynamic Sensitivity of Structures to Cracks", Journal of Vibration, Acoustics, Stress, and Reliability in Design, Vol. 111, pp. 251 - 256.

Collins, K.R., Plaut, R.H., and Wauer, J., 1992. "Free and Forced Longitudinal Vibrations of a Cantilevered Bar with a Crack", Journal of Vibration and Acoustics, Vol. 114, pp. 171 - 177.

Doebling, S.W., Farrar, C.R., Prime, M.B., and Shevitz, D.W., 1996. "Damage Identification and Health Monitoring of Structural and Mechanical System From Changes in Their Vibration Characteristics: A Literature Review", Los Alamos National Laboratory report # LA-13070-MS, May, 127 pages; contains 309 references on various aspects of cracking.

Doebling, S.W., Hemez, F.M., Barlow, M.S., Peterson, L.D., and Farhat, C., 1993. "Damage Detection in a Suspended Scale Model Truss via Modal Update", Proceedings of the 11th International Modal Analysis Conference, Vol. II, pp. 1083 - 1094.

Ewins, D.J., 1996. "Modal Testing: Theory and Practice", Research Studies Press, ISBN 0 86380 017 3.

Gomes, A.J.M.A. and Silva, J.M.M., 1991. "Theoretical and Experimental Data on Crack Depth Effects in the Dynamic Behaviour of Free-free Beams", Proceedings of the IXth International Modal Analysis Conference, Italy, April, Vol. I, pp. 274 - 283.

Gomes, A.J.M.A. and Silva, J.M.M., 1990. "On the Use of Modal Analysis for Crack Identification", Proceedings of the VIIIth International Modal Analysis Conference, Florida, U.S.A., Vol. II, pp. 1108 - 1115.

Guigne, J.Y., Klein, K., Swamidas, A.S.J., and Guzzwell, J., 1992. "Modal Information from Acoustic Measurements for Fatigue Crack Detection Applications", Proceedings of the 11th International Conference on Offshore Mechanics and Arctic Engineering, Vol.I, Part B. pp. 585 - 594.

Harris, C.E., and Heyman, J.S., 1993. "Overview of NASA Research Related to the Aging Commercial Transport Fleet", Journal of Aircraft, Vol.30, No.1, Jan-Feb, pp. 64 - 68.

Hearn, G. and Testa, R.B , 1991. "Modal Analysis for Damage Detection in Structures", Journal of Structural Engineering, Vol. 117, No. 10, Oct., pp. 3042 - 3063.

Hibbitt, Karlsson & Sorenson, Inc. (1080 Main Street, Pawtucket, R.I. USA), 1995. "ABAQUS/Standard User's Manual, Version 5.4".

Hibbitt, Karlsson & Sorenson, Inc., 1995. "ABAQUS Theory Manual, Version 5.4".

Hibbitt, Karlsson & Sorenson, Inc., 1991. "Fracture Mechanics - Notes".

Jeong, W. B., and Nagamatsu, A., 1992. "A New Approach for Identification of Physical matrices by Modal Testing", Proceedings of the 10th International Modal Analysis Conference, Vol. I, pp. 265 - 271.

Kaouk, M., and Zimmerman, D.C., 1993. "Evaluation of the Minimum Rank Update in Damage Detection: An Experimental Study", Proceeding of the 11th International Modal Analysis Conference, Vol. II, pp. 1061 - 1068.

Kim, H.M., Bartkowicz, T.J., Smith, S.W., and Zimmerman, D.C., 1995. "Health Monitoring of Large Structures", Sound and Vibration, April, pp. 18 - 21.

Li, D., Zhuge, H., and Wang, B., 1989. "The Principle and Techniques of Experimental Strain Modal Analysis", Proceeding of VIIth International Modal Analysis Conference, Las Vegas, U.S.A., Vol. II, pp. 1285 - 1289.

Newton, K., 1990. "Development of New Techniques for Underwater Inspection of Offshore Structures", Proceeding of 9th International Conference of Offshore Mechanics and Arctic Engineering, Vol.3, Part B, pp. 547 - 553.

Nwosu, D.I., 1993. "Fatigue Strength Analysis of Offshore Tubular Welded Joints Under Constant Amplitude Loading: Local Strain and Fracture Mechanics Approach", Ph.D. thesis

submitted to School of Graduate Studies, Memorial University of Newfoundland, February, 323 pages.

Pandey, A.K., Biswas, M., and Samman, M.M., 1991. "Damage Detection from Changes in Curvature Mode Shapes", Journal of Sound and Vibration, Vol.145 (2), pp. 321 - 332.

Pouet, B.F., 1993. "Additive/subtractive Decorrelated Electronic Speckle Pattern Interferometry", Optical Engineering, June, Vol.32, No.6, pp. 1360 - 1369.

Richardson, M.H., and Mannan, M.A., 1991. "Determination of Modal Sensitivity Functions for Location of Structural Faults", Proceedings of the IXth International Modal Analysis Conference, Italy, Vol. I, pp. 670 - 676.

Rogers, L.M., 1987. "Detection and Monitoring of Cracks in Offshore Structures by Acoustic Emission", Offshore and Arctic Operations Symposium, ASME, Vol.10, pp. 55 - 60.

Rytter, A., 1993. "Vibrational Based Inspection of Civil Engineering Structures", Ph.D. thesis, Department of Building Technology and Structural Engineering, University of Aalborg, Aalborg, Denmark. This thesis lists 178 references on various aspects of cracking.

Salawu, O.S., and Williams, C., 1993. "Structural Damage Detection Using Experimental Modal Analysis - A Comparison of Some Methods", Proceedings of 11th International Modal Analysis Conference, Vol.I, pp. 254 - 260.

SDRC (Structural Dynamics Research Corporation, 2000 Eastman Drive, Milford, Ohio, USA), 1990. "I-DEAS USER'S GUIDE - TEST".

Shahriver, F. and Bouwkamp, J.G., 1986. "Damage Detection in Offshore Platform Using Vibration Information", Journal of Energy Resources Technology, Transaction of the ASME, June, Vol. 108, pp. 97 - 106.

Silva, J.M.M., and Gomes, A.J.A., 1992. "On the Use of Modal Analysis for Fatigue Crack Detection in Simple Structural Elements", Proceedings of the XIth International Conference on Offshore Mechanics and Arctic Engineering, Calgary, Canada, Vol. I, Part B, pp. 595 - 600.

Spectral Dynamics, Inc. (GenRad Inc., 2855 Bowers Avenue, Santa Clara, California USA), 1994. "STAR System Reference Manual".

Springer, W.T., Stuff, S.A., Coleman, A.D., and Driskell, T.A., 1991. "Simulating the Presence of Damage in a Vibrating Structure with Finite Element and Structural Dynamics Modification Techniques", Proceedings of the IXth International Modal Analysis Conference, Italy, Vol. II, pp. 1108 - 1109.

Stubbs, N., and Osegueda, R., 1990. "Global Non-Destructive Damage Evaluation in Solids", The International Journal of Analytical and Experimental Modal Analysis, 1990 Apr., pp. 67 - 79.

Swamidas, A.S.J. and Chen, Y., 1992. "Damage Detection in a Tripod Tower Platform (TTP) Using Modal Analysis", Proceedings of the XIth International Conference on Offshore Mechanics and Arctic Engineering, Calgary, Canada, Vol. I, Part B, pp. 577 - 583.

APPENDIX I

METHODS FOR MODAL PARAMETER EXTRACTION

I.1 Peak searching method

Perhaps the simplest method to extract modal parameters from experimental FRFs is the "peak searching" or "peak-picking" method. This method is suitable for structures whose FRF exhibits well separated modes which are not so lightly-damped that accurate measurements at resonance are difficult to obtain, and not so heavily damped that the response at resonance is strongly influenced by more than one mode. Although this appears to limit the applicability of this method, nevertheless, in most cases, FRFs do exhibit not so lightly and not so heavily damped behaviours. For these typical cases, this method can be used as an initial estimator because it is so simple to apply. The procedure to apply the method is as follows:

(1) First, individual resonance peak is detected on the FRF plot, and the frequency of maximum response is taken as the natural frequency of that mode (ω_r);

(2) Second, the maximum value of the FRF is noted ($|H|$) and the frequency bandwidth of the function for a response level of $|H|/\sqrt{2}$ is determined ($\Delta\omega$). The two points thus identified as ω_a and ω_b are the "half-power points";

(3) The damping ratio of the mode in question can now be estimated from the following formula:

$$\zeta_r = \Delta\omega/\omega_r \qquad \text{(A1.1)}$$

where $\Delta\omega = \omega_b - \omega_a$

(4) Finally, the modal constant of the mode being analyzed can be estimated from the following equation:

$$A_r = |H|_{max}(\omega_b^2 - \omega_a^2) \qquad (A1.2)$$

where $|H|_{max}$ is the maximum value of the FRF at the peak point.

I.2 Polynomial method

This method fits a polynomial function, in a rational fraction form, to FRF data in a frequency band around the resonant peak. The fitting is done in a least-squared error sense; sometimes this method is also called the Rational Fraction Least Squares (RFLS) method. When this method is used for a single degree of freedom, the modal frequency, the percentage of critical damping ratio, and the complex residue (magnitude and phase) for the mode can be identified by solving the polynomial as it represents an equation of motion for the system.

This method can also be used for multiple-degrees-of-freedom system (MDOF). After specifying the number of modes in the fit frequency range, the system is solved using the polynomial as it represents the equations of motion of a MDOF system.

The polynomial method fits extra residual polynomial terms to the data to compensate for the effects of modes which are outside the curve-fitting frequency band. These residual terms are used to synthesize the fit function. Therefore the contribution due to the out-of-band modes can be observed by comparing the synthesized and measured FRF data.

1.3 Circle fitting method

For a SDOF system, the frequency response function can be written as:

$$H(\omega) = \frac{1}{(k-\omega^2 m)+i(\omega c)} \tag{A1.3}$$

where m is the mass, k is the stiffness and c is the damping.

Using the relationship between the velocity and displacement

$$U_v = \dot{U} = i\omega H(\omega) e^{i\omega t} \tag{A1.4}$$

the following velocity form of the FRF (designated as $U_v(\omega)$) can be written as:

$$U_v(\omega) = i\omega H(\omega) = \frac{i\omega}{(k-\omega^2 m) + i(\omega c)} = \frac{\omega^2 c + i\omega(k-\omega^2 m)}{(k-\omega^2 m)^2 + (\omega c)^2} \tag{A1.5}$$

The real and imaginary parts can now easily be separated as:

$$Re(U_v(\omega)) = \frac{\omega^2 c}{(k-\omega^2 m)^2 + (\omega c)^2} \tag{A1.6}$$

$$Im(U_v(\omega)) = \frac{\omega(k-\omega^2 m)}{(k-\omega^2 m)^2 + (\omega c)^2} \tag{A1.7}$$

Letting $Z_1 = Re(U_v) - 1/2c$ and $Z_2 = Im(U_v)$, the following equation can be obtained:

$$Z_1^2 + Z_2^2 = \frac{[(k-\omega^2 m)^2 + (\omega c)^2]^2}{4c^2[(k-\omega^2 m)^2 + (\omega c)^2]^2} = \left(\frac{1}{2c}\right)^2 \qquad \text{(A1.8)}$$

which is in fact the equation of a circle with radius of 1/2c and centred at (1/2c, 0).

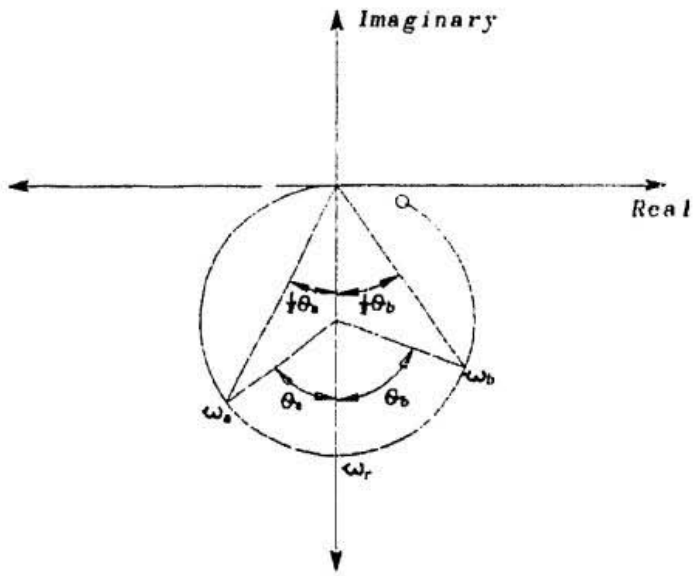

Figure AI.1 Modal circle for receptance

Figure AI.1 shows the properties of the modal circle (also called Nyquist plot) for a displacement FRF (receptance).

The natural frequency ω_r is the frequency value of the point along the circle where sweep rate is maximum. The method of obtaining the natural frequency ω_r is explained later.

The damping ratio can be determined by using any two points on the either side of ω_r from the following equation:

$$\zeta_r = \frac{(\omega_a^2 - \omega_b^2)}{\left\{2\omega_r\left[\omega_a \tan\left[\frac{\theta_a}{2}\right] + \omega_b \tan\left[\frac{\theta_b}{2}\right]\right]\right\}} \qquad \text{(A1.9)}$$

The modal constant (or residue) can be derived from the modal circle diameter using the following equation:

$$A_{ij}^r = D_r(2\omega_r^2\zeta_r) \qquad \text{(A1.10)}$$

where D is the diameter of the modal circle for rth frequency (see Ewins, 1996 for details).

For the MDOF system, the Nyquist plots of FRF data form a section of near-circular arc corresponding to the regions near the natural frequencies. This method, based on the fact that in the vicinity of resonance the behaviour of most systems is dominated by a single mode, can be expressed as follows:

$$H_{ij}(\omega) = \frac{A_{ij}^r}{\omega_r^2 - \omega^2 + i\eta_r\omega_r^2} + \sum_{\substack{k=1 \\ k\neq r}}^{N} \frac{A_{ij}^k}{\omega_k^2 - \omega^2 + i\eta_k\omega_k^2} \qquad \text{(A1.11)}$$

where $\eta_r = \zeta_r\sqrt{1-\zeta_r^2}$ is the damping loss factor; same holds good for η_k.

Since the SDOF assumption is valid for a small range of frequencies in the vicinity of

a natural frequency ω_r the second term on the right hand side of the above equation is approximately independent of frequency ω; hence the above equation can be rewritten as:

$$H_{ij}(\omega) = \frac{A_{ij}^{r}}{\omega_r^2 - \omega^2 + i\eta_r\omega_r^2} + B_{ij}^{r} \qquad (A1.12)$$

The procedure of circle-fit technique can be described as follows:

(1) select points to be used;

(2) fit circle, and calculate quality of fit;

(3) locate natural frequency, obtain damping ratio estimate;

(4) calculate multiple damping estimates, and the scatter;

(5) determine modal constant.

Step (1) can be made by selecting points on either side of any identified maximum response of an FRF. The number of points should encompass some 270° of the circle. Not less than 6 points should be used.

Step (2) can be performed by one of numerous curve-fitting routines and consists simply of finding a circle which gives a least-squares deviation for the points included.

Step (3) can be implemented by constructing radial lines from the circle centre to a succession of points around the resonance and by noting the angles they subtend with each other.

Then, the rate of sweep through the region can be estimated and the frequency at which it reaches a maximum can be obtained. This particular frequency is the natural frequency in question. At the same time, an estimation of damping ratio can be derived using the equation given above.

Next, for step (4), a set of damping estimates are computed using every possible combination from selected points of one point below natural frequency and the other above it and Eqn. (A1.9). If the deviation is less than 4-5%, then the mean value of the damping is the estimated value for the system. If the deviation is 20 or 30%, then the estimation is unsatisfactory. More study should be carried around this point for damping estimation.

Step (5), is to determine the modal constant from the diameter of the circle, and from its orientation relative to the real and imaginary axes.

Finally, it is desirable to construct a theoretically-regenerated FRF plot against the originally measured data. In the vicinity of the resonant region, they should appear very close to one another.

APPENDIX II

WELDING PROCEDURE

SPECIFICATIONS

1. Scope

This specification covers welding and related operations for the fabrication of T-joint by Manual Shielded Metal arc Process in G40.21 Grade 350 WT materials, and is generally in accordance with CSA Standard W59-1982 "Welded Steel Construction" (Metal Arc Welding). Typical welded joint geometry is shown in Figure AII.1.

2. Welding

Welding will be performed by Manual Shielded Metal Arc Process.

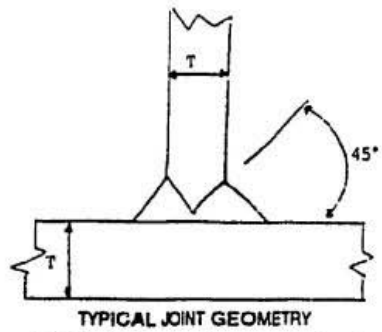

Figure AII.1 Typical welded joint geometry

3. Preparation

Edges and surface of parts to be welded shall be prepared by flame-cutting. They shall be smooth, uniform and free of fins, teras, cracks and other defects which would adversely affect the quality or strength of the weld. Surfaces to be welded shall also be free, within two inches of any weld location, from loose or thick scale, slag, rust, paint, grease, moisture and other foreign material that will prevent proper welding or produce objectionable fumes.

4. Preheat

Prior to tacking or welding, the base metal shall be preheated and the heat maintained during welding at the minimum temperature of 15 °C. Preheating will be accomplished by means of flame torches. Preheating shall consist of heating a band of the base metal equal to the thickness of the base metal, but not less than 3 inches on either side of the joint to the desired temperature, and maintaining this temperature during welding.

5. Distortion Control

In assembling and joining, the procedure and sequence shall be such as will minimize distortion and shrinkage. In so far as practicable, all welds shall be deposited in a sequence that will balance the applied heat of welding while the welding progresses.

6. Appearance of Welding Layers

The welding current and manner of depositing the weld metal shall be such that undercutting on the side walls of the welding groove or the adjoining base material shall be limited to .25 mm for areas subjected to fatigue testing.

7. Cleaning

Cleaning of previously deposited layers shall be done by wire brushing or by mechanical means, if necessary, before the next layer is deposited.

8. Defects

Surface defects appearing on any weld bead shall be removed by grinding and rewelded, if necessary, before the next layer is deposited.

9. Treatment of Second Side of Welding Groove

The root of the joint shall be arc-gouged to produce a groove contour substantially conforming to the prequalified single U-joint, and its depth shall be adequate to ensure complete penetration into the previously deposited weld metal.

10. Finished Joint Profile

The weld profile shall conform to a 45° reinforcing fillet as shown in Figure AII.2, and the capping runs shall be carried out by first depositing a buttering run, to give a good weld toe angle and then filling the bulk of the capping runs. In all cases, the weld toe angle shall conform

to the "dime" test as indicated in the figure. That is, a disc of radius t/2 shall be placed against the butting weld run and the longitudinal plate, and a 1 mm diameter wire shall not pass between the disc and the buttering run in the weld toe region. In all cases, the maximum amount of undercut at the weld toe shall not exceed 0.25 mm.

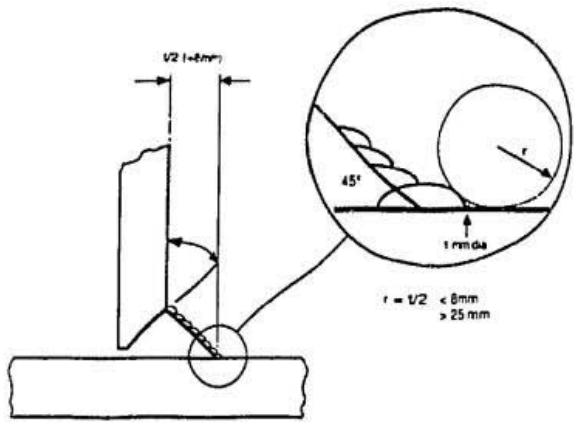

Dime Test

Figure AII.2 Dime test for the T-joint welding

APPENDIX III

NATURAL FREQUENCIES AND DAMPING RATIOS OBTAINED FROM THE EXPERIMENTS ON SEVEN PLATED T-JOINTS

Fatigue stage	1st	2nd	3rd	5th	6th	7th
Specimen #1						
			Natural frequencies (Hz)			
2	84.61	155.96	232.44	451.33	1110.53	1246.04
3	83.43	156.16	232.70	454.41	1111.85	1250.03
4	83.53	156.08	232.28	453.28	1111.57	1247.08
5	83.67	155.92	226.95	452.64	1111.54	1242.08
6	83.36	155.57	223.13	451.38	1110.66	1241.66
7	82.72	154.88	223.80	449.34	1109.75	1240.45
8	83.33	154.34	220.61	447.09	1108.36	1235.00
9	82.51	150.11	196.52	437.54	1103.67	1217.17
10	66.35	82.38	161.94	419.77	1093.13	1181.15
			Damping ratios (%)			
2	1.00	0.50551	0.84323	0.24635	0.07990	0.26867
3	1.03	0.39151	0.86329	0.20199	0.09701	0.20833
4	1.12	0.40551	0.90765	0.24679	0.09031	0.52924
5	1.74	0.47993	0.90723	0.27598	0.09081	0.19118
6	1.67	0.44385	1.17	0.27349	0.09187	0.21376
7	1.50	0.41742	1.36	0.27639	0.09102	0.42507
8	1.81	0.44159	1.33	0.29711	0.11086	0.47164
9	1.07	0.56126	0.93800	0.51490	0.17082	0.63872
10	0.53452	1.59	1.05	0.31956	0.15120	0.51986
Specimen #2						
			Natural frequencies (Hz)			
1	76.84	154.58	232.71	455.94	1118.90	1256.26
2	76.69	154.30	232.44	454.88	1113.29	1252.78
3	76.64	154.17	231.66	454.69	1113.38	1252.59
4	76.69	154.16	231.70	454.82	1113.39	1252.41
5	76.60	154.03	231.70	454.52	1113.28	1251.99
6	76.61	154.10	231.63	454.74	1113.34	1251.50
7	76.70	154.06	231.56	454.82	1113.46	1251.68
8	76.42	154.01	231.46	454.87	1113.51	1251.62
9	76.66	153.96	231.47	454.66	1113.51	1251.15
10	76.65	154.11	231.64	454.68	1113.13	1250.94
11	76.58	154.17	231.30	454.48	1113.03	1249.21
12	76.67	153.92	231.08	454.73	1113.17	1249.37
13	76.70	153.97	230.88	454.58	1113.06	1249.47

Fatigue stage	1st	2nd	3rd	5th	6th	7th
14	76.46	153.85	230.78	454.59	1113.04	1249.08
15	76.53	153.81	230.87	454.18	1112.97	1248.83
16	76.51	153.79	230.68	454.12	1113.04	1249.40
17	76.48	153.67	230.49	454.13	1112.98	1249.16
18	76.59	153.60	230.29	453.91	1112.95	1248.93
19	76.50	153.63	230.50	453.89	1112.67	1248.39
20	76.64	153.53	230.16	453.72	1112.54	1247.83
21	76.43	153.49	230.36	453.71	1112.36	1247.14
22	76.42	153.38	229.82	453.58	1112.51	1247.38
23	76.45	153.26	229.42	453.40	1112.14	1246.74
24	76.48	153.18	229.82	453.56	1112.29	1247.32
25	76.43	153.07	229.66	453.31	1111.85	1246.52
26	76.35	152.58	229.10	453.06	1111.63	1245.65
27	76.32	152.36	228.83	453.00	1111.22	1245.22
28	76.29	152.33	228.50	452.00	1110.71	1244.46
29	76.15	151.98	227.08	451.67	1110.36	1244.02
30	75.98	151.87	227.45	451.90	1110.02	1243.79
31	76.03	151.74	226.87	451.39	1109.69	1243.46
32	75.91	151.44	226.95	451.17	1109.53	1243.13
33	75.89	151.33	226.48	451.02	1109.41	1243.02
34	75.74	151.42	226.36	450.83	1108.98	1242.46
35	75.70	151.50	226.31	451.17	1108.95	1242.40
36	75.60	151.31	225.72	450.42	1108.78	1242.25
37	75.71	150.98	225.93	450.87	1109.37	1242.77
38	75.56	151.33	225.07	449.70	1108.39	1241.60
39	75.29	151.17	224.51	449.68	1108.10	1241.10
40	75.17	151.08	224.04	449.20	1107.86	1237.14
41	74.77	150.94	219.60	447.44	1107.02	1233.10
42	72.98	144.58	198.81	443.58	1104.16	1223.36

Damping ratios (%)

1	0.23232	0.54618	1.14	0.19997	0.16231	0.38111
2	0.19498	0.48736	1.30	0.22754	0.05917	0.40107
3	0.26924	0.40120	1.52	0.21774	0.05622	0.40273
4	0.30645	0.44444	1.38	0.22346	0.05876	0.39451
5	0.32926	0.49337	1.34	0.20890	0.05410	0.40155
6	0.29355	0.53190	1.22	0.22729	0.05457	0.40985
7	0.29166	0.54650	1.23	0.23586	0.05819	0.41519
8	0.33714	0.49245	1.26	0.23946	0.05833	0.38538
9	0.29415	0.48790	1.28	0.21946	0.05317	0.41590
10	0.34084	0.53967	1.28	0.23937	0.05487	0.43590

Fatigue stage	1st	2nd	3rd	5th	6th	7th
11	0.27407	0.73023	1.38	0.21474	0.05453	0.41359
12	0.33272	0.53783	1.36	0.23384	0.05530	0.40008
13	0.27787	0.62714	1.28	0.22946	0.05653	0.39482
14	0.32490	0.48409	1.28	0.22809	0.05365	0.37637
15	0.29932	0.59976	1.20	0.22246	0.05480	0.39001
16	0.33283	0.60334	1.38	0.22090	0.05764	0.39510
17	0.31403	0.55446	1.28	0.22649	0.05678	0.39355
18	0.44564	0.55080	1.18	0.21804	0.05518	0.40445
19	0.25467	0.47976	1.34	0.22634	0.05777	0.41103
20	0.32400	0.46401	1.19	0.22844	0.05589	0.38630
21	0.42043	0.55245	1.23	0.22321	0.05550	0.40288
22	0.28582	0.44114	1.23	0.21526	0.05609	0.43251
23	0.35676	0.57861	1.06	0.21300	0.05331	0.40506
24	0.34919	0.54765	1.15	0.23226	0.05873	0.40174
25	0.35612	0.60725	1.20	0.23323	0.05581	0.38463
26	0.35665	0.65052	1.31	0.22093	0.05428	0.36120
27	0.24657	0.51117	1.25	0.23880	0.05385	0.39242
28	0.21505	0.49643	1.22	0.21200	0.05736	0.29303
29	0.19895	0.51264	1.23	0.21747	0.05582	0.29658
30	0.22279	0.45655	1.10	0.22636	0.05638	0.24590
31	0.35586	0.42277	1.01	0.21362	0.05984	0.24307
32	0.39628	0.53806	1.00	0.21876	0.05702	0.22503
33	0.21337	0.45713	0.88920	0.22399	0.05925	0.23260
34	0.44981	0.59092	0.98997	0.22507	0.05906	0.21165
35	0.22143	0.48078	1.04	0.20760	0.05827	0.21839
36	0.44756	0.53497	0.94605	0.19328	0.06033	0.22522
37	0.20318	0.30856	1.09	0.23294	0.06086	0.24659
38	0.41026	0.54743	1.02	0.20380	0.05907	0.17524
39	0.51691	0.59956	0.95638	0.21747	0.06308	0.18782
40	0.30746	0.43979	0.73227	0.20942	0.06036	0.25750
41	0.37697	0.39797	1.63	0.19448	0.05858	0.30911
42	0.11197	0.46995	1.20	0.20386	0.14118	0.32197

Specimen #3

Natural frequencies (Hz)

0	76.13	153.73	230.96	454.73	1110.39	1250.23
1	75.73	153.78	230.44	454.21	1109.63	1246.36
2	75.73	153.73	230.19	454.03	1109.54	1244.93
3	75.64	153.69	230.69	454.27	1109.52	1245.19

Fatigue stage	1st	2nd	3rd	5th	6th	7th
4	74.82	153.77	230.30	453.87	1109.56	1244.56
5	75.78	153.76	230.72	454.05	1109.51	1244.62
6	75.85	153.80	230.36	453.79	1109.44	1244.21
7	75.76	153.71	230.03	453.92	1109.72	1245.22
8	76.02	153.77	230.53	453.71	1109.60	1244.72
9	75.99	153.81	230.47	453.66	1109.50	1244.51
10	75.96	153.57	230.08	453.86	1109.44	1244.28
11	75.54	153.58	230.12	453.69	1109.46	1244.05
12	75.72	153.55	229.67	453.65	1109.42	1243.94
13	75.98	153.65	229.82	453.60	1109.48	1244.32
14	75.48	153.31	230.00	453.50	1109.35	1243.85
15	75.87	153.17	229.88	453.24	1109.05	1243.90
16	75.63	153.25	228.92	453.18	1108.58	1243.42
17	75.92	153.05	228.55	452.77	1108.21	1242.98
18	75.82	152.85	227.77	452.25	1107.41	1241.96
19	75.59	152.63	227.95	452.12	1107.46	1242.40
20	75.44	152.27	226.75	451.23	1106.44	1238.15
21	75.33	151.89	226.16	450.63	1106.09	1237.28
22	75.18	151.63	226.15	450.11	1106.06	1237.50
23	75.05	151.74	225.88	449.99	1106.29	1238.14
24	74.97	151.20	225.40	449.59	1105.27	1236.49
25	75.01	151.26	225.19	449.01	1104.85	1235.07
26	74.45	146.70	220.80	447.91	1104.16	1233.12
27	72.93	145.08	201.58	443.10	1102.43	1222.73

Damping ratio (%)

0	0.48892	0.52444	1.20	0.17415	0.06833	0.46729
1	0.33395	0.54319	1.22	0.16514	0.06365	0.34737
2	0.44343	0.54914	1.46	0.17101	0.06215	0.27961
3	0.50369	0.46118	1.28	0.17914	0.06037	0.29924
4	0.32691	0.57653	1.23	0.16431	0.06188	0.26169
5	0.56601	0.53204	1.28	0.17352	0.06169	0.26920
6	0.60501	0.53064	1.40	0.15950	0.05904	0.24591
7	0.53688	0.50538	1.45	0.15741	0.06254	0.31512
8	0.45520	0.50888	1.38	0.15470	0.05893	0.27929
9	0.49351	0.51351	1.44	0.15766	0.06137	0.27267
10	0.41583	0.50994	1.19	0.16561	0.05961	0.29246
11	0.47165	0.47757	1.42	0.17123	0.05917	0.26084
12	0.63882	0.49728	1.50	0.16089	0.05773	0.25205
13	0.39483	0.62238	1.41	0.15926	0.05982	0.27141
14	0.43537	0.53225	1.36	0.17869	0.05671	0.27067

Fatigue stage	1st	2nd	3rd	5th	6th	7th
15	0 14630	0.39941	1.43	0.16494	0.05870	0.26469
16	0.27477	0.59167	1.50	0.16788	0.06582	0.24231
17	0.29948	0.58020	1.23	0.16310	0.06819	0.23111
18	0.19707	0.56344	1.21	0.15070	0.06182	0.20290
19	0.24944	0.61833	1.14	0.15793	0.05283	0.21780
20	0.18886	0.59184	0.90395	0.16198	0.04980	0.16856
21	0.17369	0.56202	0.73582	0.17369	0.03783	0.20195
22	0.31887	0.53301	0.62839	0.17600	0.10523	0.22336
23	0.44227	0.60032	0.92975	0.17929	0.10927	0.24005
24	0.38511	0.35151	0.62018	0.19318	0.11164	0.28639
25	0.73756	0.52768	0.78703	0.18214	0.11628	0.28369
26	0.79519	0.45636	1.70	0.17801	0.07763	0.31559
27	0.41289	0.47097	1.05	0.16460	0.05052	0.28767

Specimen #4

Natural frequencies (Hz)

3	75.839	153.10	235.189	457.889	1109.22	1242.06
4	75.947		234.618	456.12	1109.70	1240.95
5	75.929		234.708	456.18	1109.93	1240.72
6	75.813		234.489	456.22	1109.28	1240.54
7	75.727		233.893	456.16	1108.93	1239.87
8	74.761		223.031	456.08	1101.13	1235.84
9	73.757		208.488	454.60	1095.40	1224.95
10	71.988		197.677	453.91	1092.49	1212.28
11	65.000		122.681	409.88	1074.06	1151.26

Damping ratios (%)

3	0.08757	1.460	0.83350	0.18594	0.28793	0.22891
4	0.09268		0.76063	0.23221	0.30140	0.20352
5	0.26647		0.75542	0.24083	0.31599	0.19724
6	0.06130		0.75179	0.24140	0.35748	0.20825
7	0.07340		0.75212	0.24432	0.36581	0.20873
8	0.13035		1.169	0.30953	0.25666	0.30015
9	0.03863		0.82612	0.47376	0.17273	0.47878
10	0.19071		1.060	0.56354	0.28903	0.26271
11			0.96709	0.26399	0.28804	0.11747

Fatigue stage	1st	2nd	3rd	5th	6th	7th
Specimen #5						
			Natural frequencies (Hz)			
0	75.998	165.171	234.147	467.132	1103.97	1245.60
1	76.067	166.561	232.275	466.857	1103.18	1239.14
2	76.175	166.763	232.340	467.028	1103.57	1238.73
3	76.110	166.963	232.449	466.967	1103.95	1239.18
4	76.133	167.168	232.643	467.153	1103.90	1239.26
5	75.662	167.290	232.372	466.900	1104.12	1239.23
6	75.899	167.117	231.799	466.641	1103.63	1238.43
7	75.713	166.196	229.433	466.326	1102.91	1237.27
8	75.572	165.202	224.009	466.495	1102.07	1234.89
9	72.701	165.216	201.290	464.935	1095.53	1222.58
10	66.124	154.108	176.068	462.359	1088.21	1205.61
			Damping ratios (%)			
0	0.03000	1.694	0.78128	0.69614	0.18370	0.31514
1	0.03110	2.292	0.73600	0.67864	0.21097	0.25930
2	0.04894	2.344	0.72734	0.69750	0.21906	0.22827
3	0.01849	2.630	0.75916	0.70275	0.24289	0.25121
4	0.05136	2.776	0.81606	0.73732	0.22616	0.24185
5	0.01405	2.444	0.73293	0.72168	0.22627	0.25169
6	0.12540	2.545	0.75542	0.73160	0.22257	0.23832
7	0.08268	2.621	0.84315	0.67008	0.22147	0.24737
8	0.11833	3.013	0.93090	0.73589	0.17819	0.27078
9	0.21152	1.680	2.009	0.65319	0.24327	0.27650
10	0.32864	2.228	1.134	0.49615	0.12790	0.25607
Specimen # 6						
			Natural frequencies (Hz)			
0	75.544		227.259	456.44	1100.59	1228.72
1	75.638		226.945	456.61	1100.95	1227.80
2	75.520		227.196	456.84	1101.40	1227.93
3	75.321		227.532	457.03	1101.65	1228.21
4	75.555		227.588	457.18	1102.07	1228.37
5	75.606		227.551	457.18	1101.93	1227.74
6	75.326		227.810	457.12	1102.25	1228.02
7	75.608		228.173	457.22	1102.23	1228.51
8	75.614		228.058	457.16	1102.76	1228.84

Fatigue stage	1st	2nd	3rd	5th	6th	7th
9	75.500		225.372	457.10	1101.64	1226.80
10	75.230		223.728	457.02	1101.25	1225.94
11	74.892		219.212	457.17	1100.36	1224.13
12	72.210		197.905	457.21	1091.36	1210.02

Damping ratios (%)

0	0.03301		0.64698	0.18929	0.14419	0.19700
1	0.01729		0.61928	0.17041	0.12724	0.19359
2	0.02907		0.62427	0.14665	0.11108	0.19114
3	0.00126		0.62734	0.13950	0.10340	0.21074
4	0.04301		0.67304	0.18168	0.11225	0.20711
5	0.05617		0.60169	0.16000	0.12161	0.17090
6	0.00939		0.61162	0.14905	0.12640	0.17655
7	0.05787		0.71236	0.16888	0.10471	0.20934
8	0.02650		0.68965	0.13625	0.12195	0.20150
9	0.04690		0.62572	0.15590	0.11618	0.18906
10	0.13381		0.62309	0.13093	0.10852	0.19654
11	0.05995		0.84400	0.18817	0.09380	0.25451
12	0.14129		0.98957	0.23711	0.15867	0.21739

Specimen #7

Natural frequencies (Hz)

0	75.771	139.524	231.997	467.183	1104.67	1238.18
1	76.033	174.625	230.390	468.563	1105.67	1233.93
2	75.808	174.897	230.850	468.360	1105.68	1233.24
3	75.946	174.741	230.600	468.794	1105.62	1232.70
4	75.774	174.813	230.453	469.431	1106.15	1232.84
5	75.623	174.143	229.366	469.100	1105.66	1232.95
6	75.616	173.925	227.201	468.344	1105.36	1231.81
7	75.295	174.035	226.098	469.201	1105.65	1231.99
8	75.187	173.976	222.097	468.753	1105.30	1229.71
9	72.901	173.374	201.996	467.274	1101.46	1218.18

damping ratios (%)

0	0.07031	2.406	0.96925	0.74420	0.19551	0.36005
1	0.06895	2.480	0.88346	0.87557	0.22766	0.30438
2	0.07373	2.496	0.90224	0.87093	0.21562	0.28445

Fatigue stage	1st	2nd	3rd	5th	6th	7th
3	0.20416	2.298	0.91270	0.89328	0.21005	0.26678
4	0.10082	2.405	0.90523	0.91164	0.19170	0.27352
5	0.09560	2.400	0.89235	0.88417	0.19563	0.29630
6	0.07462	2.362	1.006	0.85891	0.21255	0.29455
7	0.18203	2.359	1.128	0.88619	0.21370	0.34317
8	0.04082	2.391	1.101	0.88398	0.21840	0.31396
9	0.17404	2.506	0.98488	0.82291	0.16803	0.31161